# LUND UNIVERSITY

**Numerical modelling of biomass thermochemical conversion and potassium release**

Mousavi, Seyed Morteza

2022

# Numerical modelling of biomass thermochemical conversion and potassium release

SEYED MORTEZA MOUSAVI

DEPARTMENT OF ENERGY SCIENCES | FACULTY OF ENGINEERING | LUND UNIVERSITY

# Numerical modelling of biomass thermochemical conversion and potassium release

by Seyed Morteza Mousavi

LUND
UNIVERSITY

Thesis for the degree of Doctor of Philosophy
Thesis advisors: Prof. Xue-Song Bai, Dr. Hesamedin Fatehi
Faculty opponent: Prof. Jeroen Van Oijen

| Organization | Document name |
|---|---|
| **LUND UNIVERSITY** | **DOCTORAL DISSERTATION** |
| Department of Energy Sciences<br>Box 118<br>SE–221 00 LUND<br>Sweden | Date of disputation<br>2022-12-16 |
| | Sponsoring organization<br>Swedish Energy Agency (STEM) through KC-CECOST, Knut & Alice Wallenberg foundation (KAW COCALD project) |
| Author(s)<br>Seyed Morteza Mousavi | |

Title and subtitle

Numerical modelling of biomass thermochemical conversion and potassium release

Abstract

The use of biomass as a renewable source of energy has been increasing over the past few decades, and biomass is regarded as a promising replacement for fossil fuels. Thermochemical conversion of biomass is a common approach for biomass utilization with a relatively short conversion time. Despite the many advantages that biomass offers over fossil fuels, the thermochemical conversion of biomass has some drawbacks including harmful emissions such as NO and negative impacts of alkali metals such as potassium, which need to be further studied. Numerical modelling is a powerful tool that compliments the experimental measurements for studies on biomass conversion and its challenges.

In this thesis, numerical models are developed with a focus on different scales of biomass conversion, ranging from single particles to reactor-scale simulations. A detailed mesh-based particle model is developed to study the intra-particle phenomena, as well as the reactions surrounding the particle. The model is used to study the effects of particle shrinkage, anisotropic heat transfer, and the stiff problem of particle-surrounding gas coupling. Moreover, a new anisotropic shrinkage model is proposed that correlates the axial and radial shrinkage of particles to the decomposition of main wood components, i.e., cellulose, hemicellulose, and lignin. Finally, the particle model is used to study the stages of hydrogen release during pyrolysis and the effects of wood inhomogeneities on particle conversion.

Potassium release from biomass can cause numerous problems in the reactors, namely, corrosion, slagging, fouling, and aerosol formation. A new detailed potassium release model is developed in the current study, which for the first time, takes into account the effects of variables such as fuel type and ash composition, conversion temperature, and surrounding atmosphere. The model is validated against different experimental measurements from the literature in terms of the prediction of different types of potassium in residual solid, the total potassium, chloride, and sulfur in solid, and also the gas-phase potassium-containing species downstream of reacting particles. Later, the developed potassium model is used in a CFD simulation of an entrained flow gasifier to study the gasification process and the potassium release in the reactor.

Numerical studies are also carried out to investigate the performance and NO emissions from fixed-bed biomass reactors. A novel method is proposed to handle the complicated tar species and their decomposition in the freeboard of a lab-scale fixed bed reactor. The model is used to study NO emissions from the same reactor and the performance of selective non-catalytic reduction (SNCR) for NO reduction. In a later study, the bed is also included in the simulations with a fast-solving 2D bed model. The model is based on the detailed simulation of thermally-thick particle conversion at different conditions. The simulation results are tabulated and then used to extract the source terms for particles in the fuel bed at different times and locations.

Key words

Numerical modelling, particle model, bed model, CFD simulation, biomass, pyrolysis, combustion, gasification, potassium release, alkali

Classification system and/or index terms (if any)

| Supplementary bibliographical information | | Language<br>English |
|---|---|---|
| ISSN and key title<br>0282-1990 | | ISBN<br>978-91-8039-441-3 (print)<br>978-91-8039-442-0 (pdf) |
| Recipient's notes | Number of pages<br>255 | Price |
| | Security classification | |

Signature _____     Date _____2022-09-15_____

DOKUMENTDATABLAD enl SIS 61 41 21

# Numerical modelling of biomass thermochemical conversion and potassium release

by Seyed Morteza Mousavi

A doctoral thesis at a university in Sweden takes either the form of a single, cohesive research study (monograph) or a summary of research papers (compilation thesis), which the doctoral student has written alone or together with one or several other author(s).

In the latter case the thesis consists of two parts. An introductory text puts the research work into context and summarizes the main points of the papers. Then, the research publications themselves are reproduced, together with a description of the individual contributions of the authors. The research papers may either have been already published or are manuscripts at various stages (in press, submitted, or in draft).

Media-Tryck is a Nordic Swan Ecolabel certified provider of printed material. Read more about our environmental work at www.mediatryck.lu.se

NORDIC SWAN ECOLABEL

Printed matter
3041 0903

MADE IN SWEDEN

*To Salma and Noura*

# Contents

**Numerical modelling of biomass thermochemical conversion and potassium release**  ⋯ **1**

# List of publications

This thesis is based on the following publications, referred to by their Roman numerals:

I  **Multi-region modeling of conversion of a thick biomass particle and the surrounding gas phase reactions**
**Seyed Morteza Mousavi**, Hesameddin Fatehi, Xue-Song Bai
*Combustion and Flame* 237 (2022): 111725,
https://doi.org/10.1016/j.combustflame.2021.111725

II  **Detailed modeling of hydrogen release and particle shrinkage during pyrolysis of inhomogeneous wood**
**Seyed Morteza Mousavi**, Frederik Ossler, Charles E.A. Finney, Xue-Song Bai, Hesameddin Fatehi
*Proceedings of the Combustion Institute* 39 (2022): , 1540-7489,
https://doi.org/10.1016/j.proci.2022.07.108

III  **A multi-step predictive model for the release and transformation of K-Cl-S-containing species from biomass**
**Seyed Morteza Mousavi**, Xue-Song Bai, Hesameddin Fatehi
*Accepted for publication in Combustion and Flame* (2022)

IV  **Numerical study and experimental verification of biomass gasification and potassium release in a 140 kW entrained-flow gasifier**
**Seyed Morteza Mousavi**, Emil Thorin, Florian M. Schmidt, Alexey Sepman, Xue-Song Bai, Hesameddin Fatehi
*Energy and Fuels* (2022): Under revision.

V  **Numerical study of the combustion and application of SNCR for NOx reduction in a lab-scale biomass boiler**
**Seyed Morteza Mousavi**, Hesameddin Fatehi, Xue-Song Bai
*Fuel* 293 (2020): 120154,
https://doi.org/10.1016/j.fuel.2021.120154

VI  **A tabulation-based numerical model for the combustion of thick particles in fixed-bed reactors**
**Seyed Morteza Mousavi**, Hesameddin Fatehi, Xue-Song Bai
*Manuscript to be submitted*

Publications not included in this thesis:

VII     **Numerical simulation of biomass gasification in fluidized bed gasifiers**

Miao Yang, **Seyed Morteza Mousavi**, Hesammedin Fatehi, Xue-Song Bai
*Fuel* (2022): Under revision

# Acknowledgements

First of all, I would like to express my sincere gratitude and appreciation to my supervisors Prof. Xue-Song Bai and Dr. Hesameddin Fatehi, who trusted me with this position in the first place and gave me the chance to study and carry out research in this exciting field. You have always been available for discussion, provided a great vision of the problems, and suggested perfect directives for the research, and I certainly could not ask for more from you. It was a great pleasure and honour to work with and learn from you.

I would also like to thank my co-authors, Frederik Ossler, Charles Finney, Florian Schmidt, Emil Thorin, and Alexey Sepman. Thanks for performing the experiments that were necessary for parts of my research, helping to analyze the results from different perspectives, and also helping a lot with the writing and revision of the papers.

I truly enjoyed my time at Lund University as a PhD student mainly because of the great people I met here. I am highly grateful to the senior staff and colleagues at the Department of Energy Sciences, Robert Szász, Catarina Lindén, Isabelle Frej, Marcus Thern, Lei Wang, Johan Revstedt, Magnus Genrup, and Rixin Yu. I will always remember all the things that I have learnt from you, and all the help and advice that you provided to me at different times. Moreover, I am extremely grateful to my wonderful friends in the department, Ahmad Hadadpour, Michael Bertch, Ali Al Sam, Shijie Xu, Leilei Xu, Thommie Nilsson, Mateusz Pucilowski, Christian Ibron, Senbin Yu, Monika Englund, Miao Yang, Francesco Pignatelli, Mark Treacy, Marcus Hothar, Yuxiang Lim, Alessandro Ercole, Ali Moallemi, and all the other students and postdocs that I met at the department, even for a short period. We spent so much time together, organized and participated in so many activities and I will never forget all the fun that we had together. I was extremely lucky to have incredible friends out of the department as well. I would like to express my deepest appreciation to the families of Hadadpour, Owlad, Mahdavi, Yazdi, Mirhajian, Naseri-Rad, Yousefian, Aminifar, Abtahi, and Bagheri. I have never felt alone, even in the toughest situations such as the Covid outbreak, simply because of your kind presence. I cannot forget all the gatherings, random discussions, sports activities, excursions, and all the fun time we spent together, and I will try to always keep in touch in future.

Words cannot express my gratitude to my family without whom, I could not have undertaken this journey. My special thanks go to the love of my life, Salma, and my lovely daughter, Noura. You have been wonderful, patient, and understanding the whole time, and I am so grateful that I have both of you in my life. Moreover, I would like to express my deepest gratitude to my parents, my brother and sisters, my

brother- and sister-in-law, and my nieces and nephews. Living far away from you was the most difficult challenge for me over the past few years, but you have always been so nice and supportive the whole time that I could feel your love from thousands of kilometres away.

# Popular science summary

The increasing concern over climate change and global warming has led the people all around the world to consider replacing fossil fuels with renewable sources of energy which have a lower impact on the environment. A promising source of renewable energy is biomass which is a large group of organic materials including wood and other plant-based materials and also residual waste. Biomass became much more popular in the past few decades because it offers several advantages over fossil fuels. First, different biomass sources such as wood, forestry residues, crops, agricultural residues, vegetable oils, and straws are available all around the world. Second, biomass is a renewable source of energy that can be replenished over a relatively short time. Third, biomass can be $CO_2$-neutral if produced in a sustainable way. This means that the same amount of $CO_2$ that was captured by the plant during its growth stage will be released into the atmosphere after the utilization. These unique features have led to the rapid growth of biomass applications over recent years. Furthermore, there are several rules and recommendations all around the world, which motivate further biomass usage. For instance, there is a target of at least 32% renewable energy in the European Union's energy consumption by 2030. Among European countries, Sweden has the highest share of renewable energy in gross final energy consumption (around 60% in 2020). The largest source of renewable energy is biomass which accounts for more than 26% of the total energy in Sweden in 2020. This high share of biomass in the energy sector motivates further research on biomass utilization process to improve the efficiency of this technology and reduce the harmful emissions.

Biomass can be converted to energy or other types of fuels through thermochemical or biochemical processes. The thermochemical conversion, which is the main topic of this study, is the act of processing biomass through heat and chemical reactions. For this purpose, solid biomass is placed in a special device, called a reactor, which is operated at a relatively high temperature. Depending on the application of the reactor, some air or other gas mixtures is blown into the reactor which reacts with the biomass. In some reactors, biomass is directly burned with the oxygen available in the gas to produce heat. But in other cases, the solid biomass is heated in an oxygen-free environment and is converted to the other types of liquid or gaseous biofuels, for instance through chemical reactions with water vapour or carbon dioxide. The liquid and gas biofuels are easier to use and have many different applications in the transport sector or electricity production. Hydrogen gas ($H_2$) and carbon monoxide (CO) and their mixtures, called syngas, are among the interesting products of biomass thermochemical conversion.

Despite many advantages and the wide range of applications of biomass, there are some drawbacks such as the emission of nitrogen oxides (NOx – which are harmful

to humans and the environment) and the release of unwanted inorganic elements such as potassium, chlorine, and sulfur (which are abundant in plant-based biomass and are harmful to the device and atmosphere), which have to be studied in more detail. The performance of a biomass reactor can be studied by experimental measurement of important parameters such as temperature or species concentrations at various locations in the reactor. However, measurement techniques are usually expensive, cannot be applied to every type of reactor, and only a limited number of parameters can be measured at the same time. Therefore, numerical (mathematical) models are also developed and used to simulate and study the process of biomass thermochemical conversion. To develop a numerical model, all the physical processes such as fluid flow, heat transfer, and chemical reactions, are represented as a set of mathematical equations which are called governing equations. Solid biomass particles have a porous structure, so the physical processes inside and outside the particle have to be considered in the governing equations. Typically, these governing equations can be solved using computers to predict/simulate the biomass conversion process.

In this thesis, the objective is to develop numerical models for the thermochemical conversion of biomass and use the models to better understand the physics of the process. The main contributions of the thesis are: the development and verification of a detailed single-particle model, and a new shrinkage model based on the structure of the wood; the development of a chemical kinetic model for the release of potassium, chlorine, and sulfur from biomass particles and applying the model to simulate a real biomass reactor; the development of a model for conversion of several large particles at the bottom of a reactor, and study of the NOx emissions and reduction methods in the reactors. These detailed models contribute to the long-term development of simulation tools that can be used to design and optimize the biomass thermochemical conversion process and reactors.

# Abstract

The use of biomass as a renewable source of energy has been increasing over the past few decades, and biomass is regarded as a promising replacement for fossil fuels. Thermochemical conversion of biomass is a common approach for biomass utilization with a relatively short conversion time. Despite the many advantages that biomass offers over fossil fuels, the thermochemical conversion of biomass has some drawbacks including harmful emissions such as NO and negative impacts of alkali metals such as potassium, which need to be further studied. Numerical modelling is a powerful tool that compliments the experimental measurements for studies on biomass conversion and its challenges.

In this thesis, numerical models are developed with a focus on different scales of biomass conversion, ranging from single particles to reactor-scale simulations. A detailed mesh-based particle model is developed to study the intra-particle phenomena, as well as the reactions surrounding the particle. The model is used to study the effects of particle shrinkage, anisotropic heat transfer, and the stiff problem of particle-surrounding gas coupling. Moreover, a new anisotropic shrinkage model is proposed that correlates the axial and radial shrinkage of particles to the decomposition of main wood components, i.e., cellulose, hemicellulose, and lignin. Finally, the particle model is used to study the stages of hydrogen release during pyrolysis and the effects of wood inhomogeneities on particle conversion.

Potassium release from biomass can cause numerous problems in the reactors, namely, corrosion, slagging, fouling, and aerosol formation. A new detailed potassium release model is developed in the current study, which for the first time, takes into account the effects of variables such as fuel type and ash composition, conversion temperature, and surrounding atmosphere. The model is validated against different experimental measurements from the literature in terms of the prediction of different types of potassium in residual solid, the total potassium, chloride, and sulfur in solid, and also the gas-phase potassium-containing species downstream of reacting particles. Later, the developed potassium model is used in a CFD simulation of an entrained flow gasifier to study the gasification process and the potassium release in the reactor.

Numerical studies are also carried out to investigate the performance and NO emissions from fixed-bed biomass reactors. A novel method is proposed to handle the complicated tar species and their decomposition in the freeboard of a lab-scale fixed bed reactor. The model is used to study NO emissions from the same reactor and the performance of selective non-catalytic reduction (SNCR) for NO reduction. In a later study, the bed is also included in the simulations with a fast-solving 2D bed model. The model is based on the detailed simulation of thermally-thick particle conversion

at different conditions. The simulation results are tabulated and then used to extract the source terms for particles in the fuel bed at different times and locations.

# Nomenclature

| | |
|---|---|
| $A_p$ | Surface area, particle surface area [m$^2$] |
| $A_i$ | Pre-exponential constant for i'th reaction [Different units] |
| $C_{diff,i}$ | Diffusion constant for char reactions [s K$^{-0.75}$] |
| $C_i$ | Concentration of i'th species [mol m$^{-3}$] |
| $c_1$ | Mass progress variable (bed model) [−] |
| $c_2$ | Surface temperature progress variable (bed model) [−] |
| $c_p$ | Specific heat capacity [J kg$^{-1}$ K$^{-1}$] |
| $D$ | Diameter [m] |
| $D_{AB}$ | Binary diffusion coefficient [m$^2$ s$^{-1}$] |
| $D_{eff}$ | Effective diffusion coefficient [m$^2$ s$^{-1}$] |
| $d_p$ | Particle diameter [m] |
| $d_{pore}$ | Pore diameter [m] |
| $E_i$ | Activation energy [kJ mol$^{-1}$] |
| $F$ | Force [kg m s$^{-2}$] |
| $f_{D,p}$ | Drag force on the particle [kg m s$^{-2}$] |
| $g$ | Gravitational acceleration vector [m s$^{-2}$] |
| $h$ | Specific enthalpy of fluid [J kg$^{-1}$] |
| $h_{rad}$ | Convection coefficient due to radiation [W m$^{-2}$ K$^{-1}$] |
| $h_{conv}$ | Heat convection coefficient [W m$^{-2}$ K$^{-1}$] |
| $h_{eff}$ | Effective convection coefficient [W m$^{-2}$ K$^{-1}$] |
| $h_m$ | Mass convection coefficient [m s$^{-1}$] |
| $\vec{I}$ | Unity vector [−] |
| $K$ | Permeability [m$^2$] |
| $Ke$ | Kinetic energy per unit mass [J kg$^{-1}$] |
| $L$ | Length [m] |
| $M$ | Molar mass [kg mol$^{-1}$] |
| $m$ | Mass [kg] |
| $p$ | Pressure [Pa] |
| $\dot{Q}$ | Heat generation [W or W m$^{-3}$] |
| $\dot{\Re}$ | Mass source term [kg s$^{-1}$ or kg m$^{-3}$ s$^{-1}$] |
| $R_u$ | Universal gas constant [J mol$^{-1}$ K$^{-1}$] |
| $r$ | Reaction rate [Different units] |
| $r_m$ | Char reactivity per unit mass [s$^{-1}$] |
| $r_A$ | Char reactivity per unit surface area [m$^{-2}$ s$^{-1}$] |
| $r_{m,dif}$ | Diffusion limited char reactivity [s$^{-1}$] |
| $r_{m,kin}$ | Kinetic limited char reactivity [s$^{-1}$] |
| $S_A$ | Particle surface area density [m$^2$ m$^{-3}$] |
| $S_p$ | Source term for momentum in porous bed [kg m$^{-2}$ s$^{-2}$] |
| $T$ | Temperature [K] |
| $T_s$ | Particle surface temperature [K] |
| $T_{eff}$ | Effective temperature (bed model) [K] |
| $t$ | Time [s] |
| $U$ | Velocity [m s$^{-1}$] |
| $V$ | Volume [m$^3$] |
| $X_C$ | Char conversion [−] |
| $Y_i$ | Mass fraction of species $i$ [−] |
| **Greek symbols** | |
| $\alpha$ | Thermal diffusivity [m$^2$ s$^{-1}$] |

| | |
|---|---|
| $\beta$ | Temperature exponent in Arrhenius reaction rate $[-]$ |
| $\vec{\beta}$ | Longitudinal shrinkage vector $[-]$ |
| $\Delta\vec{\beta}_j$ | Empirical shrinkage vector for each wood component $[-]$ |
| $\Delta$ | Change in parameter $[-]$ |
| $\epsilon$ | Emissivity $[-]$ |
| $\varepsilon$ | Porosity $[-]$ |
| $\eta_{NH3}$ | Ammonia utilization efficiency $[-]$ |
| $\theta$ | Volume shrinkage factor $[-]$ |
| $\kappa$ | Conduction coefficient [W m$^{-1}$ K$^{-1}$] |
| $\kappa_{a,e}$ | Absorption/emission coefficient [m$^{-1}$] |
| $\mu$ | Dynamic viscosity [kg m$^{-1}$ s] |
| $\nu$ | Stoichiometric coefficient $[-]$ |
| $\rho$ | Density [kg m$^{-3}$] |
| $\sigma$ | Stefan–Boltzmann constant [W m$^{-2}$ K$^{-4}$] |
| $\tau$ | Total stress tensor [Pa] |
| $\Omega_C$ | Determines CO to CO$_2$ ratio in char combustion $[-]$ |

**Subscripts**

| | |
|---|---|
| *conv* | Related to convection |
| *rad* | Related to radiation |
| *drying* | Related to drying |
| *pyrolysis* | Related to pyrolysis |
| *char* | Related to char conversion |
| *reac* | Related to reactions |
| *dif* | Related to diffusion |
| *kin* | Related to kinetics |
| *M* | Moisture |
| *B* | Biomass |
| *C* | Char |
| *eff* | Effective |
| *ref* | Reference |
| *tot* | Total |
| *b* | Related to bed |
| *p* | Related to particle |
| *s* | Related to solid or particle surface |
| *g* | Related to gas |
| *i, j* | Indices for different species or reactions |
| *si* | Indices for solid species |
| *gi* | Indices for gas species |
| 0 | Initial value |
| $\infty$ | Final value or value in surrounding gas |

**Dimensionless numbers**

| | |
|---|---|
| Bi | Biot number |
| Nu | Nusselt number |
| Pr | Prandtl number |
| Re | Reynolds number |
| Sc | Schmidt number |
| Sh | Sherwood number |

**Abbreviations**

| | |
|---|---|
| WBA | World Bioenergy Association |
| IEA | International Energy Agency |

| | |
|---|---|
| SNCR | Selective Non-Catalytic Reduction |
| SCR | Selective Catalytic Reduction |
| EFG | Entrained Flow Gasifier |
| ODE | Ordinary Differential Equation |
| PDE | Partial Differential Equation |
| CFD | Computational Fluid Dynamics |
| HCE | Hemicellulose |
| CEL | Cellulose |
| LIG | Lignin |
| EXT | Extractives |
| MET | Metaplastic species |
| DOM | Discrete Ordinate Method |
| PSR | Perfectly Stirred Reactor |
| NCT | Neutron Computed Tomography |
| TDLAS | Tunable Diode Laser Absorption Spectroscopy |
| PF-TDLAS | PhotoFragmentation Tunable Diode Laser Absorption Spectroscopy |
| NSR | Nitrogen Stoichiometric Ratio |

# Numerical modelling of biomass thermochemical conversion and potassium release

# Chapter 1

# Introduction

## 1.1 Motivations

Biomass is a renewable source of energy that is widely used as a replacement for fossil fuels to control global warming and climate change. Biomass offers many benefits as it is available worldwide, is $CO_2$ neutral, and has a wide range of applications. Based on the statistics from the World Bioenergy Association (WBA), around 17% of the gross final energy consumption in 2019 was from renewable sources, where biomass accounts for 70% of the renewables [1]. This marks biomass as the main source of renewable energies and the fourth largest source of energy in the world (after oil, natural gas, and coal) with a share of 12% in the total energy consumption [1]. Energy production from renewable sources and biomass in specific is expected to increase even more in the coming years, because of the new environmental laws and directives all around the world. For instance, the renewable energy directive in Europe sets a target of at least 32% renewable energy in the EU's energy consumption by 2030 [2].

The mentioned directives and other regulations greatly changed the share of different energy sources over the past few decades. The gross available energy from different sources from 1990 to 2020 in Europe (data obtained from Eurostat database [3]) is presented in Fig. 1.1. It can be observed that the share of solid fossil fuels has been decreasing while the energy from renewable sources has been increasing over the years. Since 2018, renewables surpassed solid fossil fuels and also nuclear heat and became the third largest source of energy in Europe after oil and natural gas. In Sweden, the ambition for utilization of renewable energy sources are even higher than in the rest of Europe. The gross available energy sources in Sweden [3] are presented

in Fig. 1.2, which shows that since 2010, the largest portion of Energy in Sweden is obtained from renewable sources. Based on the data from the International Energy Agency (IEA) [4], energy from biofuels and waste is the biggest source of renewable energy in Sweden, and in 2020, it was the second largest source of total energy supply with 26.6%, only surpassed by nuclear energy with 26.9% share.
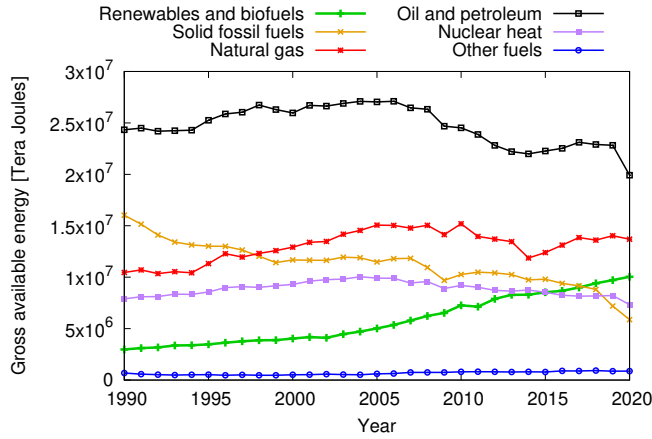


**Figure 1.1:** Gross available energy from different sources in Europe between 1990 to 2020 [3].
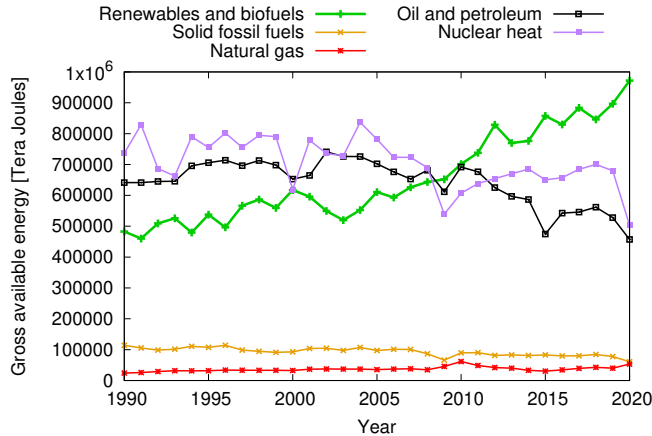


**Figure 1.2:** Gross available energy from different sources in Sweden between 1990 to 2020 [3].

The above discussion highlights the significant role of biomass as an energy source all around the world and especially in Sweden. Based on the trends in energy supply over the past few decades, it is expected that the applications of biomass in the energy sector will expand even more in the coming years, which motivates further research in this field. Biomass conversion for energy production is a complicated

process that should be studied with a focus on different scales. Experimental measurements and numerical modelling are the two main tools for the study of biomass conversion, and the focus is on the latter in the present thesis. The multi-scale conversion of biomass and its challenges, and how they can be improved by numerical modelling are introduced in the next sections of this chapter. Finally, the contribution of the present thesis is explained at the end of this chapter.

## 1.2   Biomass conversion

Biomass is referred to organic and usually plant-based material such as wood, agricultural residues, forestry residues, grasses and straws, energy crops, or in a wider view, municipal and food waste can also be considered as biomass [5, 6]. The main source of biomass is plant-based (also called lignocellulosic) which can be converted to other types of fuel or energy through biochemical or thermochemical conversion. The thermochemical conversion of biomass, which is the main focus of the present work, is the fastest and the most efficient method for biomass utilization [7]. The main types of thermochemical conversion are pyrolysis (devolatilization), gasification, and oxidation (combustion) which are explained in the following.

Pyrolysis is the decomposition of initial solid fuel in a hot and inert atmosphere which leads to the release of volatiles and the formation of char. The main volatile species that are released during pyrolysis (or devolatilization) are water, permanent gas, and tar. Permanent gas (also referred to as gas or light gas) is a mixture of volatile species released during pyrolysis which are in the gas phase at room temperature. $H_2$, CO, $H_2O$, $CO_2$, and $CH_4$ are the main components of gas which are produced during pyrolysis [8]. Tar is also a mixture of volatile species that are released during pyrolysis, but tar (also called bio-oil) species are in condensed form at room temperature. The composition of tar is more complicated than gas and it can contain various molecules with different molecular weights and properties. The residual solid after pyrolysis is called char (also bio-char or charcoal) which is highly rich in carbon and is comparable to coal. The pyrolysis process is endothermic meaning it requires energy to progress. However, the gas, liquid, and solid-phase products of pyrolysis are all combustible, and they can be used in different devices to produce energy. The ratio of gas, tar, and char in the pyrolysis products is dependent on many factors, such as maximum temperature, heating rate, particle size, and fuel type. Especially, temperature has a high impact and generally a higher temperature leads to a higher gas, and lower tar and char production. Torrefaction is a mild type of pyrolysis performed at low temperatures to produce char. In some cases, pyrolysis can be used as an independent technology to produce secondary types of biofuels. However, pyrolysis is also studied because it is an important stage of biomass conversion in any other

technology such as combustion or gasification.

Biomass combustion and gasification are among the most important technologies for biomass utilization. In both combustor and gasifier reactors, the biomass particles are injected into the hot atmosphere of the reactor to undergo drying and pyrolysis first. In a combustor, enough oxygen is available for the complete combustion of volatiles and char, and the combustors are used for direct energy production. However, in a gasifier instead of oxygen, the atmosphere is rich in $CO_2$ or $H_2O$. After pyrolysis, the char reacts with $CO_2$ and $H_2O$ which leads to the production of a gas mixture which is rich in CO and $H_2$. The produced gas which is called synthesis gas or syngas has a high calorific value and it can be used as a clean fuel in other combustion devices. Similar to pyrolysis, char gasification is an endothermic process and is used to produce secondary types of biofuels. The energy required for the gasification process can be obtained by partial combustion of the char or volatiles. Char gasification and oxidation are heterogeneous reactions happening between solid and gas phases, at the surface of the char pores. The heterogeneous char reactions are generally more complicated than the homogeneous gas-phase reactions, as they depend on many factors such as temperature, the diffusion rate of the reactant and product gases, particle size and structure, and concentration of inorganic elements inside biomass which can act as a catalyst for the reaction [5, 9]. Some of the mentioned parameters such as the particle size and the operating temperature are determined by the requirements of the biomass conversion device. Hence, it is important to know the main characteristics of different devices that are used for biomass conversion.

The combustion and gasification of biomass can be carried out in fixed (or moving) bed, entrained flow, and fluidized bed reactors [9]. Large biomass particles which have a long conversion time are usually converted in fixed-bed reactors. Fixed bed reactors are relatively insensitive to particle size and moisture content which makes their design and fuel processing more simple. However, the temperature and heating rate are relatively low in this design, which promotes tar formation, which is not the desired product, especially in gasifiers. Moreover, it is not easy to maintain a stable flame front in a large bed of fuel particles, so fixed bed reactors are mainly used in domestic or small-scale industrial applications [9]. In fluidized bed reactors, the biomass particles should be small enough to be suspended by the fluid flow. In addition to the biomass particles, inert sand particles are also injected into the fluidized bed which helps to keep the bed temperature high and the process of gasification/combustion continuous. Fluidized bed reactors have a better mixing and a higher conversion rate compared to fixed bed reactors, and they have the possibility to be scaled up to medium and large scale [9]. On the other hand, the design of this type of reactor is more complicated and the temperature inside the reactor has to be limited to avoid sand melting and bed agglomeration. The entrained flow reactors are used for

large-scale systems, in which very small fuel particles are injected into the reactor and converted at high temperature and low residence time [10]. In this design, the temperature can be higher than in the fluidized bed reactors, since there is no sand in the system and the liquid ash can be removed easily [11]. The high temperature in this type of reactor improves the carbon conversion efficiency and also leads to the production of a gas that is almost tar-free, which is highly important for gasifiers [9, 12]. The main drawbacks of entrained flow reactors are the cost of size reduction of fuel and the problems such as slagging or corrosion associated with the high alkali content of biomass, which are more significant at higher temperatures.

## 1.3 Challenges of biomass conversion

There are some challenges and complications related to biomass thermochemical conversion and further research is still required to improve the design of conversion devices. The main problems can be categorized as those related to emissions to the environment, ash and alkali-related problems, and conversion efficiency and products. Such problems and some of the known solutions to overcome them are discussed in the following.

Similar to any combustion device, biomass reactors and especially combustors can emit some harmful species into the environment, which has to be controlled. Compared to fossil fuels, biomass has the advantage of being $CO_2$-neutral so it has a lower contribution to global warming. However, biomass combustion can lead to harmful emissions such as $NO_x$, $SO_x$, and soot and unburned hydrocarbons. In this thesis, the main focus is on NO emissions and for other types of pollutants from biomass combustion, the readers are referred to the review by Williams et al. [13]. Nitrogen oxides which are produced in almost any combustion device are important because NO and $NO_2$ are acid rain precursors and participate in the generation of photochemical smog, and $N_2O$ is a greenhouse gas [14]. In biomass combustors, $NO_x$ can be formed from the atmospheric $N_2$ in the air (thermal and prompt pathways), or from the solid fuel-bound nitrogen (fuel-N). The fuel-N is known to be the dominant source of $NO_x$ from biomass, and oxygen availability and the nitrogen content of the fuel are among the most significant parameters affecting the $NO_x$ formation [14]. During biomass conversion, the fuel-N is released to the gas phase in the form of HCN, $NH_3$, and HNCO, which can later react in the gas phase to produce $NO_x$. The gas-phase reactions for formation and reduction of $NO_x$ in biomass combustors have been studied and detailed and skeletal reaction mechanisms have been proposed for the simulation of this process [15, 16, 17]. Three main methods are used for the reduction of NO emissions which are the use of low $NO_x$ burners or oxy-fuel combustion, selective non-catalytic reduction (SNCR), and selective catalytic reduction

(SCR) [18, 14]. In the first method, the temperature field and the mixing with oxygen are controlled in the burner to minimize the NO emissions. In SNCR, ammonia is injected at a specific temperature range in the burner which reacts with NO to form other N-containing species such as $N_2$. SCR is similar to SNCR but it is applied to the flue gas at a lower temperature, and a catalyst is used to enhance the ammonia reactions. SCR is very effective in NO reduction and is widely used in the exhaust system of motorcars, but the alkali metals from biomass can react with the catalyst leading to its deactivation. For this reason, SNCR becomes more appropriate for biomass combustion, and this method is examined as a part of this study.

Biomass has a relatively higher content of alkali metals compared to coal. Especially, biomass has a high potassium (K) content, which together with other elements such as chlorine (Cl) and Sulfur (S), can cause a lot of problems such as fouling, slagging, corrosion, and agglomeration of bed media [19]. The K-Cl-S elements from biomass can release into the gas phase in the form of KCl which is highly corrosive and $K_2SO_4$ which facilitates aerosol formation [20]. The release of K-containing species (called K-release for brevity) is a complicated process and is dependent on many parameters. The type of biomass and composition of ash-forming elements play an important role because some elements such as Cl, Magnesium (Mg), and Calcium (Ca) facilitate, and others such as Silicon (Si) or Aluminum (Al) prohibit the K-release [21]. The occurrence form of the elements is also important because they are available in both organic and inorganic forms, and each form follows a different pathway for transformation and release [22]. The major part of K in different types of biomass is in the form of inorganic salt namely KCl, $K_2CO_3$, and $K_2SO_4$. Conversion of biomass at high temperature increases the evaporation rate of inorganic salts and high $H_2O$ concentration increases the dissociation rate of $K_2CO_3$ and $K_2SO_4$ which leads to KOH formation [21]. The release of inorganic salts is highly important in entrained flow gasifiers (EFG) because the temperature and $H_2O$ concentration are very high in this type of reactor. Other known parameters that are effective on the K-release are the size and structure of the particles which affects the diffusion rate, and also the conversion atmosphere where combustion in $O_2$ increases and gasification in $CO_2$ decreases the K-release from biomass [22].

The carbon conversion efficiency and the composition of the products are among the most important parameters of interest in biomass conversion, especially in gasifiers. The case of biomass combustion is quite straightforward because, in ideal conditions, all of the char and volatiles are oxidized in combustors, so the major products will be a mixture of $CO_2$, $H_2O$, $O_2$, and $N_2$. The mass fraction of combustion products can be determined based on the C, H, and O content of the original fuel. In pyrolysis, the gas-phase products are highly sensitive to temperature and heating rate. A higher heating rate generally leads to lower tar and char and a higher gas produc-

tion [8]. Furthermore, more hydrogen will be released to the gas phase by pyrolysis at higher temperatures [23] which is important for the production of $H_2$ or $H_2$-rich mixtures. In biomass gasifiers, both carbon conversion and gas-phase products are important, which are both dependent on the type of the device and operating conditions. In fixed bed gasifiers the residence time of the particles are high and in the EFGs the temperature is high, so near complete carbon conversion is expected in both devices [9]. However, additional care is required in the operation of a fluidized bed gasifier to achieve a high carbon conversion, because of the moderate temperature and residence time [9]. The gas composition that is produced in a gasifier is dependent on the temperature, heating rate, particle size and residence time, and the partial pressure of the gasifying agent. One of the main challenges in biomass gasifiers is to produce a gas mixture that is rich in CO and $H_2$ (syngas), that can be used as a fuel in other devices.

Further research is still required to improve biomass conversion devices in regard to pollutant emissions, alkali release, and product composition. Experimental measurements and numerical modelling are the main two methods which are used to increase the current knowledge in this field. Performing experiments provides reliable information on the matter, but the experiments are usually expensive and only a limited number of variables can be measured in each experiment. Numerical modelling is an alternative approach which complements the experimental measurements. Model predictions have to be compared with some experimental data for validation of the model. After that, the model can be used to extract more information about the process or be used to improve the design or operating conditions of the device. The most recent numerical models from the literature which are relevant to the objectives of this thesis are summarized in the next section.

## 1.4   Numerical modelling

Biomass conversion is a multi-scale problem and various types of numerical models are developed each with a focus on a specific range of time and length scales. The span of scales involved in biomass conversion is very wide, ranging from fast reactions in micro-pores of the solid to very slow char conversion of large particles in an industrial reactor. The numerical models that are used for the study of biomass conversion can be categorized into particle, bed, and reactor models. In all models, a kinetic model is required to simulate the reactions at different scales. A brief overview and the recent advances in these models are presented in the following.

Single particle models are used to study the thermophysical phenomena inside and around a single biomass particle. The particle models are categorized into two

groups based on the conversion regime which is determined by Biot number (Bi), the ratio of the convective to conductive heat transfer in the particle [24]. The small particles that have Bi≪1 are converted in a thermally thin regime, which means the temperature inside the particle is almost uniform. This considerably simplifies the thermally thin particle models because the particle conversion becomes dependent on a single temperature. In this case, no spatial discretization is required inside the particle and all governing equations are expressed as Ordinary Differential Equations (ODE) with time as the only independent variable. On the other hand for larger particles in the thermally thick regime that have a Bi≫1, the process is more complicated because the intra-particle heat and mass transfer cannot be neglected. In that case, spatial discretization is required to solve the partial differential equations (PDEs) governing the conversion of the particles. Interface-based [25] and mesh-based methods [26, 27] are the two main approaches used for single particle modelling. The mesh-based models are generally more accurate than interface-based models at the expense of a higher computational cost. The mesh-based modelling can be carried out using a 1D [28], 2D [29], or 3D [30] domain. The 2D and 3D simulations can include the anisotropic characteristics of wood (such as heat and mass diffusion and shrinkage) and they can be easily coupled to CFD solvers to model the gas-phase reactions around the particle. One of the main challenges in the simulation of the particle and the surrounding gas phase is the significant difference between the time scales of the particle conversion and the combustion of volatiles around the particle. Different types of particle models can be used in the simulation of the bed or the freeboard of a biomass reactor.

Bed models are required for the simulation of biomass conversion in a fixed or moving grate reactor. In most studies, the models have been developed for a batch (packed bed) reactor, because for a moving grate, the distance travelled over the bed can be converted to the time spent in a packed bed [31]. The most simple approach to model the bed is the so-called porous bed model [32, 33]. In the porous bed model, the bed is considered as a homogeneous media and is discretized (usually one-dimensional) in a way that all fuel particles in a grid cell are assumed to be at the same temperature. The temperature gradient inside the particles is neglected in this method, which is a reasonable assumption for small particles in the thermally thin regime. However, relatively large particles in the thermally thick regime are converted in fixed-bed reactors, so the intra-particle gradients cannot be neglected [34]. To overcome this problem, simplified and fast-solving interface-based particle models are developed to be coupled to the bed model [35, 36, 37]. More expensive mesh-based particle models are also used in some bed simulations, but a coarse grid is used for both the bed and the particle to make the simulation possible [38]. In general, the main challenge in bed simulations is the high computational cost of the models. Therefore, it is not easy to include detailed particle models, detailed chemistry, or 2D

or 3D discretization in the bed model. Such details are important in some studies such as the simulation of channelling problem in the bed [39]. More research has to be done and new methods have to be developed to allow adding more details to the bed simulations. A bed model can be coupled to a CFD solver of the freeboard to have a complete model of the fixed-bed reactor. Different types of reactor-scale models are introduced in the following.

The largest scale of biomass conversion modelling is the CFD simulation of biomass reactors. The kinetic, particle, and bed models (for fixed bed reactors) can all play a part in a comprehensive model of a biomass conversion device. Modelling of the fluidized bed and entrained flow reactors are considerably different from fixed bed reactors. In fluidized bed and entrained flow reactors, the most common approach is to use an Eulerian-Lagrangian approach [40, 41, 42]. In this approach, the dispersed biomass particles are tracked in Lagrangian and the continuous fluid phase is modelled in the Eulerian frame of reference. Since the particle size is relatively small in entrained flow and fluidized bed reactors, the thermally thin particle models are commonly used in their simulations. The simulation of fixed bed reactors is different in the sense that particles are stationary (or moving with the grate). It is possible to model the fixed bed reactors with different strategies. The first approach is to model the bed separately to get an estimate of the volatiles that enter the freeboard (as a function of time, or steady-state conditions). Then the mass flow and concentration of the volatiles can be used as a boundary condition for CFD simulation of the freeboard [43, 44]. A more advanced method which has a higher computational cost is to couple a bed model directly to the CFD solver to simultaneously model the reactions in the bed and freeboard [45, 46]. By this method, a two-way coupling of bed and freeboard is possible so the effects of gas-phase reactions on the bed can also be included in the model. Reactor scale simulations are commonly carried out to study the overall performance of the reactor or the composition of the product mixture, especially in fluidized bed reactors [41]. More research is still required on pollutant emissions and potassium release, and the possible methods to reduce the problems associated with them.

In all of the mentioned models at different scales, kinetic models are required to simulate the reactions related to conversion of solid particles or the gas phase. Some of the kinetic models related to solid particle conversion are the simple and detailed pyrolysis mechanisms [47, 25, 23] and the char oxidation and gasification kinetic models [5]. Furthermore, over the past few years, single-step and multi-step kinetic models are developed for the release of potassium from solid biomass, e.g., the recent models developed in our group [48, 49, 50]. For the gas-phase reactions kinetic models are developed for tar cracking and combustion, NO emissions, and gas-phase potassium chemistry. A detailed kinetic model is developed by the CRECK mod-

elling group for the decomposition and combustion of complicated volatile mixtures [51]. This reaction mechanism involves 486 species and more than 16,000 reactions and is computationally expensive for CFD simulations. However, a compact and reduced kinetic model is derived based on the CRECK mechanism for the decomposition of tar species in an inert atmosphere which is suitable for CFD simulations as well [52]. Detailed [15] and skeletal [16, 17] kinetic models are developed to study the nitrogen chemistry during biomass combustion. A detailed kinetic model is proposed for the gas-phase reactions of K-Cl-S species [53] and a skeletal model is developed later which can be implemented in CFD simulations [54]. Selecting the appropriate kinetic model is an important step in numerical modelling of biomass conversion, because in general, more detailed kinetic models lead to more reliable results at the expense of a higher computational cost.

Based on the above discussion, significant studies were dedicated to the modelling of biomass conversion over the past few decades. However, there are still some research gaps which require further studies. Some of the research gaps that are investigated in this thesis are: (1) more detailed particle models which include the effects of anisotropic wood properties and wood non-homogeneities are still needed for thick particles; (2) the release of K-Cl-S from biomass at different operating conditions is not very well known; (3) NO emissions and possible methods for the reduction of NO emissions from biomass devices have to be studied; and (4) more advanced bed models are required to study the fixed-bed reactors in more details. In the next section, the main contributions of this thesis regarding the mentioned research gaps are discussed.

## 1.5    Thesis contribution

The main objectives of the present thesis are to further develop the numerical models and use the models to study the biomass conversion process. Each paper included in this thesis covers a part of the knowledge gaps discussed in the last section. The main contribution of the thesis through each paper is presented as follows.

In **Paper I**, a detailed mesh-based, multi-region particle model is developed and used for the study of single particle pyrolysis and combustion in a thermally-thick regime. The proposed model can predict the temperature distribution inside the particle, the products of conversion, and temporal mass loss of the particle during various stages of conversion, i.e., drying, pyrolysis, and char combustion. The model is extensively validated against various experimental measurements from the literature and then is used to study the effects of anisotropic heat conductivity in the model and also a possible solution to the stiff problem of coupling the particle model to the surround-

ing gas phase simulation. In **Paper II**, the same particle model is used to study the stages of hydrogen release during biomass pyrolysis. A novel anisotropic shrinkage model is proposed which correlates the particle shrinkage to the conversion of cellulose, hemicellulose, and lignin, which are the main components of the wood cell walls. The model is developed based on the temporal measurement of the axial and radial dimensions of wood dowels during pyrolysis up to 1273 K. Using the model, pyrolysis is divided into four different stages with different characteristics related to hydrogen release and gas phase products.

Another contribution of the thesis is related to the development and validation of a new detailed model for the release of K-Cl-S species from biomass, which is presented in **Paper III**. The model involves 12 solid species and 13 reactions to simulate the main pathways of transformation and release of potassium species. The model prediction for different parameters related to potassium release is compared and validated against different experiments from the literature. Three main parameters related to K-Cl-S release that can be predicted by the proposed model are: (1) the types of potassium (organic, inorganic, and stable) that remain in the solid after pyrolysis or combustion at different temperatures; (2) the residual mass fraction of K, Cl, and S in the solid after combustion at different temperatures; (3) the concentration of the gas phase K-containing species (atomic K, KCl, and KOH) at the vicinity of burning particles. The proposed model is coupled to a reactor scale CFD simulation of a 140 kW EFG to study the K-release during gasification and the results are presented in **Paper IV**. To the best of authors' knowledge, this was the first attempt to study the K-release in a biomass reactor using a detailed K-release model. In this paper, the gasification process and the main processes that are active at different locations inside the EFG are studied. The concentration of water and gas temperature inside the reactor and also the gas-phase composition at the gasifier outlet are compared against experimental measurements from an earlier study. On the other hand, the concentration of gas-phase K, KCl, and KOH is compared with experimental measurements to examine the validity of the K-release model in reactor scale simulations. Finally, the model is used to study the different stages and pathways of K-Cl-S release during the gasification process.

The last two papers that are included in this thesis are focused on the study of fixed-bed biomass combustion. In **Paper V**, the gas-phase reactions in the freeboard and NO formation and reduction are discussed. To model the boiler freeboard, the most common volatile (tar and gas) species from biomass pyrolysis are identified using a detailed single particle model from an earlier work. A method is developed to estimate the mass fraction of volatile species right above the bed in a way that satisfies the elemental and energy balance in the bed. Two reduced reaction mechanisms from the literature, one for tar decomposition and one for hydrocarbon combustion

and NO emissions, are coupled to study the gas-phase reactions in the reactor. The model predictions for major and minor species at different heights along the reactor are validated with experimental measurements from the literature. The possibility of SNCR for NO reduction in this specific boiler and the effective parameters on the performance of this method are investigated. In **Paper VI**, a tabulation-based model is developed for the simulation of the fixed bed reactors. The model is based on pre-processing the pyrolysis of thick particles in different conditions using the detailed particle model presented in **Paper I**. The temperature range for table generation is related to that in a fixed-bed reactor. The generated tables are used to include the intra-particle processes in the 2D bed model, without the need to run the computationally expensive particle model. The tabulation method is validated for the conversion of a single particle and three stacked particles and the results are compared to the detailed particle model. Finally, the tabulation method is used to model the combustion in a batch reactor and the temperature evolution and the flame propagation speed in the bed are compared with the experimental measurements. The bed model is coupled to a CFD solver of the freeboard to have a comprehensive model of a fixed bed reactor.

# Chapter 2

# Theory and modelling

Thermochemical conversion of biomass is a multi-scale problem and specific models have been developed and presented for each scale. In this chapter, the mathematical description of the different models that have been developed for the particle scale, potassium release, fixed bed, and freeboard simulations are presented.

## 2.1 Particle models

Biot number, Bi, is the ratio of convective to conductive heat transfer to a particle and is a decisive parameter in particle modelling. The Biot number can be defined as

$$\text{Bi} = \frac{h_{eff}d_p}{\kappa_p} \ , \tag{2.1}$$

where $d_p$ is the (equivalent) particle diameter and $\kappa_p$ is the conductivity of the solid particle. $h_{eff}$ is the effective heat convection coefficient, in which both the radiative and the convective heat transfer coefficients are considered. The convection coefficient can be calculated by the Nusselt number, Nu, and the radiation coefficient can be calculated based on the particle surface temperature, $T_{p,s}$, and the radiation source temperature, $\text{T}_{rad}$. Hence, the effective heat convection coefficient becomes [55]

$$h_{eff} = h_{conv} + h_{rad} = \frac{\text{Nu}\kappa_f}{d_p} + \sigma\epsilon\left(T_{p,s} + T_{rad}\right)\left(T_{p,s}^2 + T_{rad}^2\right) \ , \tag{2.2}$$

where $\kappa_f$ is the surrounding fluid conductivity, $\sigma$ is the Stefan–Boltzmann constant, and $\epsilon$ is the emissivity factor.

Based on the Biot number, the conversion of the particle is either in a thermally thin or thermally thick regime. The temperature gradient inside a thermally thin particle (Bi ≪ 1) can be neglected which simplifies the problem and the governing equations for the particle. This is not the case for larger particles in the thermally thick regime (Bi ≫ 1) and the temperature distribution inside the particle should be considered. In the following, the governing equations for both types of particles are presented. The thermally thin particle model is used in **Paper III** and **Paper IV** to study the potassium release from single biomass particles or in an EFG. The thermally thick particle model is developed and used in **Paper I** and is later used to study the anisotropic shrinkage and hydrogen release from a single particle in **Paper II**.

### 2.1.1 Thermally thin particle model

For particles in the thermally thin regime, all properties inside the particle can be considered uniform. Therefore, the governing equations for thin particles become a set of ODEs that are only a function of time. The mass balance and energy conservation equations for a thin particle can be expressed as

$$\frac{dm_p}{dt} = \dot{\Re}_{drying} + \dot{\Re}_{pyrolysis} + \dot{\Re}_{char} \,, \tag{2.3}$$

$$m_p c_p \frac{dT_p}{dt} = \dot{Q}_{conv} + \dot{Q}_{rad} + \dot{Q}_{drying} + \dot{Q}_{pyrolysis} + \dot{Q}_{char,s} \,, \tag{2.4}$$

where $m_p$, $c_p$, and $T_p$ are the mass, specific heat capacity, and temperature of the particle, respectively. $\dot{Q}_{rad}$ is the radiative heat transfer and is calculated by a radiation model, and the convective heat transfer to the particle can be calculated by

$$\dot{Q}_{conv} = h_{conv} A_p (T_g - T_p) \,, \tag{2.5}$$

where $A_p$ is the particle surface area, and $T_g$ is the gas temperature surrounding the particle. The other source terms in mass and energy equations are calculated through submodels for drying, pyrolysis, and char conversion, which are presented in Section 2.2.

The thermally thin particles are relatively small and in a fluidized bed or entrained flow reactors, they constantly move by the fluid flow. The momentum equation for the movement of the thin particles is in the form of

$$\frac{dm_p U_p}{dt} = f_{D,p} + g(1 - \frac{\rho_g}{\rho_p}) m_p \,, \tag{2.6}$$

where $m_p$, $\rho_p$, and $U_p$ are particle mass, density, and velocity vector, $f_{D,p}$ is the drag force vector and $g$ is the gravitational acceleration vector.

## 2.1.2 Thermally thick particle model

For the thermally thick particles, the temperature and other properties inside the particle are not uniform. Hence, the variables are dependent on both time and location and the governing equations are in the form of PDE. In this case, the equations and the computational domain have to be discretized and a computational grid is required. 2D and 3D grids can be used for spherical and cylindrical particles, such as those presented in Fig. 2.1a–d. Furthermore, the particle region can be coupled to the surrounding region as in Fig. 2.1e, based on the multi-region approach that is explained in **Paper I**. The governing equations for the thick particle model were presented and discussed in detail in **Paper I**, and a summary is also presented here.
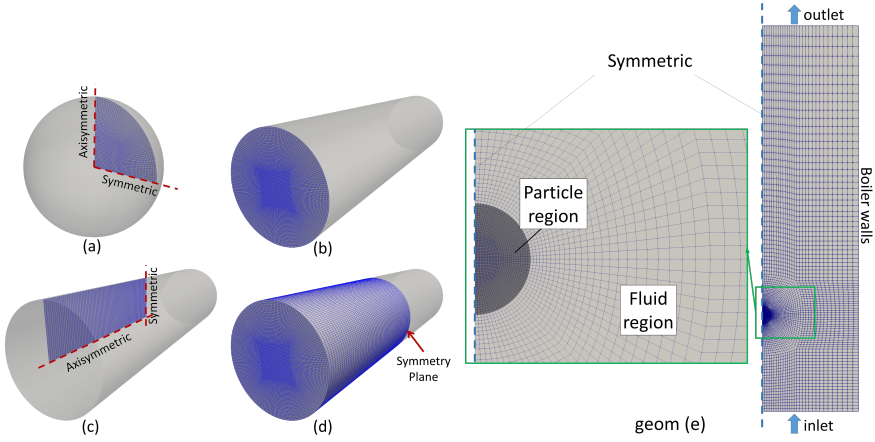


**Figure 2.1:** Different 2D and 3D grids used for uncoupled particle simulations (a–d) or coupled simulations (e).

The biomass particle is a porous media which can contain solid, liquid, and gas phases at the same time. At low temperatures before the moisture content of the particle evaporates, the liquid water is trapped within the pores of the particle, and its movement can be neglected. Neglecting the movement of liquids within the pores, the governing equations for the solid and liquid phases become similar. The mass balance equation for the solid and liquid species can be expressed as

$$\frac{\partial \rho_{s,i}}{\partial t} = \dot{\Re}_{s,i} \, , \tag{2.7}$$

and the continuity equation for the gas phase is

$$\frac{\partial}{\partial t} \left( \varepsilon \rho_g \right) + \nabla \cdot \left( \varepsilon \rho_g U \right) = \dot{\Re}_g \, . \tag{2.8}$$

In the above equations, $\rho_{s,i}$ is the density of the $i$'th solid or liquid species and $\dot{\Re}_{s,i}$ is the source term for the same species due to drying, pyrolysis, or char conversion

reactions. $\rho_g$ and $U$ are the density and velocity vector of the gas phase inside the particle, and $\dot{\Re}_g$ is the total gas formation due to particle conversion. The total gas formation rate is equal to the sum of the formation rate of different gas-phase species,

$$\dot{\Re}_g = \sum_{j=1}^{N_{gas}} \dot{\Re}_{g,j} \,, \tag{2.9}$$

where $\dot{\Re}_{g,j}$ is the formation rate of $j$th gas-phase species due to particle conversion.

The fluid velocity vector inside the particle can be estimated by the Darcy equation,

$$U = -\frac{K}{\mu}\nabla p \,, \tag{2.10}$$

where $p$ and $\mu$ are the gas pressure and dynamics viscosity, respectively, and $K$ is the permeability of the particle which can be calculated based on the pore diameter, $d_{pore}$, and local porosity inside the particle, $\varepsilon$, using [56]

$$K = \frac{d_{pore}^2 \varepsilon^3}{180(1-\varepsilon)^2} \,. \tag{2.11}$$

Various gas-phase volatiles are produced during the particle conversion and the transport equation for the volatiles inside the porous particle can be expressed as

$$\frac{\partial}{\partial t}\left(\varepsilon\rho_g Y_j\right) + \nabla \cdot \left(\varepsilon\rho_g U Y_j\right) = \nabla \cdot \left(\rho_g D_{eff,p}\nabla Y_j\right) + \dot{\Re}_{g,j} \,, \tag{2.12}$$

where $Y_j$ is the mass fraction of the $j$th volatile species and $D_{eff,p}$ is the effective pore diffusivity.

The local thermal equilibrium assumption is considered in the model meaning that the three phases of solid, liquid, and gas have the same temperature, $T$, at each specific location inside the particle. Hence, one energy equation can be solved for the whole particle, which is expressed as

$$\left(\rho c_p\right)_{tot} \frac{\partial T}{\partial t} + \varepsilon\rho_g c_{p_g} U \nabla T = \nabla \cdot \left(\kappa_{eff}\nabla T\right) + \dot{Q}_{reac} \,, \tag{2.13}$$

where $c_{p_g}$ is the heat capacity of the gas mixture and $\dot{Q}_{reac}$ is the heat generation due to particle conversion. The derivation of the energy equation for the solid particle is presented in Appendix A.1. $\left(\rho c_p\right)_{tot}$ can be calculated as

$$\left(\rho c_p\right)_{tot} = \varepsilon\rho_g c_{p_g} + \rho_s c_{p_s} = \varepsilon\rho_g \sum_{j}^{N_{gas}} Y_j c_{p_j} + \rho_s \sum_{i}^{N_{solid,liquid}} Y_{s,i} c_{p_i} \,. \tag{2.14}$$

The $\kappa_{eff}$ in Eq. 2.13 is the effective heat conductivity in the porous media which includes conduction and pore radiation by

$$\kappa_{eff} = \kappa_{cond} + \kappa_{rad} \, , \tag{2.15}$$

where

$$\kappa_{cond} = \varepsilon \kappa_g + (1 - \varepsilon) \kappa_s = \varepsilon \sum_{j}^{N_{gas}} Y_j \kappa_j + (1 - \varepsilon) \sum_{i}^{N_{solid,liquid}} Y_{s,i} \kappa_i \, , \tag{2.16}$$

and

$$\kappa_{rad} = \frac{\varepsilon \sigma T^3 d_{pore}}{\epsilon} \, . \tag{2.17}$$

In the above equation, $\epsilon$ is the local emissivity inside the particle pores which can be calculated as a mass-weighted average of the emissivity of different solid components, i.e., biomass, char, and ash, so that

$$\epsilon = \sum_{i}^{N_{solid}} Y_{s,i,dry} \epsilon_i \, . \tag{2.18}$$

More details on the thick particle model and also the parameters that are used in the model are presented in **Paper I**.

## 2.2 Submodels for particle conversion

Biomass particles in both thermally thin and thermally thick regimes undergo three main stages of conversion that are drying, pyrolysis, and char conversion. The main difference between thin and thick particles is related to the temperature distribution inside the particle, which significantly affects the progress rate of all stages of conversion. Therefore, the local temperature inside the particle should be used for the thick particles, and the particle temperature, $T_p$, for the thin particles. On the other hand, the progress of char conversion is also controlled by mass diffusion to the particle, which is handled differently for thin and thick particles. The details of the conversion submodels that are used in different papers are presented in the following.

### 2.2.1 Drying

Drying is the first stage of biomass conversion, during which the moisture content of the biomass is evaporated and released into the surrounding. Three types of drying

models are used in the literature, i.e., the heat flux, equilibrium, and chemical reaction models [27]. It was found that the three methods lead to very similar predictions, especially at higher temperatures [27]. So it is intuitive to use a method that is easier to implement in the simulation. A brief description of the equilibrium and chemical reaction methods, which are used in different parts of this thesis, is presented in the following.

The chemical reaction model is a simple and stable model for particle drying, and it is used in **Paper I** and **Paper II** to model the drying of thick particles. In this model, evaporation is considered as a reaction to convert the liquid water to water vapour, where the reaction rate per unit mass is expressed in the Arrhenius form,

$$r = A exp\left(-E/(R_u T)\right) \ [1/s] \ , \tag{2.19}$$

where A and E are the pre-exponential factor and the activation energy of the reaction, respectively. Here, rate constants of $A = 5.13 \times 10^{10}$ [1/s] and $E = 88$ [kJ/mol] are used to model the drying [57].

The equilibrium model is slightly more advanced than the chemical reaction model and is used in **Paper III** and **Paper IV** to model the drying of thin particles. In this model, the drying rate is estimated by

$$\dot{\Re}_{drying} = h_m A_p M_{water}(C_{water,S} - C_{water,g}) \ [kg/s] \ , \tag{2.20}$$

where $h_m$ is the mass convection coefficient, $A_p$ is the particle surface area, and $M_{water}$ is the molecular weight of water. $C_{water,S}$ and $C_{water,g}$ are the water vapour concentration at the particle surface and in the gas phase surrounding the particle, respectively. The $C_{water,S}$ is calculated by the saturation vapour pressure of the water at the particle surface temperature.

For both models, the heat of drying can be calculated based on the drying rate by $\dot{Q}_{drying} = \dot{\Re}_{drying}\Delta h_{vap,water}$, where $\Delta h_{vap,water}$ is the latent heat of water evaporation.

## 2.2.2 Pyrolysis

Pyrolysis or devolatilization is an important stage of conversion, during which between 60–90% of the particle mass is released as volatiles, and the rest remains in the solid state in the form of char and ash. The pyrolysis rate and products are highly sensitive to temperature, and different mechanisms are proposed in the literature to model pyrolysis. The pyrolysis models used in this thesis can be categorized into a one-step single reaction, three competing reactions, and detailed multi-step models. A schematic representation of the three pyrolysis models is presented in Fig. 2.2. The kinetic rate constants for the first two models are presented in Table 2.1.

$$Biomass \xrightarrow{k_1} \alpha_1.Gas + \alpha_2.Tar + \alpha_3.Char$$

(a)

$$Biomass \xrightarrow{k_2} Gas$$
$$Biomass \xrightarrow{k_3} Tar$$
$$Biomass \xrightarrow{k_4} Char$$

(b)

$$Biomass \begin{cases} CEL \rightarrow Volatile, Char, MET \\ HCE \rightarrow Volatile, Char, MET \\ LIG \rightarrow Volatile, Char, MET \\ EXT \rightarrow Volatile, Char, MET \end{cases}$$

(c)
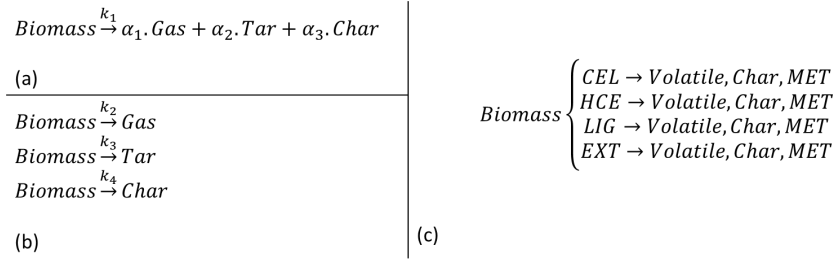
**Figure 2.2:** Different schemes for pyrolysis of lignocellulosic biomass. Single reaction (a), three competing reactions (b), and detailed multi-step (c) schemes.

**Table 2.1:** Pyrolysis kinetic rate constants for the single reaction and three competitive reaction models.

| | $A_i$ [1/s] | $E_{ai}$ [kJ/mol] | Ref. |
|---|---|---|---|
| Single reaction: | | | |
| $k_1$: | $1.73 \times 10^6$ | 106.5 | [58] |
| Three competitive reactions: | | | |
| $k_2$: | $4.4 \times 10^9$ | 153 | [47] |
| $k_3$: | $1.1 \times 10^{10}$ | 148 | [47] |
| $k_4$: | $3.3 \times 10^6$ | 112 | [47] |

In the one-step single reaction model, the biomass is converted to gas, tar, and char through a single reaction. The mass fraction of pyrolysis yields, i.e., $\alpha_1$–$\alpha_3$, are the model inputs which should be predicted by experiments or other more advanced models. This model is the most simple pyrolysis model with the lowest computational cost. Therefore, it is commonly used for simulations in the reactor scale where a large number of particles are involved. This pyrolysis model is used in the modelling of thin particle conversion in **Paper III** and **Paper IV**.

The three competitive reaction model is more advanced compared to the single reaction model, mainly because it can predict the gas, tar, and char yields relatively well. The main limitations of this pyrolysis model are that it is not dependent on the fuel type, gives no information about the composition of the gas-phase products, and it cannot predict the elemental composition of char at different temperatures. This model is used in **Paper I** to study the conversion of thermally thick particles, and its performance is compared against the detailed pyrolysis model.

The most advanced pyrolysis model for lignocellulosic biomass is a multi-step reaction mechanism that is developed over the years by CRECK modelling group [59, 60, 23]. In this model, the thermal decomposition of main biomass constituents, i.e., cellulose (CEL), hemicellulose (HCE), lignin (LIG), and extractives (EXT) are considered as presented in Fig. 2.2c. Each biomass component has its own decomposition rate and pathway, and it can be converted to volatiles, char, and intermediate

species such as metaplastic species (MET), during different stages of conversion. The initial composition of the biomass can be estimated based on the ultimate analysis of the fuel (C, H, O, and ash content). The main advantages of this model compared to earlier pyrolysis models are a more accurate pyrolysis rate at different stages of pyrolysis, detailed prediction of volatile species, ability to predict the elemental composition of the residual char, and more realistic prediction of the heat of pyrolysis. This model is used in both **Paper I** and **Paper II** for detailed analysis of biomass pyrolysis. The main limitation of this model is its high computational cost, so it is cannot be easily implemented in reactor scale simulations. Nevertheless, the single particle simulations with the detailed pyrolysis model can be used as a pre-processing step to predict the volatile composition, for instance, in the one-step single reaction pyrolysis model.

### 2.2.3 Char conversion

The heterogeneous char conversion can take place after biomass pyrolysis through the reactions that are presented in Table 2.2. Depending on the atmosphere, the solid char can react with oxidizing agent $O_2$ (combustion), or gasifying agents $H_2O$, $CO_2$, and $H_2$ (gasification). The gasification with $H_2$ is very slow in atmospheric gasifiers and it can be neglected in many cases [9]. Based on reaction R1, char can react with oxygen to produce CO and $CO_2$. The ratio of CO to $CO_2$ during char combustion is determined by $\Omega_C$ which is a function of temperature [61, 25]

$$\Omega_C = \frac{2\left(1 + 4.3 exp[-3390/T]\right)}{2 + 4.3 exp[-3390/T]}. \tag{2.21}$$

The char conversion rate or char reactivity is defined as

$$r_m = -\frac{1}{m_C}\frac{dm_C}{dt} = \frac{1}{1 - X_C}\frac{dX_C}{dt} \text{ [1/s] }, \tag{2.22}$$

where $X_C = 1 - m_C/m_{C0}$ is the char conversion and $m_C$ and $m_{C0}$ are current and initial mass of char, respectively. The char reactivity per unit mass is presented in Eq. 2.22 but the char reactivity per unit surface area, $r_A$ [kg/(m$^2$ s)] is also commonly used in the literature [9]. The two types of reactivity are correlated by

$$r_m = A_m r_A \text{ [1/s] }, \tag{2.23}$$

where $A_m$ [m$^2$/kg] is the total active surface area per unit mass. The active surface area of char changes during conversion, and is reported in the general form of $A_m = A_{m0}F(X_C)$, where different functions of $F(X_C)$ are proposed in different studies [5].

The heterogeneous char conversion reactions are more complicated in nature than the pyrolysis reactions. The pyrolysis reactions are mainly controlled by temperature, while many factors related to both kinetics and mass diffusion are effective on char reactivity. The kinetic rate of heterogeneous reactions is sensitive to the temperature, active surface area of char, partial pressure of the gas-phase reactant, and also the catalytic effects of inorganic matter such as potassium [5]. The mass diffusion of the gas-phase reactant or the products can be limited externally or internally. The external mass diffusion is dependent on the particle size and the surrounding flow parameters such as velocity, reactant concentration, and temperature. On the other hand, the internal diffusion rate is affected by the morphological structure of the biomass which constantly changes during conversion. Based on the above discussion, three different regimes can be defined for the char conversion: Regime I which is controlled by kinetics; Regime II which is controlled by internal or pore diffusion; and Regime III which is controlled by the external diffusion [62, 5, 9]. Only the experiments in Regime I leads to the measurement of the intrinsic kinetic rates of char conversion, as opposed to measurements in Regime II and III which provide the overall reactivity of the char. It was found that the effects of diffusion cannot be neglected even in particles as small as 60 $\mu$m, so most of the experiments in literature are performed to measure the overall char reactivity [5].

The kinetic rates of the char oxidation and gasification are commonly presented in a general form of [5]

$$r_{m,kin,i} = A_i T^{\beta_i} exp\left(-E_i/(R_u T)\right) p_i^{n_i} F(X_C) \text{ [1/s] },\qquad(2.24)$$

or in some cases, the more simple form of [26]

$$r_{m,kin,i} = A_i T exp\left(-E_i/(R_u T)\right) C_i F(X_C) \text{ [1/s] },\qquad(2.25)$$

where $i$ is the gas-phase reactant ($O_2$, $CO_2$ or $H_2O$) and $p_i$ and $C_i$ are the partial pressure or concentration of the same reactant surrounding the particle. It should be noted that both the overall or intrinsic reactivity of char can be presented in the form of the above equations. The best approach for char conversion modelling is to use the intrinsic kinetic rate and model the diffusion rate separately. Different approaches can be used to model the diffusion rate in thermally thin and thermally thick particles.

In the thick particle models (**Paper I**), the diffusion of the gas-phase reactant to the surface of the particle is modelled using the Stefan flow correlations [63]. The diffusion inside the particle is modelled by solving the species transport equation, which is affected by the local porosity inside the particle.

For thermally thin particles (**Paper III** and **Paper IV**) a kinetic-diffusion limited model is used to calculate the overall char conversion rate. The kinetic-diffusion limited model is commonly used in the literature [40, 64] and it can be expressed in the

general form of

$$r_{m,i} = \frac{r_{m,dif,i} r_{m,kin,i}}{r_{m,dif,i} + r_{m,kin,i}} \ [1/s] \ , \tag{2.26}$$

where $r_{m,i}$ is the reactivity of char due to reactions with gas species $i$ and $r_{m,dif,i}$ is the char conversion rate per unit mass [1/s] limited to the external diffusion rate, which can be calculated by

$$r_{m,dif,i} = \frac{A_p p_i}{m_C} \frac{C_i \left(0.5(T_g + T_p)\right)^{0.75}}{d_p} \ [1/s] \ . \tag{2.27}$$

In Eq. 2.27, $C_i = 4 \times 10^{-12} \nu_{C,i}$ [s/K$^{0.75}$] is calculated based on the diffusion coefficient, and $\nu_{C,i}$ is the stoichiometric ratio of char to the gas-phase reactant (Calculations in Appendix A.3). Following the literature, two different sets of kinetic rates are used for thin and thick particles, which are presented in Table 2.2.

**Table 2.2:** Kinetic rate of heterogeneous oxidation and gasification reactions. Units in [Pa-J-kmol-m-s-K].

|    | Heterogeneous reactions | |
|----|---|---|
| R1 | $\Omega_C$ C + O$_2$ → 2($\Omega_C$ - 1) CO + (2-$\Omega_C$) CO$_2$ | |
| R2 | C + CO$_2$ → 2 CO | |
| R3 | C + H$_2$O → H$_2$ + CO | |
|    | Thin particles, $r_{m,kin,i}$ [1/s] | ref. |
| R1 | $7.06 \times 10^5 P_{O_2}^{0.78} exp(-160 \times 10^6/(R_u T))(1 - X)$ | [65] |
| R2 | $3.62 \times 10^4 P_{CO_2}^{0.8} T^{-0.8} exp(-166 \times 10^6/(R_u T))(1 - X)^{2/3}$ | [66] |
| R3 | $1.773 \times 10^3 P_{H_2O}^{0.41} exp(-179 \times 10^6/(R_u T))$ | [67] |
|    | Thick particles, $r_{m,kin,i}$ [1/s] | ref. |
| R1 | $0.658 M_C/\rho_C \nu_{C,i} C_{O_2} S_a T exp(-74.8 \times 10^6/(R_u T))$ | [61] |
| R2 | $3.42 M_C/\rho_C C_{CO_2} S_a T exp(-130 \times 10^6/(R_u T))$ | [68] |
| R3 | $3.42 C_{H_2O} M_C/\rho_C S_a T exp(-130 \times 10^6/(R_u T))$ | [68] |

## 2.2.4 Shrinkage

The biomass particles shrink during various stages of thermochemical conversion. The particle shrinkage is important because it affects the size, density, and porosity of the particle, hence the heat and mass transfer to the particle. In the case of thermally thin particles, a simple assumption of constant density is used for simulations. This means the particle volume changes at the same rate as particle mass loss. However, a more advanced shrinkage model is used for the simulation of thermally thick particles. In the case of nearly isotropic particles such as wood pellets, it is assumed that the shrinkage is also isotropic but the volume change is different at various stages of

conversion. Hence, an empirical correlation is used in **Paper I** to calculate the local shrinkage factor, $\theta = \dfrac{V}{V_0}$ [27],

$$\theta = 1 + (1 - \theta_M)(\frac{\rho_M}{\rho_{M,0}} - 1) + (\theta_M - \theta_B)(\frac{\rho_B}{\rho_{B,0}} - 1) + (\theta_B - \theta_C)(\frac{\rho_C}{\rho_{C,0}} - 1) \ , \quad (2.28)$$

where subscripts $M$, $B$ and $C$ correspond to moisture, biomass and char, respectively. The $\rho_{M,0}$ and $\rho_{B,0}$ are the apparent densities at the start of conversion and $\rho_{C,0}$ is the apparent char density after the pyrolysis stage is finished. $\theta_M$, $\theta_B$ and $\theta_C$ are empirical model constants varying between 0 and 1.

The shrinkage of lignocellulosic biomass which has anisotropic properties is more complicated and is highly dependent on the structure of the wood cell walls. Based on some earlier observations [69, 70] and also some experimental results presented in **Paper II**, it was found that wood shrinkage can be different in axial (along the grain) and radial (normal to grain) directions, and also the shrinkage rate is different during decomposition of different wood components (cellulose, hemicellulose, and lignin). Therefore, a new anisotropic shrinkage model is developed in **Paper II** which is explained in the following.

The longitudinal shrinkage vector, $\vec{\beta}$, is defined as the particle length to its initial length, in each of the $x$, $y$, and $z$ Cartesian directions. Here we have defined $z$ as the axial direction (along the grain) of the particle, and $x$ and $y$ are the radial directions. The $\vec{\beta}$ is related to the conversion of biomass constituents by

$$\vec{\beta} = \vec{I} - \sum_j \Delta\vec{\beta}_j \left( 1 - m_j/m_{j0} \right) \ , \quad (2.29)$$

where $j$ represents the particle constituents, i.e., moisture, CEL, HCE, LIG, EXT, MET, and char. $\vec{I}$ is a 1-vector, $\Delta\vec{\beta}_j$ is an empirical shrinkage vector for the decomposition of each constituent, and $m_j$ and $m_{j0}$ are the mass and initial mass of each constituent. More details regarding this shrinkage model are presented in **Paper II**.

### 2.2.5 K-release model

The most simple and common approach to model the K-release from biomass is to describe the release rate in the form of an empirical Arrhenius reaction rate. However, this approach requires experimental measurements for each specific fuel and operating conditions, because the release rate can be affected by several different factors. A new detailed K-Cl-S release model was developed and proposed in **Paper III** which is based on various experimental measurements over the past two decades. This model includes

12 solid-phase species and 13 reactions which are related to the main pathways of K-Cl-S transformation and release during biomass pyrolysis and combustion. The effects of fuel type and ash-forming elements, especially K, Cl, S, Si, Ca, and Mg, and also operating conditions, such as temperature and $H_2O$ concentration are included in the model. A summary of the reactions and the proposed kinetic rates are presented in Table 2.3. Further details regarding the procedure and assumptions that led to this model, model validation, and the main limitations of the model are presented in **Paper III**. The model is also used in **Paper IV** to study the K-release in an EFG, and the results are compared with the experimental measurements by our collaborators [71].

**Table 2.3:** Reactions and the reaction rates used to model the transformation and release of K, Cl, S, and Si-containing species from **Paper III**, units in [kg-J-kmol-m-s-K].

|     | Reaction | rate |
| --- | --- | --- |
| R1  | $K_{inorganic} \rightarrow \phi_1 KCl + \phi_2\ K_2SO_4 + \phi_3\ K_2CO_3$ | $5.13 \times 10^{10} \exp(-88 \times 10^6/(R_u T))$ |
| R2  | $S^{2-} \rightarrow S_{crystal}$ | $5.13 \times 10^{10} \exp(-88 \times 10^6/(R_u T))$ |
| R3  | $S_{crystal} \rightarrow SO_{2(g)}$ | $1.25 \times 10^{11} \exp(-125 \times 10^6/(R_u T))$ |
| R4  | $KCl + R\text{-}COOH \rightarrow R\text{-}COOK + HCl_{(g)}$ | $1.25 \times 10^{11} \exp(-125 \times 10^6/(R_u T))$ |
| R5  | $R\text{-}COOK \rightarrow char\text{-}K + CO_{2(g)}$ | $1.10 \times 10^7 \exp(-112 \times 10^6/(R_u T))$ |
| R6  | $R\text{-}COOK \rightarrow R + CO_{2(g)} + K_{(g)}$ | $4.40 \times 10^9 \exp(-153 \times 10^6/(R_u T))$ |
| R7  | $KCl \rightarrow KCl_{(g)}$ | $4.16 \times 10^7 \exp(-186 \times 10^6/(R_u T))$ |
| R8  | $K_2CO_3 \rightarrow 2K_{(g)} + CO_{2(g)} + 0.5O_{2(g)}$ | $3.25 \times 10^{12} \exp(-360 \times 10^6/(R_u T))$ |
| R9  | $K_2CO_3 + H_2O_{(g)} \rightarrow 2KOH_{(g)} + CO_{2(g)}$ | $3.25 \times 10^{14} \exp(-360 \times 10^6/(R_u T)) \cdot p_{H_2O}^n$ |
| R10 | $K_2SO_4 \rightarrow K_2SO_{4(g)}$ | $5.93 \times 10^6 \exp(-261 \times 10^6/(R_u T))$ |
| R11 | $K_2SO_4 + H_2O_{(g)} \rightarrow 2KOH_{(g)} + SO_{2(g)} + 0.5O_{2(g)}$ | $5.93 \times 10^8 \exp(-261 \times 10^6/(R_u T)) \cdot p_{H_2O}^n$ |
| R12 | $char\text{-}K \rightarrow \alpha\ K_2CO_3 + (1\text{-}\alpha)\ K_2SiO_3$ | $2.00 \times 10^7 \exp(-182 \times 10^6/(R_u T)) \cdot X_{char}$ |
| R13 | $K_2SO_4 + SiO_2 \rightarrow K_2SiO_3 + SO_{2(g)} + 0.5O_{2(g)}$ | $2.00 \times 10^6 \exp(-182 \times 10^6/(R_u T)) \cdot X_{char}$ |

## 2.3   Fixed bed model

The details of the fixed bed model developed in this study are presented in **Paper VI** and a summary is reported here. The main idea is to include more details in the bed model by separating the drying and pyrolysis stages from the char combustion stage. Then a tabulation method is proposed to model the drying and pyrolysis stage, while char combustion can be modelled by a relatively simple kinetic-diffusion limited model which was used in earlier studies.

### 2.3.1   Tabulation method for drying and pyrolysis

The major part of particle mass is released during the pyrolysis stage in the form of several different volatile species. However, a detailed particle model and a detailed

pyrolysis mechanism cannot be easily used in bed simulations due to their high computational cost. The particle drying and pyrolysis are governed by the heat transfer to the particle. Therefore, it is possible to preprocess the conversion of thick biomass particles in different thermal conditions and store the results in some tables that can be used for bed simulation. For this purpose, we have defined three variables which define the state of the particle and the heat transfer rate to the particle. The three variables are defined as

$$c_1 = m/m_0 \, , \tag{2.30}$$

$$c_2 = (T_s - T_{s,min})/(T_{s,max} - T_{s,min}) \, , \tag{2.31}$$

and

$$T_{eff} = \left( \frac{\dot{Q}_{tot,p}}{A_p \sigma \epsilon} + T_s^4 \right)^{1/4} . \tag{2.32}$$

In the above equations $c_1$, $c_2$, and $T_{eff}$ represent particle mass, surface temperature, and heat transfer to the particle, respectively. $m$ and $m_0$ are the particle mass and initial mass, respectively. $T_s$ is the particle surface temperature which changes from an initial value of $T_{s,min}$ to the maximum temperature in the reactor, $T_{s,max}$. $\dot{Q}_{tot,p}$ is the total heat transfer to the particle, $A_p$ is the particle surface area, $\sigma$ is the Stefan-Boltzmann constant, and $\epsilon$ is the emissivity of the particle surface. Based on $T_{eff}$ definition, a particle that absorbs $\dot{Q}_{tot,p}$, is similar to a particle that is exposed to a heating source with black body radiation at $T_{eff}$.

In the proposed tabulation method, it is assumed that the conversion rate is a function of the two progress variables $c_1$ and $c_2$, and the effective temperature $T_{eff}$. Therefore, the conversion of particles under different $T_{eff}$ conditions is simulated using the detailed particle model, and the variables of interest are stored in tables as a function of $c_1$ and $c_2$. For each particle in the bed, instead of using the detailed particle model, the total heat transfer to the particle $\dot{Q}_{tot,p}$ has to be calculated first to find the $T_{eff}$. Then the governing equations for the progress variables can be solved using the data from the tables. The governing equations for $c_1$ and $c_2$ can be expressed as

$$dc_1/dt = (dm/dt)/m_0 = -\dot{\Re}_{sg,p}/m_0 \tag{2.33}$$

and

$$dc_2/dt = (dT_s/dt)/(T_{s,max} - T_{s,min}) = \dot{T}_s/(T_{s,max} - T_{s,min}) . \tag{2.34}$$

In the above equations, the terms $\dot{\Re}_{sg,p}$ and $\dot{T}_s$ which determine the mass loss rate and surface heating rate will be extracted from the tables. Based on this approach, the particle surface temperature and mass loss rate which are the most important

parameters affecting the gas-phase domain are calculated quickly, without solving the time-consuming equations of the detailed particle model during the run time. The total heat transfer to the particle is dependent on the particle surface temperature $T_s$, and no information on the temperature distribution inside the particle is needed. $\dot{Q}_{tot,p}$ is calculated based on the convective, conductive, and radiative heat transfer to the particle, where the details are reported in **Paper VI**.

### 2.3.2 Other submodels for the fixed bed

During drying and pyrolysis, the outward flow of the volatiles from the surface of the particle (Stefan flow) prevents the oxygen to reach the char surface. Therefore, char combustion starts after the pyrolysis stage and the rate of char combustion can be limited by either the kinetics or the diffusion rate of oxygen. In the bed model, the char reactivity is described as in the Eq. 2.22, but the diffusion rate is calculated in a more general form compared to thermally thin particles. Since large particles are being converted in a fixed bed, and the fluid flow is relatively slow, diffusion through the ash layer should also be considered. For a spherical particle in a fixed bed, the mass transfer limited rate of char conversion can be expressed in the form of

$$r_{m,dif} = \left( \frac{1}{\pi d_2^2 h_m} + \frac{d_2 - d_1}{2\pi d_1 d_2 D_{ash}} \right)^{-1} \times \frac{M_C \rho_{O_2}}{M_{O_2} m_C} \times \frac{1}{\nu_{O_2}} \; [\text{1/s}] \; , \qquad (2.35)$$

where $d_1$ and $d_2$ are the char and particle diameters, respectively. $h_m$ is the mass convection coefficient, $D_{ash}$ is the effective diffusion coefficient in the ash layer, and $M_C$ and $M_{O_2}$ are the molecular weight of char and oxygen, respectively. The derivation of this equation and more details on the calculation of different terms are presented in Appendix A.3.

Other submodels that are required for the solid particles in the bed model are the convective and radiative heat transfer to the particle. The particle surface temperature is known because the transport equation for $c_2$ is being solved in the bed. The convective heat transfer to the particle is calculated by

$$\dot{Q}_{conv} = h_c S_A (T_g - T_s) \; , \qquad (2.36)$$

where $h_c$ is the heat convection coefficient, $S_A$ is the particle surface area, and $T_g$ is the gas temperature near the particle.

The radiative heat transfer from the reactor walls to the particles is calculated by Discrete Ordinate Methods (DOM) [72]. Since radiation is the main source of heating of the particles, an important parameter in the bed modelling is the absorption coefficient. The absorption of gas can be neglected compared to that in the bed of

solid particles [73]. The bed absorption/emission coefficient is calculated based on the volume scattering relation proposed by Brewster et al. [74] as a function of bed porosity and particle diameter

$$\kappa_{a,e} = \frac{1.5(1 - \varepsilon_b)}{\varepsilon_b d_p} \,, \tag{2.37}$$

where $\varepsilon_b$ is the bed porosity assuming non-porous particles. More details on the convection, radiation, and different definitions of porosity in the bed are reported in **Paper VI**. The governing equations for the fluid flow in the porous bed and also in the freeboard are presented in the next section.

## 2.4 Gas-phase model

The numerical modelling of the flow and reactions in a biomass reactor is different depending on the reactor type. In fixed bed reactors, the solid particles are located in the bed and they are not moving with the flow. In this case, the bed is considered as a porous media and the freeboard does not contain any solid particles. On the other hand, an Eulerian-Lagrangian model is required to model the fluid flow and particle movement in entrained flow or fluidized bed reactors. The type of gas-phase reactions to be considered in the model is also dependent on the device, the operating conditions, and the objectives of the study. In the next sections, first, the general form of the governing equations for the fluid phase in the porous bed and freeboard is presented, and then the different gas-phase reactions that are considered in different parts of this thesis are explained.

### 2.4.1 Fluid flow in porous bed and freeboard

The continuity, momentum, species transport, and energy equations for the fluid flow inside the porous bed are expressed in the following form:

$$\frac{\partial \varepsilon_b \rho}{\partial t} + \nabla \cdot (\varepsilon_b \rho U) = \dot{\Re}_{sg} \,, \tag{2.38}$$

$$\frac{\partial}{\partial t} (\varepsilon_b \rho U) + \nabla \cdot (\varepsilon_b \rho U U) = -\nabla \varepsilon_b p + \varepsilon_b \rho g + \nabla \cdot (\varepsilon_b \tau) - S_p \,, \tag{2.39}$$

where

$$\tau = \mu_{eff} \left[ (\nabla U + \nabla U^T) - \frac{2}{3} \nabla \cdot U I \right] \,, \tag{2.40}$$

29

$$\frac{\partial}{\partial t} \left( \varepsilon_b \rho Y_i \right) + \nabla \cdot \left( \varepsilon_b \rho U Y_i \right) = \nabla \cdot \left( \rho D_{eff} \nabla Y_i \right) + \dot{\Re}_{g,i} + \dot{\Re}_{sg,i} \,, \qquad (2.41)$$

and

$$\frac{\partial}{\partial t} \left( \varepsilon_b \rho h \right) + \nabla \cdot \left( \varepsilon_b \rho U h \right) + \frac{\partial}{\partial t} \left( \varepsilon_b \rho K_e \right) + \nabla \cdot \left( \varepsilon_b \rho U K_e \right) - \frac{\partial p}{\partial t}$$
$$= \nabla \cdot \left( \rho \alpha_{eff} \nabla h \right) + \dot{Q}_{rad} + \dot{Q}_{reac} + \dot{Q}_{char,g} - \dot{Q}_{conv} \,. \qquad (2.42)$$

In the above equations, $\rho$, $U$, $p$ and $h$ are density, velocity vector, pressure and the specific enthalpy of the fluid, respectively. $\dot{\Re}_{sg}$ is the gas production from the solid particles. In the momentum equation, $\tau$ is the total stress tensor, $g$ is the gravitational acceleration vector, and $S_p$ is the momentum source term from the particles. $Y_i$ is the mass fraction of the $i$'th species in the gas mixture and $\dot{\Re}_{g,i}$ and $\dot{\Re}_{sg,i}$ are the production rate of the same species due to gas phase reactions and particles conversion, respectively. In the energy equation, $K_e$ is the kinetic energy per unit mass and $\dot{Q}_{rad}$ is the radiation source term. $\dot{Q}_{reac}$ is the heat source due to gas phase reactions, $\dot{Q}_{conv}$ is the convective heat transfer from gas to the solid and $\dot{Q}_{char,g}$ is a share of the heat generated due to heterogeneous char reactions, which is directly transferred to the gas-phase. The derivation of the above equations is presented in Appendix A.2 and more details on the calculation of each term are presented in **Paper VI**.

The parameters $\varepsilon_b$, $\dot{\Re}_{sg}$, $\dot{\Re}_{sg,i}$, $S_p$, $\dot{Q}_{char,g}$, and $\dot{Q}_{conv}$ are involved in coupling the gas-phase equations to the solid-phase particles and their calculation is different in various parts of this thesis. Other than in the porous bed in **Paper VI**, $\varepsilon_b = 1$ is considered in the fluid flow in the other studies. In **Paper I** and **Paper V**, the gas phase reactions around a particle or in the freeboard above a fixed bed are studied. Therefore, the particle effects are only added to the fluid domain boundaries, so the source terms from the particles within the domain are zero. In **Paper IV**, small particles in the EFR are tracked with a Lagrangian frame of reference, and the source terms in the fluid region are calculated by a thermally thin particle model. For fixed bed simulations in **Paper VI**, the source terms from the particle are calculated based on the tabulation method and char combustion model that was explained in the previous section.

### 2.4.2 Gas-phase reactions

Different reaction mechanisms are used in different parts of the present work that are summarized in Table 2.4 and explained in the following. In **Paper I**, the GRI-Mech 3.0 [75] is used to model the combustion of volatiles surrounding a thick particle during pyrolysis. The focus in **Paper II** and **Paper III** are on the solid particles, so the gas-phase reactions are not considered in those studies. In **Paper IV** a set of global reactions that are commonly used in gasification simulations [76] are used. The global

reactions include the forward and backward water-gas shift reactions, and combustion of CO, $H_2$, $CH_4$, and $C_2H_6$. A new reaction mechanism is proposed for the simulations in **Paper V**, which is the combination of two other reduced mechanisms, i.e., Lovas [16] and Goyal [52]. The Lovas mechanism is used to model the combustion of $C_1$ and $C_2$ hydrocarbons and also NO emissions and reduction in a biomass combustor. The Goyal mechanism includes the pathways for the decomposition of heavy tar molecules to $C_1$ and $C_2$ species. The performance of the new combined mechanism is compared against the two original mechanisms for the main variables of interest to test the validity of the model. Finally, in **Paper VI** a new set of decomposition reactions for the tar species are introduced and a set of global reactions are used to model the combustion of gases. The method used to extract the tar decomposition reactions is briefly described in the following.

**Table 2.4:** Different gas-phase reaction mechanisms are used in various parts of the present study.

| Paper | Name of mechanism | Used for | ref. |
|---|---|---|---|
| **Paper I** | GRI-Mech 3.0 | Combustion of volatiles near particle | [75] |
| **Paper IV** | Global gasification reactions | Modelling the EFG | [76] |
| **Paper V** | Lovas | Combustion and NO emissions | [16] |
| | Goyal | Decomposition of tar species | [52] |
| **Paper VI** | Global tar decomposition | Decomposition of tar species | This study |
| | Global combustion reactions | Combustion of volatiles in freeboard | - |

A large variety of volatile species is released during the pyrolysis of biomass particles that has to be included in the gas-phase simulations. In an earlier study in our group, a set of global tar-cracking reactions was proposed [56], but the rate of decomposition of different species was unknown. In **Paper VI**, a detailed gas-phase reaction mechanism with 486 species and more than 16 thousand reactions [51] was used to estimate the decomposition rate of different tar species. The detailed kinetic model was used to propose a set of single-step global reactions for the volatile decomposition, which are presented in Table 2.5.

Perfectly Stirred Reactor (PSR) simulations are carried out to calculate the decomposition rate of each volatile species in an inert atmosphere at different temperatures between 600 to 1500 K. The major products of decomposition at high temperatures were CO and $H_2$ for most volatiles considered in this study. Other species such as $CH_4$, $C_2H_2$, $H_2O$, and $CO_2$ were also available in the products and used in the proposed reactions to satisfy the elemental balance [56]. Further details on the estimation of the reaction rate constants in Table 2.5 are presented in **Paper VI**.

**Table 2.5:** Global single step reactions for decomposition of the volatiles. Units in [kJ, mol, s].

| Reactions | A | Ea |
|---|---|---|
| $HCOOH \rightarrow 0.4H_2 + 0.6H_2O + 0.6CO + 0.4CO_2$ | 8.10E+14 | 282.8 |
| $CHOCHO \rightarrow H_2 + 2CO$ | 1.02E+14 | 220.4 |
| $CH_2OHCHO \rightarrow 2H_2 + 2CO$ | 4.71E+13 | 253.3 |
| $CH_2OHCH_2CHO \rightarrow H_2 + 2CO + CH_4$ | 3.02E+13 | 208.2 |
| $CH_3OH \rightarrow 2H_2 + CO$ | 3.47E+14 | 305.6 |
| $CH_3CHO \rightarrow CO + CH_4$ | 6.91E+10 | 204.8 |
| $CH_3CO_2H \rightarrow 2H_2 + 2CO$ | 2.56E+11 | 228.9 |
| $C_2H_3CHO \rightarrow H_2 + CO + C_2H_2$ | 7.93E+14 | 294.5 |
| $C_2H_5OH \rightarrow H_2 + CO + CH_4$ | 1.16E+12 | 248.2 |
| $C_2H_5CHO \rightarrow 2H_2 + CO + C_2H_2$ | 1.42E+13 | 240.8 |
| $C_5H_8O_4 \rightarrow 2H_2 + 4CO + CH_4$ | 7.18E+13 | 249.2 |
| $C_6H_5OH \rightarrow 0.5H_2 + CO + 2.5C_2H_2$ | 1.08E+14 | 307.0 |
| $C_6H_5OCH_3 \rightarrow H_2 + CO + 3C_2H_2$ | 1.33E+11 | 173.7 |
| $C_6H_6O_3 \rightarrow 3CO + C_2H_2 + CH_4$ | 1.57E+11 | 190.9 |
| $C_6H_{10}O_5 \rightarrow 3H_2 + 5CO + CH_4$ | 7.11E+13 | 238.2 |
| $C_7H_8O \rightarrow H_2 + CO + 3C_2H_2$ | 1.98E+14 | 285.4 |
| $C_8H_8O_3 \rightarrow 1.5H_2 + 3CO + 2.5C_2H_2$ | 3.75E+10 | 160.9 |
| $C_{24}H_{28}O_4 \rightarrow 4H_2 + 4CO + 10\,C_2H_2$ | 4.61E+13 | 224.3 |

# Chapter 3

# Summary of results

A summary of the results and the main findings of the papers included in this thesis are presented in this chapter. The results are categorized as thermally thick particle conversion (**Paper I** and **Paper II**), potassium release (**Paper III** and **Paper IV**), and fixed bed reactor results (**Paper V** and **Paper VI**).

## 3.1 Thermally thick particle conversion

### 3.1.1 Paper I

In this paper, the pyrolysis and combustion of a single thick biomass particle are studied. A multi-region approach is used to study the physical phenomena both inside and surrounding the particle. The model is extensively validated against different experiments from the literature but only a few cases are presented here. For instance, the particle mass loss and particle centre and surface temperature ($T_c$ and $T_s$) during fast pyrolysis and combustion are presented in Fig. 3.1 and compared against experimental and numerical data from the literature [26, 77, 78]. The prediction of particle mass loss in both cases and the particle temperature in pyrolysis agree very well with the experiments. However, the temperature difference is higher in the combustion case, which can be attributed to both experimental and numerical challenges. In the experiments, the thermocouples were disconnected from the particle during char combustion because of particle deformation. On the other hand, submodels such as soot formation and radiation are not included in this work, which might affect the particle temperature during combustion. Nevertheless, the model can predict the conversion rate and the onset of different stages very well.

**(a)** Particle temperature, pyrolysis

**(b)** Particle mass loss, pyrolysis

**(c)** Particle temperature, combustion

**(d)** particle mass loss, combustion
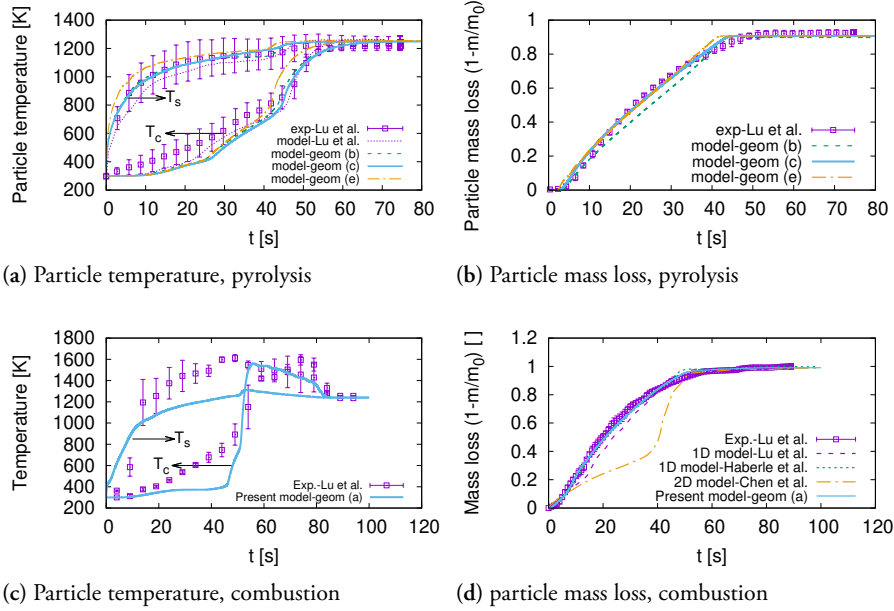
**Figure 3.1:** Model predictions of particle surface and centre temperature and particle mass loss during pyrolysis and combustion compared to experimental [26] and numerical data from literature [26, 77, 78].

The numerical model is used to study the effects of shrinkage on particle conversion. The shrinkage effects are more significant during combustion because shrinkage affects both heat transfer and mass diffusion to the particle. Two cases are simulated with and without considering the particle shrinkage and the results are compared in Fig. 3.2. Based on particle temperature in Fig. 3.2a, shrinkage makes the pyrolysis faster (end of pyrolysis marked by the sudden rise of $T_c$ around t=50 s), and the char combustion slower (end of combustion marked by a decrease in $T_c$ around t=80 s). This can be explained by the porosity, $\varepsilon$, and effective conductivity, $\kappa_{eff}$ inside the particle that is presented in Fig. 3.2b. Without shrinkage, the particle size is larger, and also the $\kappa_{eff}$ is smaller, so heat transfer to the centre of the particle is slower and pyrolysis becomes slower. On the other hand, without shrinkage, the $\varepsilon$ is higher so the oxygen diffusion inside the particle and hence the char combustion will be faster. This highlights the significant effect of particle shrinkage during biomass conversion.

(a) $T_c$ and $T_s$ during conversion

(b) Porosity and conductivity at $t = 70\ s$
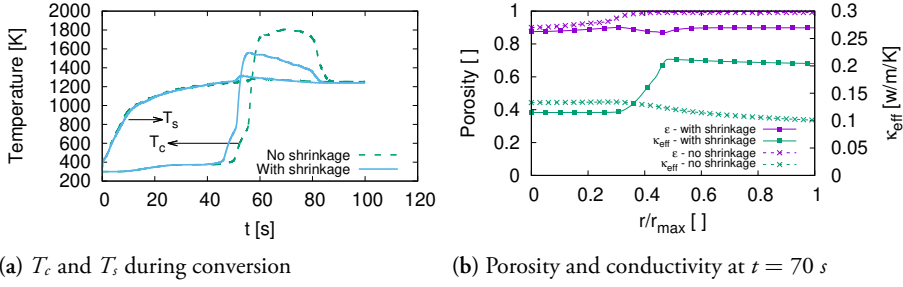
**Figure 3.2:** Effects of particle shrinkage on the particle temperature and thermophysical properties during combustion.

The effects of anisotropic heat conduction inside the woody biomass are also investigated by 3D simulations of a single cylindrical particle. The heat conductivity is higher along the fibres of the plant (axial direction) compared to the radial or tangential directions. Two cases are compared here: an isotropic case with the same conduction coefficient in all directions; and an anisotropic case with a conductivity 2.5 times higher in axial than in the radial and tangential directions. The average conductivity in three directions is the same for the two cases. The numerical results at different times are presented and compared in Fig. 3.3. In the anisotropic case, the heat transfer rate is higher from the flat sides of the cylinder compared to the curved side. But in this case, the curved side of the cylinder has a larger surface area, so the total heat transfer to the particle will be lower, hence the drying and pyrolysis rates will be lower. This can be observed by the displacement of drying and pyrolysis fronts that can be identified by water mass fraction, biomass mass fraction, or Qdot fields in Fig. 3.3.
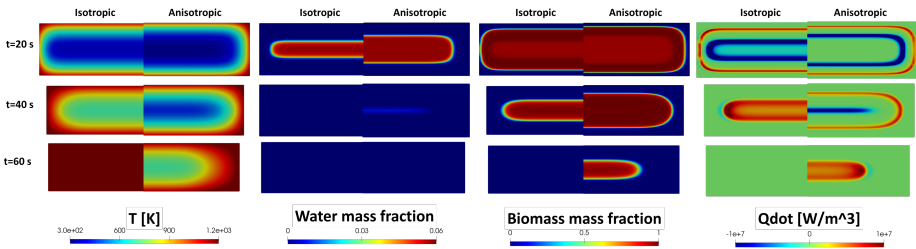


**Figure 3.3:** Effects of anisotropic heat conduction on different variables during particle pyrolysis.

In the last part of this study, coupled particle-surrounding simulations are carried out, to study the volatile combustion during thick particle pyrolysis. Particle-surrounding coupling is a stiff problem because the time scale of the fluid can be several orders of magnitude smaller than the particle timescale. Hence, the fluid can

adapt to changes at the particle surface rapidly and this leads to the idea to update the fluid field less frequently. A variable frequency scheme ($f_{var}$) is proposed that relates the fluid solution frequency to the flow rate at the particle surface. Based on this scheme, when the changes in the flow rate are high, the fluid should be solved more frequently and vice versa. This leads to a considerably lower computational cost compared to the normal scheme ($f = 1$) in which the fluid variables are updated at each iteration. The combustion of volatiles is simulated both with $f_{var}$ and the normal scheme ($f = 1$) and the results at different times are compared in Fig. 3.4. The gas temperature at a probe location 20 mm above the particle centre is presented in Fig. 3.4a which shows two distinct peaks around t=3 and 44 s. The evolution of different variables which shows the flame front is presented in Fig. 3.4b–f. As combustion starts around t=3 s, the flame front is close to the probe location, but it moves further away when the volatile release increases. The results are very similar from 20 s to 40 s, but after that toward the end of pyrolysis, the flame front moves back closer to the probe location and that is why we observe the second peak in temperature. At all times, the results obtained with the variable frequency scheme are similar to the normal scheme, while simulation time is around 4.4 times faster for the variable frequency scheme.



**(a)** T at probe location      **(b)** t=1 s      **(c)** t=3 s

**(d)** t=20 s      **(e)** t=40 s      **(f)** t=44 s
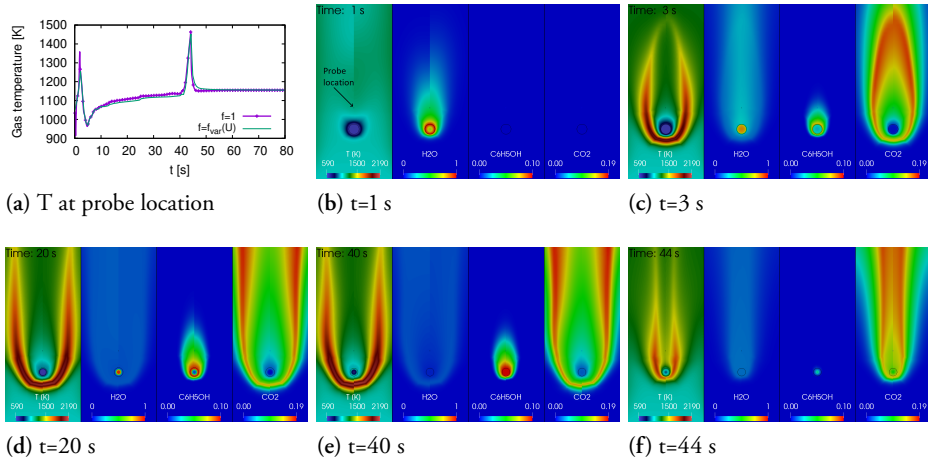
**Figure 3.4:** Numerical results with normal coupling ($f = 1$) and variable frequency coupling ($f_{var}$) for combustion of volatiles surrounding particle. Gas temperature over time at probe location (a) and T, $H_2O$, $C_6H_5OH$, and $CO_2$ concentration fields at different times (b–f). In each contour, the left half is from $f = 1$ and the right half is from variable frequency $f_{var}$ simulations.

### 3.1.2 Paper II

In this paper, the pyrolysis of lignocellulosic biomass is studied with special attention to the particle shrinkage, stages of hydrogen (H) release, and effects of wood inhomogeneities. The thick particle model developed in **Paper I** is used and the simulations are based on the recent experiments by Ossler et al. [70].

As explained in Section 2.2.4, a new anisotropic shrinkage model is proposed that is based on the experimental measurements during the pyrolysis of wood dowels. Six different cylindrical particles, p1–p6, from pine and beech wood were used in the experiments. The particle length, L, is defined along the fibre, and diameter, D, is normal to wood fibres, and the particles had an initial L/D ratio of 0.5, 1, and 2. The final L and D after slow pyrolysis (10 K/min) up to different temperatures between 300–1273 K are measured and the results are presented in Fig. 3.5. The trends for all particles are very similar and two interesting observations can be made: (1) the radial shrinkage starts at a lower temperature compared to axial shrinkage; (2) the radial shrinkage is higher than the axial shrinkage. Those observations led to the development of the anisotropic shrinkage model in Section 2.2.4, which is used in the simulations in this paper.
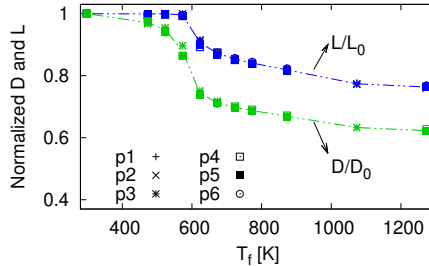


**Figure 3.5:** Effects of anisotropic heat conduction on different variables during particle pyrolysis.

Slow pyrolysis of beech wood dowels is studied. The model predictions of the mass loss, H mass loss, and particle shrinkage are compared against Ossler et al. [70] experiments and the results are presented in Fig. 3.6. The model predictions are in good agreement with the experiments at the whole range of the furnace temperature, $T_f$. Furthermore, Fig. 3.7 shows the model prediction of the elemental composition (C, H, and O mass fraction) of the residual solid at different temperatures compared to the experimental measurements in this study. Further validation of the shrinkage model is presented in the supplementary materials of **Paper II**.
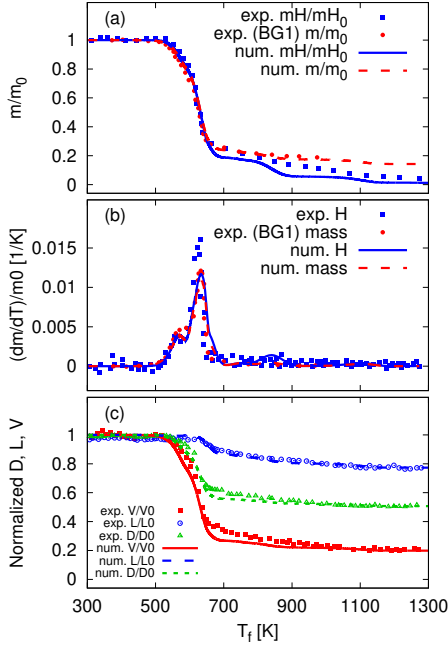
**Figure 3.6:** Comparison of the numerical and experimental [70] results. Mass and H mass (a), derivatives of mass and H mass (b), particle volume, length and diameter (c).
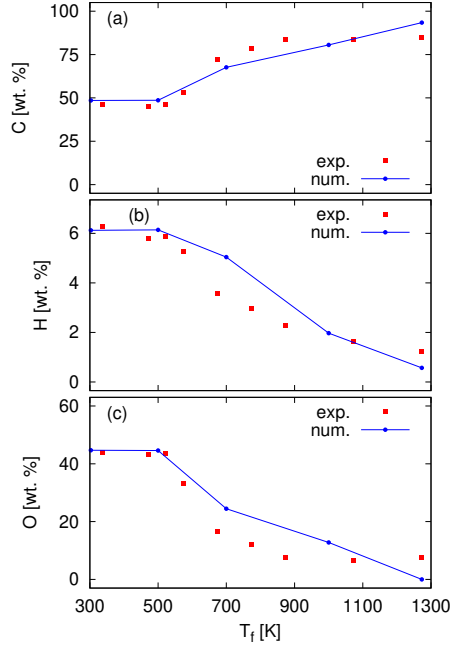
**Figure 3.7:** Elemental composition of the residual solid after pyrolysis at different temperatures, compared to experimental measurements presented in **Paper II**.

Biomass pyrolysis from 300 to 1300 K is divided into four stages as presented in Fig. 3.8. Stage (I) is from room temperature up to 500 K, during which the pyrolysis is slow and mass and H mass loss are negligible. Stage (II), 500-700 K, is the main stage of pyrolysis where around 80% of mass and total H is released. Two peaks can be observed in the H release rate in this stage which is attributed to the HCE and CEL decomposition, respectively (Fig. 3.8b). In stages (III) and (IV), the mass loss is very small but the H mass loss is still considerable. The main difference between these two stages is the mixture that is released into the gas phase as presented in Fig. 3.9. In stage (IV), the mixture is mainly made of $H_2$, CO, and $H_2O$. The water can be easily separated by condensation and the final syngas (CO+$H_2$) has many applications in different combustion devices.
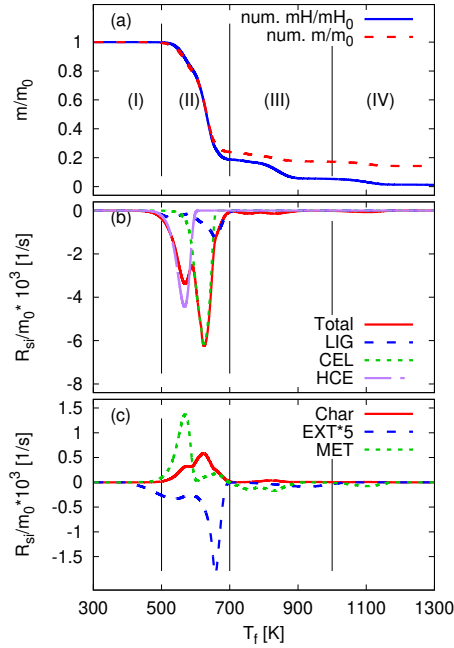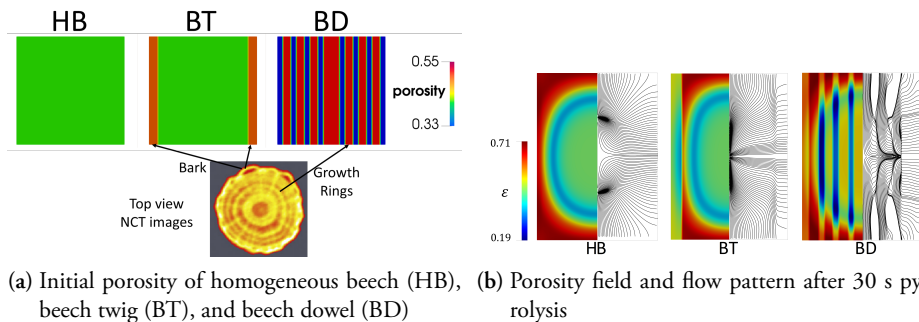
**Figure 3.8:** Different stages of pyrolysis and H release from the biomass particle.
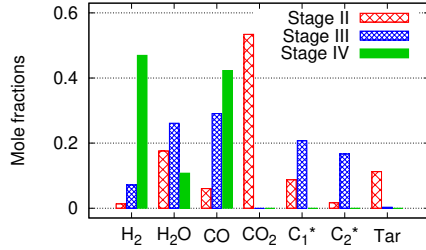


**Figure 3.9:** Major gas-phase products from primary pyrolysis at different temperatures.

The model is used to study the pyrolysis of inhomogeneous wood, such as forestry residues, which have inhomogeneous properties because of the growth rings and also bark. Three cases are considered, i.e., homogeneous beech (HB), beech twig (BT) which has bark, and beech dowel (BD) which has growth rings. The initial porosity of the three cases, in the 2D axisymmetric numerical domain, is presented in Fig. 3.10a. Also, a Neutron Computed Tomography (NCT) image of pyrolyzed wood is presented in the same figure for comparison. Based on simulations, it was found that HB and BD have a very similar pyrolysis duration, but BT pyrolysis is faster because of the lower bark density. On the other hand, the porosity field and the flow pattern inside the particle, which are presented in Fig. 3.10b, are considerably different in the three cases. The bark can disturb the flow of volatiles inside the particles toward the axial direction. Moreover, in the BD the flow rate is higher in the rings with lower density compared to higher density. The flow pattern is especially important for char combustion which is limited by mass transfer to the particle.

(**a**) Initial porosity of homogeneous beech (HB), beech twig (BT), and beech dowel (BD)

(**b**) Porosity field and flow pattern after 30 s pyrolysis

**Figure 3.10:** Effects of wood inhomogeneities such as bark and growth rings on the flow pattern inside the particle during fast pyrolysis.

## 3.2 Potassium release

### 3.2.1 Paper III

The K-release model that is proposed in this paper (Table 2.3) can predict different aspects of K-Cl-S release during and after the combustion and pyrolysis of biomass particles. The initial composition of the fuel and ash-forming elements are among the most important parameters that are included in the model. First, different types of K left in solid residue after pyrolysis and combustion at different temperatures are studied. The numerical simulations are carried out for the conversion of wheat straw (WS) based on Huang et al. [22] experiments and a comparison of the numerical and experimental results are presented in Fig. 3.11. Three different types of potassium are available in biomass, i.e., inorganic ($H_2O$-soluble), organic ($NH_4AC$-soluble), and stable (acid or non-soluble) [22]. Only a small fraction of K is released after pyrolysis at 673 K which is attributed to the release of atomic K from organic R-COOK (R6). At this temperature, also a part of inorganic KCl is converted to organic R-COOK through R4, which explains the peak of organic K at this temperature. Higher temperature favours the release of atomic K (R6) over char-K formation (R5). Therefore, by increasing T (for T>673 K) the amount of organic K in solid decreases. Two sudden changes are observed in the inorganic K curve, around 900 and 1100 K, which are attributed to KCl and $K_2CO_3$ evaporation. During pyrolysis, the amount of stable K remains almost constant.

Similar to pyrolysis, different types of potassium after the combustion of WS are presented in Fig. 3.11b. The total K release is higher after combustion compared to pyrolysis, which can be explained by the release of char-K (R12) and also a slightly higher particle temperature. During combustion, the fraction of stable K can increase due to the reaction of potassium with the aluminosilicate matrix (R13). This last

reaction is only expected in fuels with high Si content (Si-rich fuels).



(a) Pyrolysis in $N_2$ atmosphere.

(b) Combustion in $N_2$-$O_2$ atmosphere.
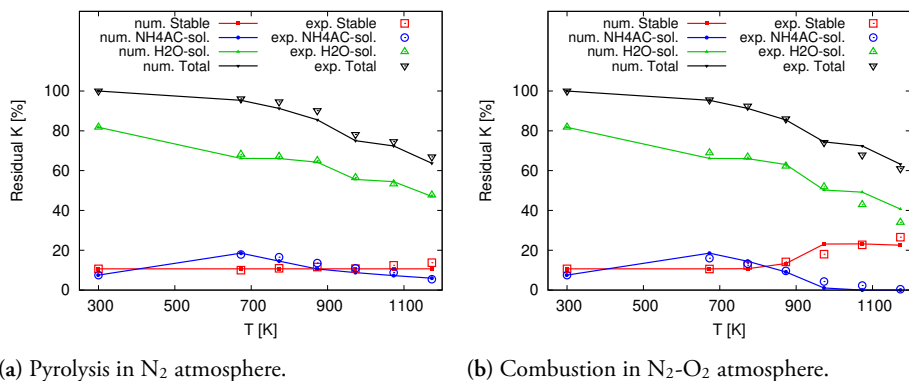
**Figure 3.11:** Types of residual K in solid particles after conversion in $N_2$ (a) and $N_2$-$O_2$ (b) atmospheres at different temperatures. Experimental data from Huang et al. [22].

The release of K, Cl, and S elements from two different types of biomass is studied by the model and the results are compared to experiments [21] in Fig. 3.12. The two fuels are wheat straw (WS) and carinata (CA) which are rich and lean in Si, respectively Fig. 3.12. It was observed that the release of ash-forming elements is considerably different in Si-rich compared to lean fuels. Fig. 3.12a shows the normalized mass of K-Cl-S after the combustion of WS at different temperatures. In this case, Cl is released in two steps which are related to HCl (R4) and KCl (R7) release, respectively. The organic S was released at a relatively low temperature (<673 K), while the inorganic S from $K_2SO_4$ was released later. The release of inorganic S in Si-rich fuels is enhanced due to the reaction of $K_2SO_4$ with aluminosilicates (R13) which leads to the trapping of K and release of $SO_2$ t. A small amount of K was released before 673 K that is attributed to organic K. Release of K is related to KCl evaporation up to 1100 K, and evaporation/dissociation of $K_2CO_3$ at higher temperatures. The release of K-Cl-S from Si-lean CA is presented in Fig. 3.12b. The major difference between WS and CA is the fact that R13 is not active for the latter. Hence, a part of K and S can remain stable in form of $K_2SO_4$ until very high temperatures.

(a) Wheat straw (WS)　　　　(b) Carinata (CA)
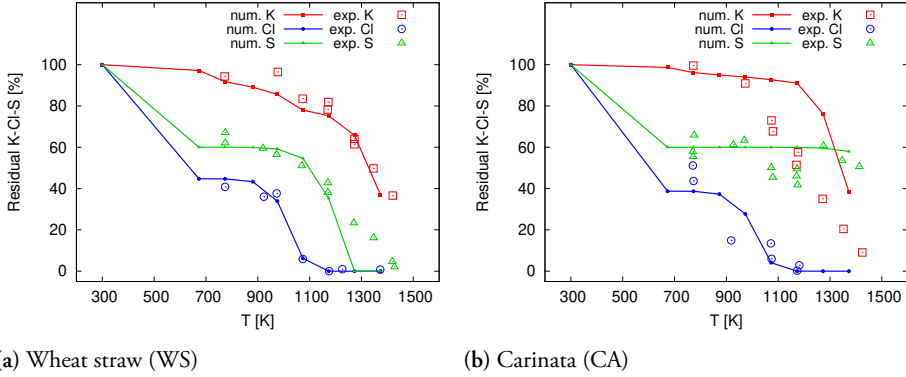
**Figure 3.12:** Residual K, Cl, and S in solid after combustion of WS (a) and CA (b) at different temperatures. Experimental data from Knudsen et al. [21].

The model was also used to study the release of gas-phase potassium species and the model predictions are compared against experimental measurements [79] in Fig. 3.13. The concentration of K-species was measured downstream of the sample during the combustion of spruce bark (SB) at different temperatures (only two are presented here). At T=1123 K (Fig. 3.13a), the concentration of atomic K is high during the pyrolysis stage ($t \leq 3$ s) which is attributed to the release of organic K (R6). During the combustion stage (3 to 25 s), the sample temperature is high enough for KCl evaporation. The KCl evaporation continues even after char combustion (during ash cooking) but at a lower rate. At this temperature, the concentration of KOH and atomic K are low during the char combustion and ash-cooking stages, which is predicted by the model. Similar trends are observed at T=1223 K (Fig. 3.13b), but the concentration of KOH is higher in this case because the dissociation of $K_2CO_3$ or $K_2SO_4$ becomes more important at higher temperatures.

**(a)** 1123 K        **(b)** 1223 K
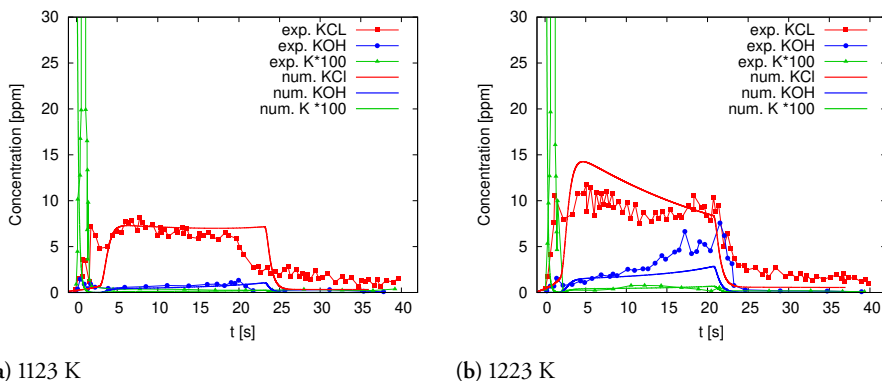
**Figure 3.13:** The concentration of gas-phase K-species downstream of the sample during combustion at different temperatures. Experimental data from Sorvajarvi et al. [79].

Based on the model that was proposed in this study, the main pathways for the transformation and release of K-Cl-S can be identified in the schematic presented in Fig. 3.14. The elements that are initially in organic, inorganic, or stable form follow different routes depending on the ash composition, temperature, and type of conversion (pyrolysis or combustion/gasification). This schematic presents a summary of what was discussed above, the main reactions that are active at different conversion stages, and the main species that are expected to be in solid particles or released to the gas phase at various temperatures.
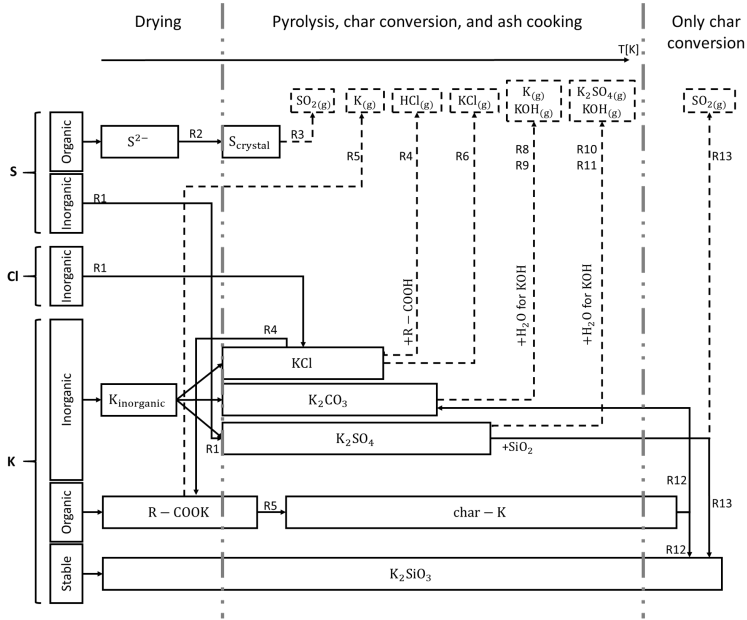
**Figure 3.14:** The main pathways for the transformation and release of K-Cl-S species. The schematic is based on the reactions in the proposed K-release model (Table .2.3).

### 3.2.2 Paper IV

In this paper, an Eulerian-Lagrangian approach is used to study the gasification of biomass particles in a 140 kW EFG. The model predictions are validated against TD-LAS measurements of temperature and $H_2O$ concentration at two different ports [80], which are presented in Fig. 3.15a. Furthermore, Fig. 3.15b shows the comparison between model and experimental measurements of mole fraction of the major gas species at the reactor outlet. The model predictions both inside EFG and at the outlet are in good agreement with the experimental measurements.

(a) Average T and H$_2$O distribution

(b) Major products at outlet
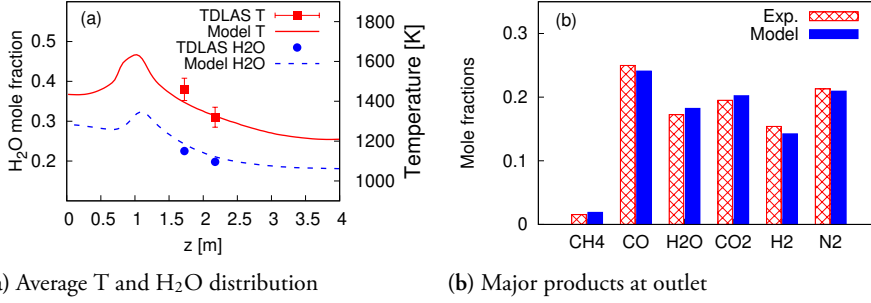
**Figure 3.15:** Comparison of the model predictions and the experimental measurements Sepman et al. [80].

The model is used to study the main phenomena that occur in different zones inside the reactor as presented in Fig. 3.16. Zone I is the drying zone, in which the liquid water evaporates from the particles and the particles undergo pyrolysis in zone II. Zone III is the combustion zone which provides the energy (heat) for the operation of the gasifier and the particles and gas are at their maximum temperature. The flame is stabilized by the recirculation zone IV, which is formed around the centre of the reactor. The gasification of char in zone V is the main active process in a large part of EFG downstream of the combustion zone. In this zone, the unburned char in the solid particles reacts with H$_2$O and CO$_2$ to produce H$_2$ and CO. The particles at the centre of the reactor have a higher momentum and a lower residence time (Fig. 3.16h), which leads to a lower carbon conversion at the same height (Fig. 3.16g). The distribution of the reactants (H$_2$O and CO$_2$) and products (H$_2$ and CO) of char gasification are presented in Fig. 3.16i–l.

45
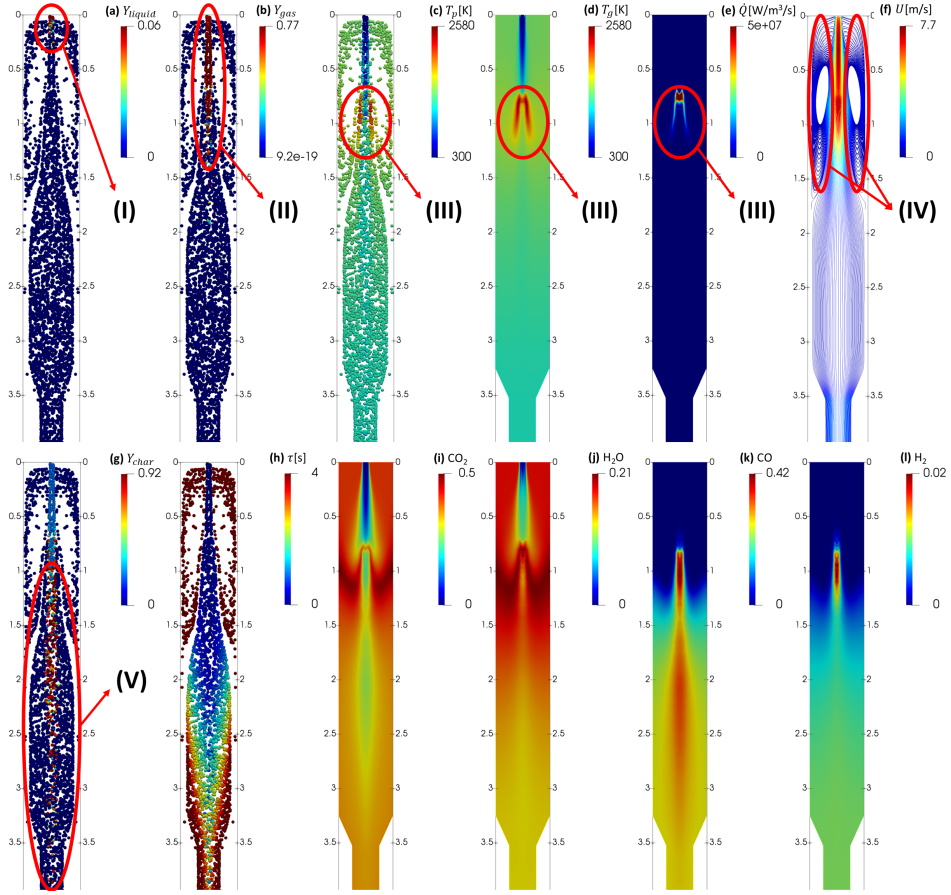
**Figure 3.16:** Numerical predictions of different fields related to fluid and solid particles. The regions marked in the figure are (I) drying, (II) pyrolysis, (III) combustion, (IV) recirculation, and (V) gasification zones.

The potassium release model from **Paper III** is integrated into the CFD model in this work to predict the distribution of gas-phase K-species inside the EFG. The model predictions and the PF-TDLAS measurements at port 2 [71] are compared in Fig. 3.17. At the operating conditions of the EFG, the major fraction of K is in KOH form, and the fraction of KCl and atomic K are considerably lower, which is predicted very well by the model.
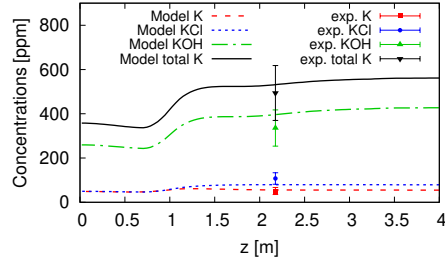
**Figure 3.17:** The concentration of gas-phase K-species and comparison to experimental measurements at port 1 [71].

Finally, the model is used to study the distribution of the gas-phase K-species and the residual K, Cl, and S elements inside the fuel particles, which is presented in Fig. 3.18. The distribution of different species can be explained by the reactions in the K-release model (Table 2.3). The atomic K (Fig. 3.18a) is released at the lowest temperature which is attributed to the release of organic K (R6). The KCl evaporation (R7) starts at a higher temperature and almost all of the KCl and solid Cl content is released around the combustion zone (Fig. 3.18b and d). The dissociation of $K_2CO_3$ and $K_2SO_4$ (R9 and R11) starts at a very high temperature in the combustion zone, which leads to the formation of KOH (Fig. 3.18c). The KOH release continues in the gasification zone because the temperature and $H_2O$ concentration are still high, and K and S are still left in the solid in form of $K_2SO_4$ (Fig. 3.18e and f).
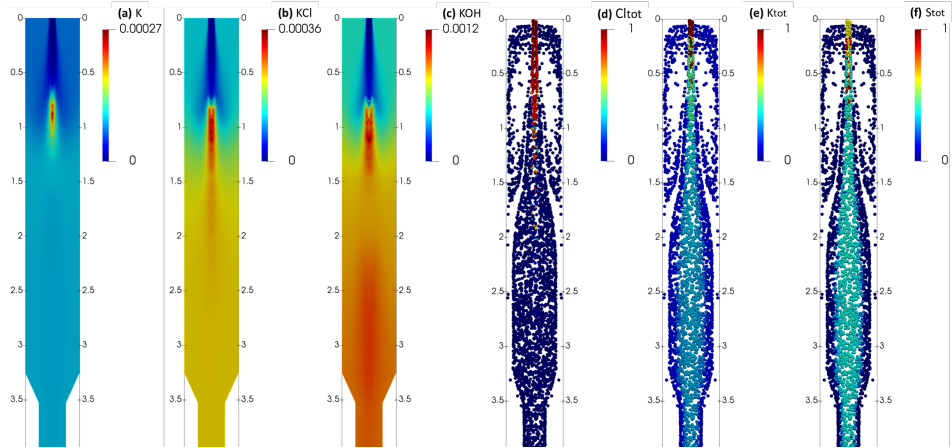


**Figure 3.18:** Distribution of gas-phase atomic K (a), KCl (b), and KOH (c). Normalized mass of residual Cl (d), K (e), and S (f) in solid particles.

## 3.3 Fixed bed reactor and freeboard

### 3.3.1 Paper V

In this study, the gas-phase reactions in the freeboard of a fixed bed reactor and NO emission and reduction are investigated. The reactor is a lab-scale 8–11 kW reactor that was investigated in earlier studies [81, 82]. 3D simulations of the freeboard are carried out without including the fixed bed in the model. The products of biomass conversion in the bed are estimated by single particle studies and the mass, element, and energy balance in the bed.

The model prediction for temperature and major species at 8 and 11 kW operating conditions are validated against the experiments. Figure 3.19a and b show the temperature and $O_2$ mole fraction over the centre axis of the reactor. $CO_2$ and CO mole fractions are also validated against the experiments, but the results are not repeated here. Finally, the NO concentration which is one of the main topics of this study is presented in Figure 3.19c and compared with experiments. Based on the model, more than 70% of total NO emission is originated from the fuel-N whereas the rest is coming from the atmospheric $N_2$.



(a) Temperature    (b) $O_2$ mole fraction    (c) NO concentration (8 kW)
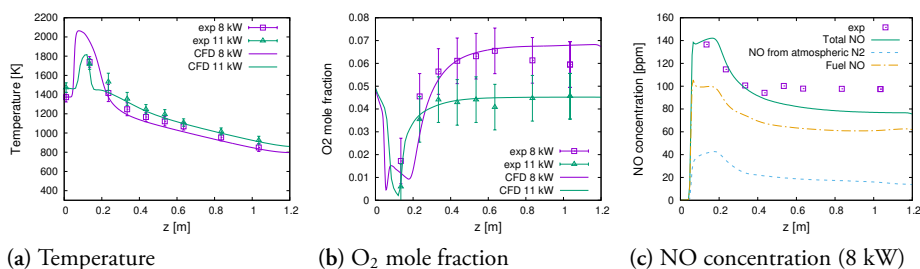
**Figure 3.19:** Comparison of the model predictions over the centre vertical axis of reactor against the experimental measurements by Wiinikka et al. [82].

The application of selective non-catalytic reduction (SNCR) on NO emissions is studied in the present work. In SNCR, $NH_3$ is injected at a specific height and temperature range to reduce the NO emissions. SNCR performance is very sensitive to the injection height because injection at very high temperatures can lead to a further increase in NO emissions, while injection at very low temperatures is ineffective because the reduction becomes too slow. In this study, $NH_3$ was injected at seven different heights from z=0.2 to 0.8 m. The NO concentrations for different cases are presented in Fig. 3.20a and compared against the original case with no SNCR. Furthermore, the NO reduction by injection at different heights is presented

in Fig. 3.20b. It was found that in this specific reactor, maximum NO reduction can be obtained by injection at z=0.4 m.

The next parameter that is effective on the performance of SNCR is the Nitrogen Stoichiometric Ratio (NSR), which is defined as the molar ratio of injected $NH_3$ to NO at the outlet of the original case [18]. Simulations with different NSRs in the range of 0.5 to 7 are carried out and the ammonia utilization efficiency, $\eta_{NH_3}$, and NO reduction as a function of NSR are presented in Fig. 3.20. The $\eta_{NH_3}$ is defined as

$$\eta_{NH_3} = \frac{NO_{initial} - NO_{final}}{NO_{initial} \times NSR} \times 100 \, , \tag{3.1}$$

where $NO_{initial}$ and $NO_{final}$ are the NO concentration at the outlet before and after applying SNCR. It was observed that by increasing NSR, the NO reduction continuously increases, but $\eta_{NH_3}$ increases and then decreases. Operating at NSR=1.5 seems like an appropriate choice, as it has a relatively high NO reduction and $\eta_{NH_3}$. NSR higher than 1.5 does not lead to significant NO reduction but significantly reduces the ammonia utilization efficiency.



(a) Injection height effect on NO distribution (b) Injection height effect on NO reduction (c) NSR effect
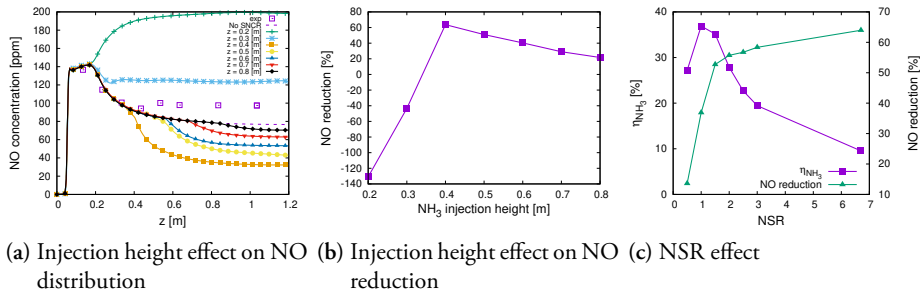
**Figure 3.20:** Performance of SNCR method for NO reduction.

The NO formation and reduction and the most important reactions that are active in different parts of the reactor are studied by the model. The NO formation rate with and without SNCR are presented in Fig. 3.21a. Two distinct peaks for NO formation can be observed which can be explained by $O_2$ and T distributions at the bottom of the reactor (Fig. 3.21b). The first peak is around z=0.1 m, where the combustion started, so the temperature is very high, and $O_2$ is still available. Slightly higher, the $O_2$ concentration is very low, so the NO formation rate is very low. Further downstream close to z=0.22 m, the temperature is still relatively high and the $O_2$ concentration is also high because of the introduction of the tertiary air, which leads to the second peak in NO formation. In the SNCR case, the NO decreases downstream of z=0.4 m, because of the ammonia injection at that height. Based on the model, the

top 10 active reactions which had the highest impact on NO formation and reduction in each case were selected and their summation is presented in Fig. 3.21a. It can be observed that the selected 10 reactions are the main reactions affecting NO formation. A schematic of the fate of fuel-N is presented in Fig. 3.21c, which is based on the 10 selected reactions in this study.
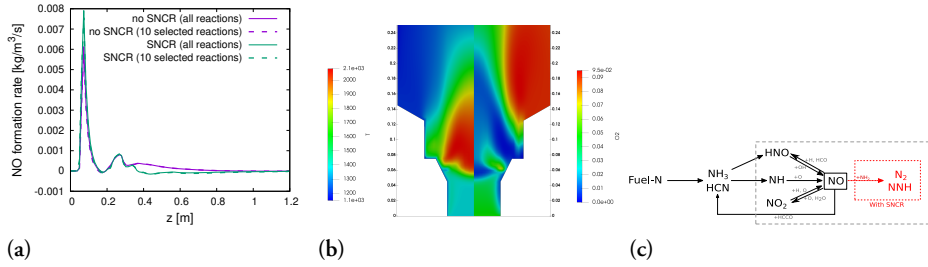


**Figure 3.21:** Performance of SNCR method for NO reduction.

## 3.3.2   Paper VI

In this paper, the tabulation method is used to model the combustion of thermally thick particles in a fixed-bed reactor. To evaluate the performance of the tabulation method, two cases with single and three stacked particles as displayed in Fig. 3.22 are considered. In each case, the pyrolysis of particles in an inert atmosphere is first modelled using the detailed method. Then, the heat transfer to the particle is calculated at each time and the tabulation method is used to estimate the particle conversion rate.
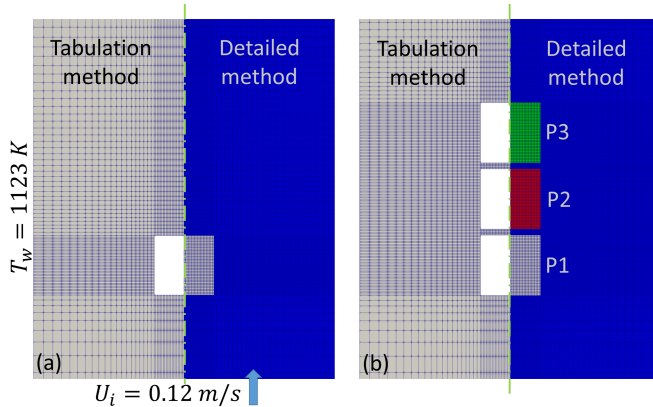


**Figure 3.22:** The geometry and mesh surrounding the particles for the comparison of the tabulation method and the detailed model. (a) One-particle case and (b) three-particles case.

The particle surface temperature for the two cases predicted by the tabulation

method is compared to the detailed particle model in Fig. 3.23a and b. In the single particle case, the radiation from the walls to the particle is dominant so $T_{eff}$ is almost uniform and the tabulation method can accurately predict the surface temperature. However, in the three particles case, the particle-particle interactions also play an important role. In this case, the middle particle (P2), is partially blocked by the neighbour particles P1 and P3. Therefore, as presented in the Fig. 3.23c, it absorbs less radiative heat from the walls, and it has the lowest temperature. Moreover, the P1 at the bottom is closest to the cold inlet and is being cooled by convection, so it has the second lowest temperature. The tabulation method can predict the same trend for the temperature of the particles. However, the temperature at the surface of the particles is not uniform and $T_{eff}$ changes over time, which leads to some errors in the tabulation method. This small error is reasonable, especially considering the significant speed-up obtained by using the tabulation method.
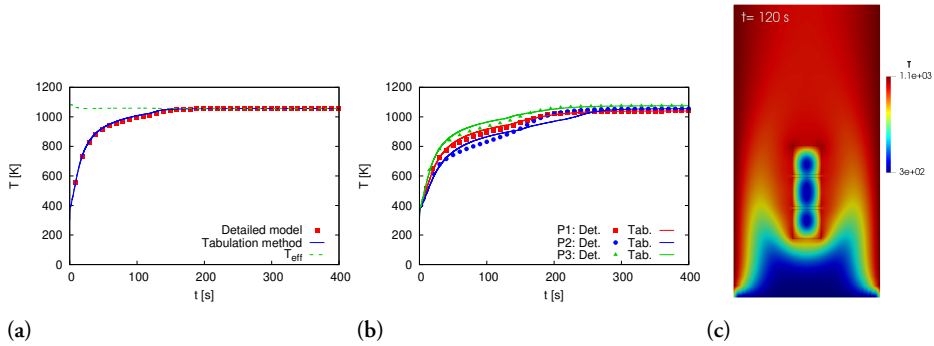


**Figure 3.23:** Particle surface temperature in (a) one-particle case and (b) three-particles case. (c) Temperature inside and around the particles predicted by the detailed model at t=120 s.

The tabulation method is used to simulate the biomass combustion based on Shin et al. [31] experiments. In the experiments, cubic particles with a size of 20 mm are placed in a batch reactor with heaters set at 1123 K. Air is flowing with a velocity of 0.12 m/s from the bottom of the reactor. The combustion starts at the top of the reactor and propagates toward the bottom. The flame propagation speed was measured by placing eight thermocouples, G2–G9, inside the bed. The measured temperatures are presented in Fig. 3.24a and the results of the 1D model of Shin et al. [31] are presented in Fig. 3.24b. The temperature profiles predicted using the present bed model, which are shown in Fig. 3.24c, are comparable with the experimental and numerical results of Shin et al. [31]. Furthermore, the flame propagation speed predicted by the present model is 0.83 cm/min, which is equal to that obtained through measurements.
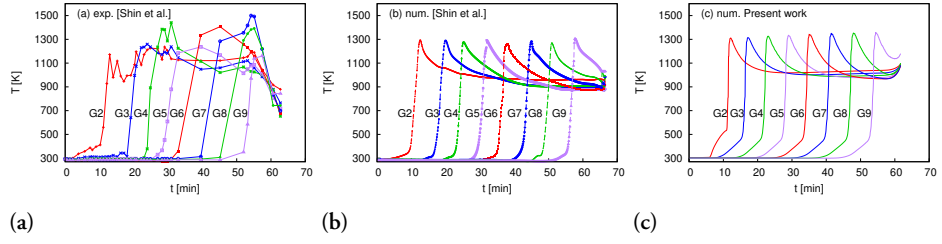
**Figure 3.24:** Temperature history at the location of thermocouples G2–G9 in the bed. (a) Experimental measurements [31], (b) 1D numerical results [31], and (c) numerical results of the present study.

# Chapter 4

# Conclusions and outlook

## 4.1   Main conclusions of the papers

The first part of the results (**Paper I** and **Paper II**) in this thesis was related to biomass conversion at the particle scale. A detailed multi-region model was developed for the conversion of thick biomass particles and validated against various experimental data related to particle temperature, mass loss, hydrogen release and char composition, shrinkage, and gas-phase products from biomass pyrolysis and combustion. Anisotropic shrinkage of different wood samples during slow pyrolysis was measured experimentally and a new anisotropic shrinkage model was developed that correlates the particle shrinkage in different directions to the decomposition of cellulose, hemicellulose and lignin. Simulations of thermally thick particles during pyrolysis and combustion were carried out to investigate the effects of anisotropic heat conduction, effects of particle shrinkage, volatile combustion surrounding the particle, stages of hydrogen release during pyrolysis, effects of heating rate, and effects of inhomogeneities such as bark and growth rings in the wood. The simulations at the particle scale led to several conclusions which can be summarized as follows: (1) Particle shrinkage increases the heat conduction and reduces the mass transfer inside the particle, hence it leads to faster pyrolysis and a slower char conversion. (2) Based on experiments on particles from different sources of wood with different initial dimensions, it was found that the radial shrinkage (normal to the grain) is higher and starts at a lower temperature than the axial shrinkage (along the grain). The proposed model, in which the radial shrinkage is mainly attributed to cellulose and hemicellulose decomposition and axial shrinkage is related to the lignin decomposition, could predict the anisotropic shrinkage of the wood very well. (3) The anisotropic heat conduction in the solid plays an important role in the pyrolysis stage. Using the average value of

heat conduction with an isotropic heat transfer model does not necessarily produce the same results. (4) Simultaneous modelling of a thick particle and surrounding fluid is a stiff problem because the timescale of the particle is orders of magnitude greater than the fluid. A solution to this stiff problem is to solve the fluid region less frequently when the changes at the particle boundary are small. (5) The hydrogen content of biomass is released in four stages during pyrolysis. Stage I (300-500 K) is the heat-up stage and stage II (500-700 K) is the main stage where around 80% of total mass and H mass are released. In stage III (700-1000 K) and stage IV (1000-1300 K), the mass release is small but the H release is still considerable. The main difference between the two stages is the fact that products of stage IV are mainly CO, $H_2$, and $H_2O$, which are easier to work with. (6) It was shown that a higher heating rate during pyrolysis can modify the temperature distribution inside the particle and shift the H release toward higher furnace temperatures. (7) Wood bark has a different density compared to wood which leads to a different pyrolysis time. Both wood bark and growth rings of wood affect the flow pattern inside the particle, which influences the internal mass transfer and char conversion.

In the second part of the thesis (**Paper III** and **Paper IV**), the potassium release from biomass was studied. A multi-step predictive model was proposed with 12 species and 13 reactions, that includes the main pathways for the transformation and release of K, Cl, and S-containing species from solid biomass. The effects of the elemental composition of the fuel, the origin of the elements (organic/inorganic), and the conversion atmosphere are also considered in the model. The model was used to study the organic, inorganic, and stable K that is left in solid residue after pyrolysis and combustion at different temperatures and the results are compared with experimental data from the literature. The residual K-Cl-S in two types of biomass (rich and lean in Si) after combustion were studied next and compared with experiments. Finally, the production of gas-phase K-containing species during the combustion of biomass at three different temperatures was simulated and compared against experiments. The validated model was used to investigate the K-release in a 140 kW atmospheric EFG. The EFG model was validated using tunable diode laser absorption spectroscopy (TD-LAS) measurements of $H_2O$ and temperature at two ports along the reactor, and also the mole fraction of major species at the outlet. The following can be concluded from the main findings of the two papers on potassium release: (1) The K-release model can predict the main solid and gas phase potassium-containing species during and after conversion at different temperatures. (2) Total K-release is higher after combustion compared to pyrolysis, which can be attributed to higher particle temperature or the release of char-K. (3) Release of atomic K starts at lower temperatures (early pyrolysis) due to the decomposition of the organic matrix. KCl evaporation starts at high temperatures during combustion and its evaporation continues at a lower rate during the ash cooking stage. KOH is mainly formed through the dissociation of inorganic

$K_2CO_3$ and $K_2SO_4$ with water at very high temperatures. (4) Based on the model, five different zones can be identified in the EFG, i.e., drying, pyrolysis, combustion, recirculation, and gasification zones. (5) Based on various experiments from literature, the gasification with $H_2O$ can be slower or faster than with $CO_2$. Nevertheless, the water-gas shift reaction is very fast in the gasifier conditions in the present study, so this reaction determines the balance between the gasification products. (6) Release of atomic K, KOH, and KCl in a gasifier can be predicted by the K-release model, and it was shown that the model has low sensitivity to the model parameters such as the ratio of organic/inorganic elements in the raw biomass.

In the last part of the thesis (**Paper V** and **Paper VI**), the combustion of biomass in fixed-bed reactors was investigated. In **Paper V**, the focus was on the freeboard, so the composition of the gas-phase products from the bed was estimated by using the results from single particle modelling and some simple assumptions to preserve the elemental and energy balance in the bed. Two reaction mechanisms (Lovas and Goyal) were combined to include the decomposition of complex tar species as well as combustion and NO chemistry in the model. The gas-phase reactions and NO formation in the freeboard were studied using the new mechanism and the performance of selective non-catalytic reduction (SNCR) for this specific boiler was analysed. In **Paper VI**, the focus was on developing a computationally efficient numerical model for the bed which can be coupled to CFD solvers. The tabulation method was proposed for the drying and pyrolysis stages, and three main controlling variables are defined to generate the tables. The tabulation method was compared with the detailed particle model for two different cases with one and three stacked particles. Finally, the bed model was used for 2D simultaneous simulation of the bed and freeboard in a batch reactor. The temperature profiles and the flame propagation speed in the bed had a good agreement with the experiments. The results from the study of biomass combustion in fixed bed reactors have led to the following conclusions: (1) Using the detailed tar composition and reaction mechanism that was proposed in this study, the utilization of global reactions for combustion of hydrocarbons is avoided, which leads to a more accurate temperature and hence NO prediction. (2) Fuel-N is the main source of NO emission and its contribution to total NO is three times higher than the atmospheric $N_2$. (3) SNCR can be applied by $NH_3$ injection at a specific height downstream of the bed to reduce the NO emissions, and up to around 60% NO reduction was obtained by proper utilization of this method. (4) Using the tabulation method leads to a significant speed-up compared to the detailed particle model, and it leads to results with acceptable accuracy. (5) The tabulation method is not sensitive to the grid size, and it allows using detailed chemistry or performing 2D/3D simulations, which are important for some studies such as bed channelling.

## 4.2   Future outlook

In this thesis, models have been developed for the study of biomass conversion and potassium release at the particle and reactor scales. Some research gaps in the literature were identified and addressed in each part of the thesis. There are still several questions that can be investigated in future works to better understand the topics presented in this thesis. Some suggestions for future work are:

- More advanced measurements and models are still required to study the char conversion stage at the particle scale. More reliable experimental data is required regarding the particle temperature, the evolution of structure and surface area of char during conversion, the diffusion rate of gas-phase reactant to and through the char, and also intrinsic kinetic rates of char conversion. Some measurements have been done in earlier studies but the level of uncertainties is very high. New measurements can be used to develop more accurate and predictive models for char conversion.

- Shrinkage of different wood particles during pyrolysis was studied, but more information is required regarding the drying and char conversion stages.

- A kinetic model was proposed for the release of potassium species from biomass, in which the rate constants were estimated based on experimental observations from the literature. A more accurate model requires experimental measurement of kinetic rates at different temperatures and $H_2O$ concentrations, especially for important reactions such as evaporation or dissociation of inorganic salts.

- Detailed and skeletal mechanisms are available for modelling combustion in freeboard, but global reactions are commonly used for the simulations of gasifiers. A detailed kinetic model has to be developed specifically for the gasifier environment, which can be used for better prediction of temperature, species, and radicals distribution inside the reactor. This also helps with the modelling of the gas-phase nitrogen and potassium reactions, which requires the concentration of the radicals.

- In entrained flow and fluidized bed reactors, because of the large number of discrete particles, a simple thin particle model with very basic submodels for drying, pyrolysis, and char combustion was used in the present work and most other recent studies. More detailed particle models can be developed in future works to improve the reactor scale simulations. Pre-processing of the particle conversion at different conditions, such as what was used for the fixed bed simulations in this thesis, is another option that can be used for entrained flow or fluidized bed reactor simulations.

- Experimental measurement of species and temperature at several points inside each zone of gasifiers are required to study the main processes in each zone. This data will be also valuable for model validation, because in most numerical studies, only the products at gasifier outlet are compared against the experiments.

- Measurements of the SNCR application in a biomass reactor are scarce. More measurements are needed to measure the actual effectiveness of this method and also to validate the model predictions.

- More progress variables can be included in the bed model to improve the accuracy of the tabulation method. When the number of variables is high, a machine learning algorithm such as an artificial neural network can replace the tables to extract the conversion rate of the particles. The tables or the neural network can also be used in Eulerian-Lagrangian simulations for a more accurate description of the solid particles.

# Appendix A

# Derivations (Appendix)

## A.1 Energy Equation

The derivation of the energy conservation equation for continuous fluid and also for thick biomass particles is presented in this section. The energy equation is derived following Bai's lecture notes [83], based on the first law of thermodynamics in an open control volume (CV). According to the first law, the total energy per unit mass, $e_{tot}$, in a CV is changed due to the energy transfer at boundaries, heat transfer from radiation, and heat generation due to viscosity. The total energy per unit mass is equal to $e_{tot} = h - p/\rho + U^2/2$ where $h$, $p$, $\rho$, and $U$ are the enthalpy, static pressure, density, and velocity vector in the control volume. The conservation of energy based on the first law can be expressed in the form of

$$\frac{\partial}{\partial t}(\rho e_{tot}) + \nabla \cdot \vec{q}_{tot} = \dot{Q}_{rad} + \dot{Q}_{vis} \,, \tag{A.1}$$

where $\vec{q}_{tot}$ is the total heat flux vector. $\dot{Q}_{rad}$ and $\dot{Q}_{vis}$ are heat sources in the CV due to radiation and viscosity, respectively.

The total energy flux over an open CV boundary is the sum of the heat transfer due to gas and species transfer through boundaries, temperature gradient at the boundary, and heat transfer due to concentration gradient at the boundary (Dufour effect) which is small in most cases other than binary gas mixtures and is neglected here. The remaining terms in the total energy flux can be expressed as

$$\vec{q}_{tot} = \left[\rho U(h - \frac{p}{\rho} + \frac{1}{2}U^2)\right] + [-\kappa\nabla T] + \left[\rho \sum(Y_i U_i h_i)\right] \,, \tag{A.2}$$

where the three terms on the right-hand side are the energy flux due to convective flow, heat conduction, and species diffusion, respectively. By defining $K_e = U^2/2$, placing every term in Eq. A.1, and reordering the energy equation we obtain

$$\frac{\partial}{\partial t}\left[\rho(h - \frac{p}{\rho} + K_e)\right] + \nabla \cdot (\rho U h) + \nabla \cdot (\rho U K_e) - \nabla \cdot (Up) =$$
$$\nabla \cdot \left[\kappa \nabla T - \rho \sum (Y_i U_i h_i)\right] + \dot{Q}_{rad} + \dot{Q}_{vis} \,. \tag{A.3}$$

The objective is to derive the energy equation in terms of $h$ for the fluid region but the diffusion term is a function of $T$. Based on the definition of enthalpy of a mixture we can write

$$\nabla h = \nabla \sum (Y_i h_i) = \sum (Y_i \nabla h_i) + \sum (h_i \nabla Y_i) \,. \tag{A.4}$$

Enthalpy of species can be calculated by $h_i = h_i^0 + \int_{T_{ref}}^{T} c_{pi} dT$, therefore $\nabla h_i = c_{pi} \nabla T$. Placing in Eq. A.4 yields

$$\nabla h = \sum (h_i \nabla Y_i) + \sum (Y_i c_{pi} \nabla T) = \sum (h_i \nabla Y_i) + c_p \nabla T. \tag{A.5}$$

Reordering the last equation and multiplying both sides to $\kappa$ we can write

$$\kappa \nabla T = \frac{\kappa}{c_p}\left[\nabla h - \sum (h_i \nabla Y_i)\right] \,. \tag{A.6}$$

Based on the above equation and Fick's law, we can rewrite the diffusion term of the Eq. A.3 so that

$$\kappa \nabla T - \rho \sum (Y_i U_i h_i) = \rho \alpha \nabla h - \rho \alpha \sum (h_i \nabla Y_i) + \rho \sum (D_i h_i \nabla Y_i)$$
$$= \rho \alpha \nabla h - \rho \alpha \sum \left[(1 - \frac{D_i}{\alpha}) h_i \nabla Y_i\right] \,. \tag{A.7}$$

Assuming unity Lewis number, $Le_i = \alpha/D_i = 1$, the last term on the right-hand side of the above equation will be zero, which simplifies the diffusion term to $\rho \alpha \nabla h$. Substitution in the Eq. A.3 and neglecting the heat generation due to viscosity yields

$$\frac{\partial}{\partial t}(\rho h) + \nabla \cdot (\rho U h) - \frac{\partial p}{\partial t} - \nabla \cdot (Up) + \frac{\partial}{\partial t}(\rho K_e) + \nabla \cdot (\rho U K_e)$$
$$= \nabla \cdot (\rho \alpha \nabla h) + \dot{Q}_{rad} \,. \tag{A.8}$$

The last three terms on the left-hand side of the above equation are small for low Mach flows and can be neglected. Following the standard OpenFOAM solvers, only

the term $\nabla \cdot (Up)$ is neglected here. Finally, the energy equation for the gas phase, with unity Lewis number and neglecting the viscosity heat generation, will be in the form of

$$\boxed{\frac{\partial}{\partial t}(\rho h) + \nabla \cdot (\rho U h) - \frac{\partial p}{\partial t} + \frac{\partial}{\partial t}(\rho K_e) + \nabla \cdot (\rho U K_e) = \nabla \cdot (\rho \alpha \nabla h) + \dot{Q}_{rad}}.$$
(A.9)

The above equation is the energy equation that is solved for the gas phase in different solvers used in this study. The form of the energy equation that is considered for the solid particle is quite different. The solid particle is a porous media which contains both solid and gas and thermal equilibrium is assumed to be established between the two phases. Therefore, it is easier to derive the energy equation in terms of the temperature instead of the enthalpy. Unity Lewis number assumption is used and the viscous heat is neglected in this part as well. Furthermore, it is assumed that the terms related to pressure and kinetic energy are negligible inside the particle (low Mach number), and the effect of radiation is included in the conduction term. Therefore, the energy equation for the solid particle can be simplified to

$$\frac{\partial}{\partial t}(\rho h) + \nabla \cdot (\rho U h) = \nabla \cdot (\kappa_{eff} \nabla T) ,$$
(A.10)

where $\kappa_{eff}$ is the effective conductivity which includes radiation effects and is discussed in the thesis in more detail. The solid velocity is equal to zero, so the energy equation can be expressed as

$$\frac{\partial}{\partial t}(\rho_s h_s) + \frac{\partial}{\partial t}(\varepsilon \rho_g h_g) + \nabla \cdot (\varepsilon \rho_g U h_g) = \nabla \cdot (\kappa_{eff} \nabla T) ,$$
(A.11)

where $\varepsilon$ is the porosity and $U$ is the gas velocity vector. Subscripts $s$ and $g$ represent the properties of the solid and gas, respectively. It should be noted that the solid density, $\rho_s$ is the apparent density which includes the porosity. Hence, before shrinkage $\rho_s = (1 - \varepsilon)\rho_{s,true}$, where $\rho_{s,true}$ is the true (intrinsic) density of biomass. We can expand the above equation in the form of

$$\left[ \rho_s \frac{\partial h_s}{\partial t} + h_s \frac{\partial \rho_s}{\partial t} \right] + \left[ \varepsilon \rho_g \frac{\partial h_g}{\partial t} + h_g \frac{\partial \varepsilon \rho_g}{\partial t} \right]$$
$$+ \left[ \varepsilon \rho_g U \nabla h_g + h_g \nabla \cdot (\varepsilon \rho_g U) \right] = \nabla \cdot (\kappa_{eff} \nabla T) .$$
(A.12)

Based on the definition, $h = \sum Y_i h_i$ and the fact that $\partial h_i / \partial t = c_{pi} \partial T / \partial t$ and

$\nabla h_i = c_{pi}\nabla T$, we can rewrite the equation in the following form

$$\left[\rho_s \sum^{N_s} Y_i c_{pi}\frac{\partial T}{\partial t} + \rho_s \sum^{N_s} h_i \frac{\partial Y_i}{\partial t} + h_s \frac{\partial \rho_s}{\partial t}\right]$$

$$+ \left[\varepsilon\rho_g \sum^{N_g} Y_i c_{pi}\frac{\partial T}{\partial t} + \varepsilon\rho_g \sum^{N_g} h_i \frac{\partial Y_i}{\partial t} + h_g \frac{\partial \varepsilon\rho_g}{\partial t}\right]$$

$$+ \left[\varepsilon\rho_g U \sum^{N_g} Y_i c_{pi}\nabla T + \varepsilon\rho_g U \sum^{N_g} h_i \nabla Y_i + h_g \nabla \cdot (\varepsilon\rho_g U)\right] = \nabla \cdot (\kappa_{eff}\nabla T) \,,$$

(A.13)

where $N_s$ and $N_g$ are the number of solid and gas species, respectively. From the continuity equation for the solid species we have

$$\frac{\partial \rho_{s,i}}{\partial t} = \frac{\partial \rho_s Y_i}{\partial t} = \dot{\Re}_{s,i} \,,$$

(A.14)

and by summation we obtain

$$\frac{\partial \rho_s}{\partial t} = \sum^{N_s} \frac{\partial \rho_{s,i}}{\partial t} = \sum^{N_s} \dot{\Re}_{s,i} = \dot{\Re}_s \,.$$

(A.15)

Substituting into the first term in the Eq. A.13 we obtain

$$\left[\rho_s \sum^{N_s} Y_i c_{pi}\frac{\partial T}{\partial t} + \rho_s \sum^{N_s} h_i \frac{\partial Y_i}{\partial t} + h_s \frac{\partial \rho_s}{\partial t}\right]$$

$$= \rho_s c_{ps}\frac{\partial T}{\partial t} + \sum^{N_s} h_i \left(\frac{\partial \rho_s Y_i}{\partial t} - Y_i \frac{\partial \rho_s}{\partial t}\right) + h_s \frac{\partial \rho_s}{\partial t}$$

$$= \rho_s c_{ps}\frac{\partial T}{\partial t} + \sum^{N_s} h_i \left(\dot{\Re}_{s,i} - \cancel{Y_i \dot{\Re}_s}\right) + \cancel{h_s \dot{\Re}_s}$$

(A.16)

$$= \rho_s c_{ps}\frac{\partial T}{\partial t} + \sum^{N_s} h_i \dot{\Re}_{s,i} \,,$$

Similarly, we can use the continuity and species transport equations for the gas species in the form of

$$\frac{\partial}{\partial t}\left(\varepsilon\rho_g\right) + \nabla \cdot (\varepsilon\rho_g U) = \dot{\Re}_g \,,$$

(A.17)

and

$$\frac{\partial}{\partial t}\left(\varepsilon\rho_g Y_i\right) + \nabla\cdot\left(\varepsilon\rho_g U Y_i\right) = \nabla\cdot\left(\rho_g D_{eff,p}\nabla Y_i\right) + \dot{\Re}_{g,i} \tag{A.18}$$

to simplify the second and third terms in Eq. A.13. By substitution into the mentioned terms and neglecting the enthalpy transfer due to diffusion of gas species, we obtain

$$\left[\varepsilon\rho_g\sum^{N_g} Y_i c_{pi}\frac{\partial T}{\partial t} + \varepsilon\rho_g\sum^{N_g} h_i\frac{\partial Y_i}{\partial t} + h_g\frac{\partial\varepsilon\rho_g}{\partial t}\right]$$

$$+ \left[\varepsilon\rho_g U\sum^{N_g} Y_i c_{pi}\nabla T + \varepsilon\rho_g U\sum^{N_g} h_i\nabla Y_i + h_g\nabla\cdot\left(\varepsilon\rho_g U\right)\right] \tag{A.19}$$

$$= \varepsilon\rho_g c_{pg}\frac{\partial T}{\partial t} + \sum^{N_g} h_i\dot{\Re}_{g,i} + \varepsilon\rho_g U c_{pg}\nabla T.$$

Finally, we substitute Eqs. A.16 and A.19 into Eq. A.13 to obtain the energy equation for the solid particle in the form of

$$\left(\rho_s c_{ps} + \varepsilon\rho_g c_{pg}\right)\frac{\partial T}{\partial t} + \varepsilon\rho_g c_{pg}U\nabla T = \nabla\cdot\left(\kappa_{eff}\nabla T\right) - \sum^{N_s} h_i\dot{\Re}_{s,i} - \sum^{N_g} h_i\dot{\Re}_{g,i}. \tag{A.20}$$

We define the total heat capacity as $\left(\rho c_p\right)_{tot} = \varepsilon\rho_g c_{pg} + \rho_s c_{ps}$ and heat of reactions as $\dot{Q}_{reac} = -\sum^{N_s} h_i\dot{\Re}_{s,i} - \sum^{N_g} h_i\dot{\Re}_{g,i}$. Finally, the energy equation for the porous particle can be expressed in the form of

$$\boxed{\left(\rho c_p\right)_{tot}\frac{\partial T}{\partial t} + \varepsilon\rho_g c_{pg}U\nabla T = \nabla\cdot\left(\kappa_{eff}\nabla T\right) + \dot{Q}_{reac}}. \tag{A.21}$$

## A.2   Momentum equation in porous media

The region inside a particle or in a fixed bed is a porous media consisting of both the solid and the gas phases. Depending on the definition of the velocity and the assumptions that have been made (such as constant porosity), the governing equations of the fluid flow in the porous media are reported in different forms [84]. To avoid any confusion, the derivation of the general form of the continuity, momentum, and species transport equations is reported in the following. For any control volume inside the domain with a total volume of $V$, the porosity or void fraction is defined as

$$\varepsilon = V_g/V = 1 - V_s/V, \tag{A.22}$$

where $V_g$ is the volume of the gas and $V_s$ is the volume of the solid. The porosity is used to derive the governing equations for the porous media. Here, we start by deriving the continuity and the momentum equations in a porous media.

We can write the mass conservation equation for a small control volume (CV) with centre coordinates at $(x, y, z)$, with a volume of $V = \Delta x \Delta y \Delta z$ and porosity of $\varepsilon$, such as the one depicted in Figure A.1. Each side of the control volume is partially blocked by the solid material. For instance, the two sides that are normal to the $x$ direction have an area of $A = \Delta y \Delta z = A_g + A_s$, where $A_g$ and $A_s$ are the areas corresponding to the gas and solid on each side. It can be shown that for a homogeneous porous media, the ratio between $A_g$ to $A$ is equal to the porosity [85]

$$A_g/A = 1 - A_s/A = \varepsilon . \tag{A.23}$$
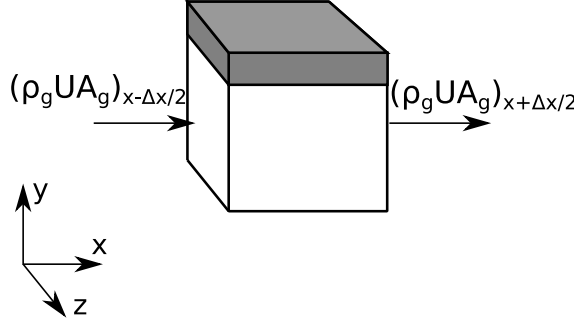


**Figure A.1:** A control volume in the porous media with the inward and outward mass flow rate in the $x$ direction.

Therefore, we can write the mass flux along the $x$ direction as $\dot{m} = \rho_g U_x A_g = \varepsilon \rho_g U_x A$. Based on Figure A.1, for a one-dimensional flow in $x$ direction, the mass conservation equation for gas in a small time-step of $\Delta t$ becomes

$$\frac{\Delta m_g}{\Delta t} = \dot{m}_{in} - \dot{m}_{out} + \dot{\Re}_g V , \tag{A.24}$$

where $m_g = \rho_g V_g$ is the mass of gas in the CV, $\dot{m}_{in}$ and $\dot{m}_{out}$ are the mass flux at the two sides of the CV, and $\dot{\Re}_g$ is the gas formation rate per unit volume due to conversion of solid to gas. Based on the definition of each term, Eq. A.24 becomes

$$\frac{\Delta(\rho_g V_g)}{\Delta t} = (\rho_g U_x A_g)_{x-\Delta x/2} - (\rho_g U_x A_g)_{x+\Delta x/2} + \dot{\Re}_g V , \tag{A.25}$$

which then by using Eq. A.22 and Eq. A.23 becomes

$$\frac{\Delta(\varepsilon \rho_g V)}{\Delta t} = (\varepsilon \rho_g U_x A)_{x-\Delta x/2} - (\varepsilon \rho_g U_x A)_{x+\Delta x/2} + \dot{\Re}_g V . \tag{A.26}$$

Dividing the two sides by the volume, $V$, and moving everything other than the source term to the left-hand side yields

$$\frac{\Delta(\varepsilon\rho_g)}{\Delta t} + \frac{(\varepsilon\rho_g U_x)_{x+\Delta x/2} - (\varepsilon\rho_g U_x)_{x-\Delta x/2}}{\Delta x} = \dot{\Re}_g , \tag{A.27}$$

which by assuming infinitesimally small $\Delta t$ and $\Delta x$, can be converted to a partial differential equation (PDE) in the form of

$$\frac{\partial(\varepsilon\rho_g)}{\partial t} + \frac{\partial(\varepsilon\rho_g U_x)}{\partial x} = \dot{\Re}_g . \tag{A.28}$$

Generalizing the Eq. A.28 to three dimensions leads to

$$\frac{\partial(\varepsilon\rho_g)}{\partial t} + \frac{\partial(\varepsilon\rho_g U_x)}{\partial x} + \frac{\partial(\varepsilon\rho_g U_y)}{\partial y} + \frac{\partial(\varepsilon\rho_g U_z)}{\partial z} = \dot{\Re}_g , \tag{A.29}$$

or identically

$$\boxed{\frac{\partial(\varepsilon\rho_g)}{\partial t} + \nabla \cdot (\varepsilon\rho_g U) = \dot{\Re}_g} . \tag{A.30}$$

The Eq. A.30 is the general form of continuity equation in a porous media with the conversion of solid to gas. The $U$ is the actual velocity vector of the gas phase and should not be confused with the superficial velocity $U_s = \varepsilon U$.

Similarly, we can write the momentum equation for the same control volume as in Figure A.1. The momentum vector of the gas phase is $m_g U$ and based on Newton's second law of motion, the change in the gas phase momentum $\Delta(m_g U)$ over a short period $\Delta t$, is equal to the summation of the momentum of the fluid entering the control volume plus the summation of the forces acting over the mass or the boundaries of the control volume, $\Sigma F$. Therefore, the momentum equation for the CV on the $x$ direction is

$$\frac{\Delta(m_g U_x)}{\Delta t} = (\dot{m}U_x)_{in} - (\dot{m}U_x)_{out} + \Sigma F_x . \tag{A.31}$$

Using the definition of $\varepsilon$ and assuming a one-dimensional flow in the $x$ direction we get

$$\frac{\Delta(\varepsilon\rho_g U_x V)}{\Delta t} = (\varepsilon\rho_g U_x A U_x)_{x-\Delta x/2} - (\varepsilon\rho_g U_x A U_x)_{x+\Delta x/2} + \Sigma F_x , \tag{A.32}$$

and by dividing to V and moving every term except the boundary force to the left-hand side we obtain

$$\frac{\Delta(\varepsilon\rho_g U_x)}{\Delta t} + \frac{(\varepsilon\rho_g U_x U_x)_{x+\Delta x/2} - (\varepsilon\rho_g U_x U_x)_{x-\Delta x/2}}{\Delta x} = \frac{\Sigma F_x}{V} . \tag{A.33}$$

Assuming infinitesimally small volume and time step, we get the PDE form of the momentum equation in the $x$ direction

$$\frac{\partial(\varepsilon \rho_g U_x)}{\partial t} + \frac{\partial(\varepsilon \rho_g U_x U_x)}{\partial x} = \frac{\Sigma F_x}{V} .$$  (A.34)

By repeating the same process for the $y$ and $z$ directions, we can finally get the general momentum equation in vector form. The vector form of the momentum equation that has to be solved in three separate directions is

$$\frac{\partial(\varepsilon \rho_g U)}{\partial t} + \nabla \cdot (\varepsilon \rho_g UU) = \frac{\Sigma F}{V} .$$  (A.35)

The vector $\Sigma F$ in the above equation is the summation of the gravity force acting on the mass of the gas and pressure and viscous forces acting on the boundaries of the control volume. Hence,

$$\Sigma F = F_{gravity} + F_{pressure} + F_{viscous} .$$  (A.36)

The gravity force is equal to $m_g g$, where $g$ is the gravitational acceleration vector. Therefore, the gravity force is equal to

$$F_{gravity} = m_g g = \varepsilon \rho_g V g .$$  (A.37)

The pressure force is acting on the $A_g = \varepsilon A$ on the boundary that is occupied by the gas phase. For instance, the pressure force in the $x$ direction is equal to $F_{pressure,x} = (\varepsilon p A)_{x-\Delta x/2} - (\varepsilon p A)_{x+\Delta x/2}$, where $p$ is the gas phase pressure. Assuming an infinitesimally small volume, and multiplying and dividing the pressure to $V$, we get $F_{pressure,x} = -V\partial(\varepsilon p)/\partial x$. Repeating the same procedure in the three directions gives the vector of pressure force in the form of

$$F_{pressure} = -V\nabla(\varepsilon p) ,$$  (A.38)

where $\nabla$ is the gradient operator.

The final force in the momentum equation of the gas phase is the viscous or the friction force, $F_{viscous}$. In a porous media, the friction force on the boundary is due to both the viscous stress from the neighbour fluid and also the friction from the neighbour solid. The viscous force between the fluids can be calculated similarly to the pressure force, and that is equal to

$$F_{viscous,fluid} = V\nabla \cdot (\varepsilon \tau) ,$$  (A.39)

in which $\tau = \mu_{eff}\big[(\nabla U + \nabla U^T) - 2/3\nabla \cdot UI\big]$ is the viscous stress tensor. The viscous force due to the friction between the fluid and solid is commonly calculated by the Darcy-Forchheimer equation [86]

$$F_{viscous,solid} = -V\left(\frac{\mu\varepsilon}{K}U + \frac{\rho\varepsilon C_F|U|}{\sqrt{K}}U\right) , \qquad (A.40)$$

where $K = (d_p^2\varepsilon^3)/(180(1-\varepsilon)^2)$ is the permeability [87] of the porous media based on pore diameter, $d_p$, and $C_F = 1.75/(150\varepsilon^3)^{1/2}$ is the Forchheimer coefficient [86]. Finally, the total viscous force is equal to the fluid and solid terms, so we have

$$F_{viscous} = F_{viscous,fluid} + F_{viscous,solid} = V\left(\nabla \cdot (\varepsilon\tau) - \frac{\mu\varepsilon}{K}U - \frac{\rho\varepsilon C_F|U|}{\sqrt{K}}U\right) . \quad (A.41)$$

Substituting the Eqs. A.37, A.38 and A.41 into the Eq. A.35 leads to the general momentum equation for the gas phase in the porous media

$$\boxed{\frac{\partial(\varepsilon\rho_g U)}{\partial t} + \nabla \cdot (\varepsilon\rho_g UU) = \varepsilon\rho_g g - \nabla(\varepsilon p) + \nabla \cdot (\varepsilon\tau) - \frac{\mu\varepsilon}{K}U - \frac{\rho\varepsilon C_F|U|}{\sqrt{K}}U.}$$
$$(A.42)$$

The species transport equation can also be derived similarly to the continuity equation, but the effects of species diffusion have to be considered as well. The change of mass of gas species in the control volume can be expressed as

$$\frac{\Delta m_{gi}}{\Delta t} = \dot{m}_{gi,in} - \dot{m}_{gi,out} + \dot{\Re}_{gi}V , \qquad (A.43)$$

where $m_{gi} = m_g Y_{gi}$ is the mass of species $gi$, and $Y_{gi}$ is the mass fraction of that species. The mass flux includes a convective and a diffusive term which is calculated based on Fick's law. For instance, the inward mass flux of species $gi$ in $x$ direction will be

$$\dot{m}_{gi,in} = \left(\varepsilon\rho_g U_x A Y_{gi} - \varepsilon\rho_g A\frac{D_{AB}}{\tau_{tor}}\frac{\partial Y_{gi}}{\partial x}\right)_{x-\Delta x/2} , \qquad (A.44)$$

where $D_{AB}$ is the binary coefficient of the fluid and $\tau_{tor}$ is the tortuosity of the porous media, which is defined as the ratio of the actual path length of flow in the porous media to the straight distance between two points. The tortuosity can be estimated by $\tau_{tor} = 1/\varepsilon$ [56]. The outward mass flux is also described as similar to the inward mass flux in Eq. A.44, and by inserting the terms in Eq. A.43 we obtain

$$\frac{\Delta(\varepsilon\rho_g V Y_{gi})}{\Delta t} = \left(\varepsilon\rho_g U_x A Y_{gi} - \varepsilon\rho_g A\frac{D_{AB}}{\tau_{tor}}\frac{\partial Y_{gi}}{\partial x}\right)_{x-\Delta x/2}$$
$$- \left(\varepsilon\rho_g U_x A Y_{gi} - \varepsilon\rho_g A\frac{D_{AB}}{\tau_{tor}}\frac{\partial Y_{gi}}{\partial x}\right)_{x+\Delta x/2} + \dot{\Re}_{gi}V .$$
$$(A.45)$$

By dividing the above equation to $V$ and assuming small $\Delta t$ and $\Delta x$ and moving the convective terms to the left-hand side we get

$$\frac{\partial(\varepsilon \rho_g Y_{gi})}{\partial t} + \frac{\partial(\varepsilon \rho_g U_x Y_{gi})}{\partial x} = \frac{\partial}{\partial x}\left(\rho_g \frac{\varepsilon D_{AB}}{\tau_{tor}} \frac{\partial Y_{gi}}{\partial x}\right) + \dot{\Re}_{gi} \,. \tag{A.46}$$

Now, we can define an effective diffusivity as $D_{eff} = \varepsilon D_{AB}/\tau_{tor} = \varepsilon^2 D_{AB}$ and rewrite the equations in three directions in the vector form. Finally, the species transport equation in the porous media can be expressed in the form of

$$\boxed{\frac{\partial(\varepsilon \rho_g Y_{gi})}{\partial t} + \nabla \cdot (\varepsilon \rho_g U Y_{gi}) = \nabla \rho_g D_{eff} \nabla Y_{gi} + \dot{\Re}_{gi}} \,. \tag{A.47}$$

## A.3  Mass transfer limited char conversion

The char combustion and gasification reactions can be controlled by either the chemical kinetics or the mass transfer of the gasifying agent ($O_2$, $H_2O$, or $CO_2$). The derivation of the mass transfer limited rate equations for a spherical particle with a diameter of $d_p$ is presented in this section. For non-spherical particles, the $d_p$ is replaced with the equivalent diameter, $d_{eq}$, which is the diameter of a sphere with the same volume as the non-spherical particle.
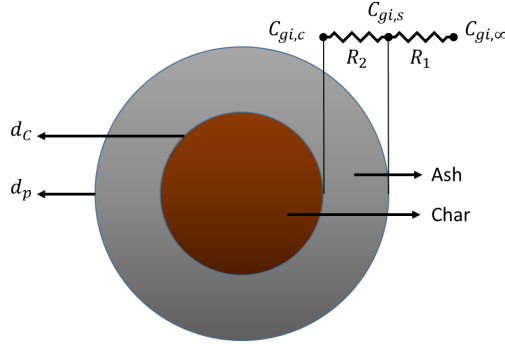


**Figure A.2:** Schematic of the electric current analogy for convection and diffusion of the gasifying agent from the surrounding gas to the char surface.

In general, the gasifying agent is transferred from the surrounding atmosphere to the surface of the particle through mass convection and then diffuses through the ash layer to reach the char surface. The mass transfer rate of the gasifying agent can be calculated based on the electric current analogy as presented in Fig. A.2. In this case, two variables, $R_1$ and $R_2$ [m3/s], can be defined as the resistance to convection and

diffusion of the gasifying agent, respectively. For a spherical particle with diameter $d_p$, the convective mass flow rate $\dot{m}_{gi,conv}$ [kg/s] of gas species $gi$ to the surface of the particle can be expressed as

$$\dot{m}_{gi} = \frac{\left(C_{gi,\infty} - C_{gi,c}\right) M_{gi}}{R_1 + R_2} \, , \tag{A.48}$$

where $C_{gi,\infty}$ and $C_{gi,c}$ are the concentration of species [kmol/m$^3$] in the surrounding gas and at the char surface, respectively. $M_{gi}$ [kg/kmol] is the molecular weight of the gasifying agent. The resistance to convection, $R_1$, can be calculated using the definition of mass convection coefficient $\dot{m}_{gi,conv} = h_m A_p \left(C_{gi,\infty} - C_{gi,s}\right)$, where $C_{gi,s}$ is the gas concentration at the particle surface. This gives

$$R_1 = \frac{1}{A_p h_m} \, , \tag{A.49}$$

where $A_p = \pi d_p^2$ [m$^2$] is the particle surface area, and $h_m$ [m/s] is the mass convection coefficient. $h_m$ can be calculated based on the Sherwood number (Sh) definition

$$h_m = \frac{\text{Sh} D_{AB}}{d_p} \, , \tag{A.50}$$

in which $D_{AB}$ [m$^2$/s]is the binary diffusion coefficient. Based on Fick's law of diffusion, the resistance to diffusion in the porous ash layer in a spherical particle can be expressed as

$$R_2 = \frac{d_p - d_C}{2\pi d_p d_C D_{eff}} \, , \tag{A.51}$$

where $d_C$ is the char diameter and $D_{eff} = \varepsilon_A^2 D_{AB}$ is the effective diffusion coefficient, as explained in Section A.2, and $\varepsilon_A$ is the ash porosity. In mass transfer limited conditions, all of the gasifying agents will be consumed at the char surface, which gives $C_{gi,c} = 0$. Hence, we can finally rewrite Eq. A.48 to calculate the mass transfer rate of the gasifying agent to the char surface in a spherical particle as

$$\dot{m}_{gi} = C_{gi,\infty} M_{gi} \left[ \frac{1}{\pi d_p \text{Sh} D_{AB}} + \frac{d_p - d_C}{2\pi d_p d_C \varepsilon_A^2 D_{AB}} \right]^{-1} . \tag{A.52}$$

In the case of small fuel particles which are moving with the fluid, such as in the fluidized or entrained flow reactors, the mass transfer rate equation can be more simplified. First, it is assumed that the ash is quickly removed from the surface of the particle by the airflow, so $R_2$ becomes zero. Second, it can be assumed that the relative velocity between the particle and surrounding fluid is zero, which leads to Sh = 2.

On the other hand, the binary diffusion coefficient at the particle surface temperature can be estimated from the following correlation [88, 45]

$$D_{AB} = D_{AB,ref}\left(\frac{T_s}{T_{ref}}\right)^{1.75}, \tag{A.53}$$

where $D_{AB,ref}$ is the diffusion coefficient at a reference temperature, $T_{eff}$, and $T_s$ is the gas temperature at the particle surface. Furthermore, from the ideal gas law we can write

$$C_{gi,\infty} = \frac{p_{gi}}{R_u T_g}, \tag{A.54}$$

in which $p_{gi}$ and $T_g$ are the partial pressure of the gasifying agent and gas temperature near the particle surface, respectively, and $R_u$ is the universal gas constant. Based on the above assumptions and Eqs. A.53 and A.54, the mass transfer rate of the gasifying agent will be simplified as

$$\dot{m}_{gi} = \frac{p_{gi}M_{gi}}{R_u T_g}\left[2\frac{A_p}{d_p}D_{AB,ref}\left(\frac{T_s}{T_{ref}}\right)^{1.75}\right]. \tag{A.55}$$

Based on the above equation, and assuming $T_g$ is close to $T_s$, the char conversion rate can be expressed in the form of

$$\dot{m}_C = \dot{m}_{gi}\frac{M_C \nu_{C,gi}}{M_{gi}} = \left(\frac{2M_C D_{AB,ref}\nu_{C,gi}}{R_u T_{ref}^{1.75}}\right) A_p p_{gi}\frac{T_s^{0.75}}{d_p}. \tag{A.56}$$

where $M_C$ is the molecular weight of char and $\nu_{C,gi}$ is the stoichiometric ratio of the char to the gasifying agent. The value in the parenthesis is a constant for each gasifying agent, so we can define a constant $C_{diff,i}$ such that

$$C_{diff,i} = \frac{2M_C D_{AB,ref}\nu_{C,gi}}{R_u T_{ref}^{1.75}}. \tag{A.57}$$

This simplifies the char conversion rate for fluidized particles to

$$\dot{m}_C = C_{diff,i}A_p p_{gi}\frac{T_s^{0.75}}{d_p}, \tag{A.58}$$

where in some studies, $T_s$ is estimated by the average temperature of the particle and surrounding gas, $0.5(T_p + T_g)$ [40]. Furthermore, the value of $C_{diff,i}$ can be estimated by assuming $D_{AB,ref} = 3 \times 10^{-5}$ at $T_{ref} = 300$ K. This leads to $C_{diff,i} = 4 \times 10^{-12}\nu_{C,gi}$ which is comparable to the values reported in the literature [40, 89].

# References

[1] W. B. Association, Global bioenergy statistics (2021).

[2] E. Commission, Consolidated text: Directive (EU) 2018/2001 of the European Parliament and of the Council of 11 December 2018 on the promotion of the use of energy from renewable sources (recast) (2021).

[3] E. Commission, Simplified energy balances, data received from the website of eurostat (European commission), `https://ec.europa.eu/eurostat/databrowser/view/NRG_BAL_S__custom_3203970/default/table?lang=en` (2022).

[4] T. I. E. A. (IEA), Energy supply in sweden, data received from the website of IEA, `https://www.iea.org/countries/sweden` (2022).

[5] C. Di Blasi, Combustion and gasification rates of lignocellulosic chars, Progress in energy and combustion science 35 (2) (2009) 121–140.

[6] H. Fatehi, Numerical Simulation of Combustion and Gasification of Biomass Particles, Division of Fluid Mechanics, Department of Enegy Sciences, Lund University …, 2014.

[7] H. Fatehi, W. Weng, Z. Li, X.-S. Bai, M. Alden, Recent development in numerical simulations and experimental studies of biomass thermochemical conversion, Energy & Fuels 35 (9) (2021) 6940–6963.

[8] D. Neves, H. Thunman, A. Matos, L. Tarelho, A. Gómez-Barea, Characterization and prediction of biomass pyrolysis products, Progress in energy and combustion Science 37 (5) (2011) 611–630.

[9] A. Gómez-Barea, B. Leckner, Modeling of biomass gasification in fluidized bed, Progress in Energy and Combustion Science 36 (4) (2010) 444–509.

[10] J. Zhou, Q. Chen, H. Zhao, X. Cao, Q. Mei, Z. Luo, K. Cen, Biomass-oxygen gasification in a high-temperature entrained-flow gasifier., Biotechnology advances 27 (5) (2009) 606–611.

[11] Y. Ögren, M. Gullberg, J. Wennebro, A. Sepman, P. Tóth, H. Wiinikka, Influence of oxidizer injection angle on the entrained flow gasification of torrefied wood powder, Fuel processing technology 181 (2018) 8–17.

[12] X. Gao, Y. Zhang, B. Li, X. Yu, Model development for biomass gasification in an entrained flow gasifier using intrinsic reaction rate submodel, Energy Conversion and Management 108 (2016) 120–131.

[13] A. Williams, J. Jones, L. Ma, M. Pourkashanian, Pollutants from the combustion of solid biomass fuels, Progress in Energy and Combustion Science 38 (2) (2012) 113–137.

[14] P. Glarborg, A. Jensen, J. E. Johnsson, Fuel nitrogen conversion in solid fuel fired systems, Progress in energy and combustion science 29 (2) (2003) 89–113.

[15] P. Glarborg, J. A. Miller, B. Ruscic, S. J. Klippenstein, Modeling nitrogen chemistry in combustion, Progress in Energy and Combustion Science 67 (2018) 31 − 68. doi:https://doi.org/10.1016/j.pecs.2018.01.002.

[16] T. Løvås, E. Houshfar, M. Bugge, Ø. Skreiberg, Automatic generation of kinetic skeletal mechanisms for biomass combustion, Energy & Fuels 27 (11) (2013) 6979–6991. doi:10.1021/ef400949h.

[17] T. Li, Ø. Skreiberg, T. Løvås, P. Glarborg, Skeletal mechanisms for prediction of NOx emission in solid fuel combustion, Fuel 254 (2019) 115569.

[18] S. Daood, M. Javed, B. Gibbs, W. Nimmo, NOx control in coal combustion by combining biomass co-firing, oxygen enrichment and SNCR, Fuel 105 (2013) 283 − 292. doi:https://doi.org/10.1016/j.fuel.2012.06.087.

[19] D. Dayton, B. Jenkins, S. Turn, R. Bakker, R. Williams, D. Belle-Oudry, L. Hill, Release of inorganic constituents from leached biomass during thermal conversion, Energy & Fuels 13 (4) (1999) 860–870.

[20] T. de Riese, D. Eckert, L. Hakim, S. Fendt, H. Spliethoff, Modelling the capture of potassium by solid Al-Si particles at pulverised fuel conditions, Fuel 328 (2022) 125321.

[21] J. N. Knudsen, P. A. Jensen, K. Dam-Johansen, Transformation and release to the gas phase of Cl, K, and S during combustion of annual biomass, Energy & Fuels 18 (5) (2004) 1385–1399.

[22] Y. Huang, H. Liu, H. Yuan, X. Zhuang, S. Yuan, X. Yin, C. Wu, Release and transformation pathways of various K species during thermal conversion of agricultural straw. Part 1: devolatilization stage, Energy & Fuels 32 (9) (2018) 9605–9613.

[23] P. Debiagi, G. Gentile, A. Cuoci, A. Frassoldati, E. Ranzi, T. Faravelli, A predictive model of biochar formation and characterization, Journal of Analytical and Applied Pyrolysis 134 (2018) 326–335.

[24] I. Haberle, Ø. Skreiberg, J. Łazar, N. E. L. Haugen, Numerical models for thermochemical degradation of thermally thick woody biomass, and their application in domestic wood heating appliances and grate furnaces, Progress in Energy and Combustion Science 63 (2017) 204–252.

[25] H. Thunman, B. Leckner, F. Niklasson, F. Johnsson, Combustion of wood particles—a particle model for Eulerian calculations, Combustion and Flame 129 (1-2) (2002) 30–46.

[26] H. Lu, W. Robert, G. Peirce, B. Ripa, L. L. Baxter, Comprehensive study of biomass particle combustion, Energy & Fuels 22 (4) (2008) 2826–2839.

[27] H. Fatehi, X.-S. Bai, A comprehensive mathematical model for biomass combustion, Combustion Science and Technology 186 (4-5) (2014) 574–593.

[28] W. C. Park, A. Atreya, H. R. Baum, Experimental and theoretical investigation of heat and mass transfer processes during wood pyrolysis, Combustion and Flame 157 (3) (2010) 481–494.

[29] C. Di Blasi, Physico-chemical processes occurring inside a degrading two-dimensional anisotropic porous medium, International journal of heat and mass transfer 41 (24) (1998) 4139–4150.

[30] M. Gómez, J. Porteiro, S. Chapela, J. Míguez, An Eulerian model for the simulation of the thermal conversion of a single large biomass particle, Fuel 220 (2018) 671–681.

[31] D. Shin, S. Choi, The combustion of simulated waste particles in a fixed bed, Combustion and flame 121 (1-2) (2000) 167–180.

[32] C. Di Blasi, Dynamic behaviour of stratified downdraft gasifiers, Chemical engineering science 55 (15) (2000) 2931–2944.

[33] M. R. Karim, J. Naser, Numerical study of the ignition front propagation of different pelletised biomass in a packed bed furnace, Applied Thermal Engineering 128 (2018) 772–784.

[34] R. Johansson, H. Thunman, B. Leckner, Influence of intraparticle gradients in modeling of fixed bed combustion, Combustion and Flame 149 (1-2) (2007) 49–62.

[35] H. Ström, H. Thunman, A computationally efficient particle submodel for CFD-simulations of fixed-bed conversion, Applied energy 112 (2013) 808–817.

[36] M. Gómez, J. Porteiro, D. Patiño, J. Míguez, Fast-solving thermally thick model of biomass particles embedded in a CFD code for the simulation of fixed-bed burners, Energy Conversion and Management 105 (2015) 30–44.

[37] T. Li, H. Thunman, H. Ström, A fast-solving particle model for thermochemical conversion of biomass, Combustion and Flame 213 (2020) 117–131.

[38] E. Ranzi, S. Pierucci, P. C. Aliprandi, S. Stringa, Comprehensive and detailed kinetic model of a traveling grate combustor of biomass, Energy & Fuels 25 (9) (2011) 4195–4205.

[39] S. Hermansson, H. Thunman, CFD modelling of bed shrinkage and channelling in fixed-bed combustion, Combustion and Flame 158 (5) (2011) 988–999.

[40] X. Ku, T. Li, T. Løvås, Eulerian–Lagrangian simulation of biomass gasification behavior in a high-temperature entrained-flow reactor, Energy & fuels 28 (8) (2014) 5184–5196.

[41] M. Yang, J. Zhang, S. Zhong, T. Li, T. Løvås, H. Fatehi, X.-S. Bai, CFD modeling of biomass combustion and gasification in fluidized bed reactors using a distribution kernel method, Combustion and Flame 236 (2022) 111744.

[42] M. Yang, S. M. Mousavi, X.-S. Bai, H. Fatehi, Numerical simulation of biomass gasification in fluidized bed gasifiers, Fuel.

[43] T. Klason, X. Bai, Computational study of the combustion process and NO formation in a small-scale wood pellet furnace, Fuel 86 (10) (2007) 1465 – 1474. doi:https://doi.org/10.1016/j.fuel.2006.11.022.

[44] M. Farokhi, M. Birouk, Modeling of the gas-phase combustion of a grate-firing biomass furnace using an extended approach of eddy dissipation concept, Fuel 227 (2018) 412 – 423. doi:https://doi.org/10.1016/j.fuel.2018.04.102.

[45] M. Hosseini Rahdar, F. Nasiri, B. Lee, A review of numerical modeling and experimental analysis of combustion in moving grate biomass combustors, Energy & Fuels 33 (10) (2019) 9367–9402.

[46]  J. Zhang, T. Li, H. Ström, T. Løvås, Computationally efficient coarse-graining XDEM/CFD modeling of fixed-bed combustion of biomass, Combustion and Flame 238 (2022) 111876.

[47]  C. Di Blasi, C. Branca, Kinetics of primary product formation from wood pyrolysis, Industrial & engineering chemistry research 40 (23) (2001) 5547–5556.

[48]  H. Fatehi, Y. He, Z. Wang, Z. Li, X.-S. Bai, M. Aldén, K. Cen, LIBS measurements and numerical studies of potassium release during biomass gasification, Proceedings of the Combustion Institute 35 (2) (2015) 2389–2396.

[49]  H. Fatehi, Z. Li, X. Bai, M. Aldén, Modeling of alkali metal release during biomass pyrolysis, Proceedings of the Combustion Institute 36 (2) (2017) 2243–2251.

[50]  H. Fatehi, M. Costa, X.-S. Bai, Numerical study on K/S/Cl release during devolatilization of pulverized biomass at high temperature, Proceedings of the Combustion Institute 38 (3) (2021) 3909–3917.

[51]  M. Pelucchi, C. Cavallotti, A. Cuoci, T. Faravelli, A. Frassoldati, E. Ranzi, Detailed kinetics of substituted phenolic species in pyrolysis bio-oils, Reaction Chemistry & Engineering 4 (3) (2019) 490–506.

[52]  H. Goyal, P. Pepiot, A compact kinetic model for biomass pyrolysis at gasification conditions, Energy & Fuels 31 (11) (2017) 12120–12132. doi:10.1021/acs.energyfuels.7b01634.

[53]  W. Weng, S. Chen, H. Wu, P. Glarborg, Z. Li, Optical investigation of gas-phase KCl/KOH sulfation in post flame conditions, Fuel 224 (2018) 461–468.

[54]  M. R. Mortensen, H. Hashemi, H. Wu, P. Glarborg, Modeling post-flame sulfation of KCl and KOH in bio-dust combustion with full and simplified mechanisms, Fuel 258 (2019) 116147.

[55]  R. Mehrabian, R. Scharler, I. Obernberger, Effects of pyrolysis conditions on the heating rate in biomass particles and applicability of TGA kinetic parameters in particle thermal conversion modelling, Fuel 93 (2012) 567–575.

[56]  H. Fatehi, F. M. Schmidt, X.-S. Bai, Gas phase combustion in the vicinity of a biomass particle during devolatilization–model development and experimental verification, Combustion and Flame 196 (2018) 351–363.

[57]  K. M. Bryden, M. J. Hagge, Modeling the combined impact of moisture and char shrinkage on the pyrolysis of a biomass particle, Fuel 82 (13) (2003) 1633–1644.

[58] F. Thurner, U. Mann, Kinetic investigation of wood pyrolysis, Industrial & Engineering Chemistry Process Design and Development 20 (3) (1981) 482–488.

[59] E. Ranzi, M. Corbetta, F. Manenti, S. Pierucci, Kinetic modeling of the thermal degradation and combustion of biomass, Chemical Engineering Science 110 (2014) 2–12.

[60] E. Ranzi, P. E. A. Debiagi, A. Frassoldati, Mathematical modeling of fast biomass pyrolysis and bio-oil formation. note i: Kinetic mechanism of biomass pyrolysis, ACS Sustainable Chemistry & Engineering 5 (4) (2017) 2867–2881.

[61] D. D. Evans, H. W. Emmons, Combustion of wood charcoal, Fire Safety Journal 1 (1) (1977) 57–66.

[62] N. M. Laurendeau, Heterogeneous kinetics of coal char gasification and combustion, Progress in energy and combustion science 4 (4) (1978) 221–270.

[63] R. B. Bird, W. E. Stewart, E. N. Lightfoot, Transport phenomena, John Wiley & Sons, New York, 1961.

[64] T. Chen, T. Li, J. Sjöblom, H. Ström, A reactor-scale CFD model of soot formation during high-temperature pyrolysis and gasification of biomass, Fuel 303 (2021) 121240.

[65] T. Kashiwagi, H. Nambu, Global kinetic constants for thermal oxidative degradation of a cellulosic paper, Combustion and Flame 88 (3-4) (1992) 345–368.

[66] F. Van den Aarsen, A. Beenackers, W. Swaaij, Wood pyrolysis and carbon dioxide char gasification kinetics in a fluidized bed. fundamentals of biomass thermochemical conversion (1985).

[67] T. Kojima, P. Assavadakorn, T. Furusawa, Measurement and evaluation of gasification kinetics of sawdust char with steam in an experimental fluidized bed, Fuel processing technology 36 (1-3) (1993) 201–207.

[68] M. L. Hobbs, P. T. Radulovic, L. D. Smoot, Modeling fixed-bed coal gasifiers, AIChE Journal 38 (5) (1992) 681–702.

[69] F. Ossler, L. J. Santodonato, J. M. Warren, C. E. A. Finney, J.-C. Bilheux, R. A. Mills, H. D. Skorpenske, H. Z. Bilheux, In situ monitoring of hydrogen loss during pyrolysis of wood by neutron imaging, Proceedings of the Combustion Institute 37 (2) (2019) 1273–1280.

[70] F. Ossler, C. E. A. Finney, J. M. Warren, J.-C. Bilheux, Y. Zhang, R. A. Mills, L. J. Santodonato, H. Z. Bilheux, Dynamics of hydrogen loss and structural

changes in pyrolyzing biomass utilizing neutron imaging, Carbon 176 (2021) 511–529.

[71] E. Thorin, A. Sepman, Y. Ögren, C. Ma, M. Carlborg, J. Wennebro, M. Broström, H. Wiinikka, F. M. Schmidt, Quantitative real-time in situ measurement of gaseous K, KOH and KCl in a 140 kW entrained-flow biomass gasifier, Proceedings of the Combustion Institute.

[72] M. F. Modest, S. Mazumder, Radiative heat transfer, Academic press, 2021.

[73] Y. Mahmoudi, Effect of thermal radiation on temperature differential in a porous medium under local thermal non-equilibrium condition, International Journal of Heat and Mass Transfer 76 (2014) 105–121.

[74] Q. Brewster, Volume scattering of radiation in packed beds of large, opaque spheres, J. Heat Transfer 126 (6) (2004) 1048–1050.

[75] Gregory P. Smith and David M. Golden and Michael Frenklach and Nigel W. Moriarty and Boris Eiteneer and Mikhail Goldenberg et al., GRI-Mech 3.0, [Online; accessed 23-October-2020] (unknown date).
URL http://combustion.berkeley.edu/gri-mech/version30/text30.html

[76] L. Yan, C. J. Lim, G. Yue, B. He, J. R. Grace, Simulation of biomass-steam gasification in fluidized bed reactors: model setup, comparisons and preliminary predictions, Bioresource technology 221 (2016) 625–635.

[77] I. Haberle, N. E. L. Haugen, Ø. Skreiberg, Combustion of thermally thick wood particles: a study on the influence of wood particle size on the combustion behavior, Energy & Fuels 32 (6) (2018) 6847–6862.

[78] T. Chen, X. Ku, J. Lin, H. Jin, Modelling the combustion of thermally thick biomass particles, Powder Technology 353 (2019) 110–124.

[79] T. Sorvajärvi, N. DeMartini, J. Rossi, J. Toivonen, In situ measurement technique for simultaneous detection of K, KCl, and KOH vapors released during combustion of solid biomass fuel in a single particle reactor, Applied spectroscopy 68 (2) (2014) 179–184.

[80] A. Sepman, E. Thorin, Y. Ögren, C. Ma, M. Carlborg, J. Wennebro, M. Broström, H. Wiinikka, F. M. Schmidt, Laser-based detection of methane and soot during entrained-flow biomass gasification, Combustion and Flame 237 (2022) 111886.

[81] H. Wiinikka, High temperature aerosol formation and emission minimisation during combustion of wood pellets, Ph.D. thesis, Luleå tekniska universitet (2005).

[82] H. Wiinikka, R. Gebart, C. Boman, D. Boström, A. Nordin, M. Öhman, High-temperature aerosol formation in wood pellets flames: Spatially resolved measurements, Combustion and Flame 147 (4) (2006) 278–293.

[83] X.-S. Bai, Turbulent combustion, Lecture notes, Lund University, 2008.

[84] Z. Zhou, S. Kuang, K. Chu, A. Yu, Discrete particle simulation of particle–fluid flow: model formulations and their applicability, Journal of Fluid Mechanics 661 (2010) 482–510.

[85] C. Crowe, M. Sommerfeld, Y. Tsuji, et al., Multiphase flows with droplets and particles, Ž, 1998.

[86] P. Yu, Y. Zeng, T. S. Lee, X. B. Chen, H. T. Low, Steady flow around and through a permeable circular cylinder, Computers & Fluids 42 (1) (2011) 1–12.

[87] F. A. Dullien, Porous media: fluid transport and pore structure, Academic press, 2012.

[88] J. R. Van Ommen, W. de Jong, Biomass as a sustainable energy source for the future: fundamentals of conversion processes, John Wiley & Sons, 2014.

[89] N. Abani, A. F. Ghoniem, Large eddy simulations of coal gasification in an entrained flow gasifier, Fuel 104 (2013) 664–680.

# Scientific publications

## Author contributions

Co-authors are abbreviated as follows:
Seyed Morteza Mousavi (MM), Hesameddin Fatehi (HF), Xue-Song Bai (XB), Charles Finney (CF), Frederik Ossler (FO), Florian Schmidt (FS), Emil Thorin (ET), Alexey Sepman (AS).

**Paper I: Multi-region modeling of conversion of a thick biomass particle and the surrounding gas phase reactions**
**Seyed Morteza Mousavi**, Hesameddin Fatehi, Xue-Song Bai
*Combustion and Flame* 237 (2022): 111725,
    https://doi.org/10.1016/j.combustflame.2021.111725
The candidate (MM) developed the particle model and did the programming, performed numerical simulations, post-processed and analysed the results and wrote the first draft of the manuscript. All simulations, analysis, and writing were done under supervision of supervisors (HF and XB). The manuscript was revised by HF and XB.

**Paper II: Detailed modeling of hydrogen release and particle shrinkage during pyrolysis of inhomogeneous wood**
**Seyed Morteza Mousavi**, Frederik Ossler, Charles E.A. Finney, Xue-Song Bai, Hesameddin Fatehi
*Proceedings of the Combustion Institute* 39 (2022): , 1540-7489,
    https://doi.org/10.1016/j.proci.2022.07.108
The candidate (MM) developed the anisotropic shrinkage model, performed numerical simulations, post-processed and analysed the results and wrote the first draft of the manuscript. All simulations, analysis, and writing were done under supervision of supervisors (HF and XB). The experimental measurements and some analysis of the results were performed by FO and CF. The manuscript was revised by HF, XB, FO, and CF.

**Paper III: A multi-step predictive model for the release and transformation of K-Cl-S-containing species from biomass**

**Seyed Morteza Mousavi**, Xue-Song Bai, Hesameddin Fatehi

*Accepted for publication in Combustion and Flame* (2022)

The candidate (MM) developed the multi-step potassium release model, performed numerical simulations, post-processed and analysed the results and wrote the first draft of the manuscript. All simulations, analysis, and writing were done under supervision of supervisors (HF and XB). The manuscript was revised by HF and XB.

**Paper IV: Numerical study and experimental verification of biomass gasification and potassium release in a 140 kW entrained-flow gasifier**

**Seyed Morteza Mousavi**, Emil Thorin, Florian M. Schmidt, Alexey Sepman, Xue-Song Bai, Hesameddin Fatehi

*Energy and Fuels* (2022): Under revision.

The candidate (MM) applied the potassium release model to the reactor scale simulations, performed numerical simulations, post-processed and analysed the results and wrote the first draft of the manuscript. All simulations, analysis, and writing were done under supervision of supervisors (HF and XB). The experimental measurements and some analysis of the results were performed by FS, ET, and AS. The manuscript was revised by HF, XB, FS, ET and AS.

**Paper V: Numerical study of the combustion and application of SNCR for NOx reduction in a lab-scale biomass boiler**

**Seyed Morteza Mousavi**, Hesameddin Fatehi, Xue-Song Bai

*Fuel* 293 (2020): 120154,                 https://doi.org/10.1016/j.fuel.2021.120154

The candidate (MM) performed numerical simulations, post-processed and analysed the results and wrote the first draft of the manuscript. All simulations, analysis, and writing were done under supervision of supervisors (HF and XB). The manuscript was revised by HF and XB.

**Paper VI: A tabulation-based numerical model for the combustion of thick particles in fixed-bed reactors**
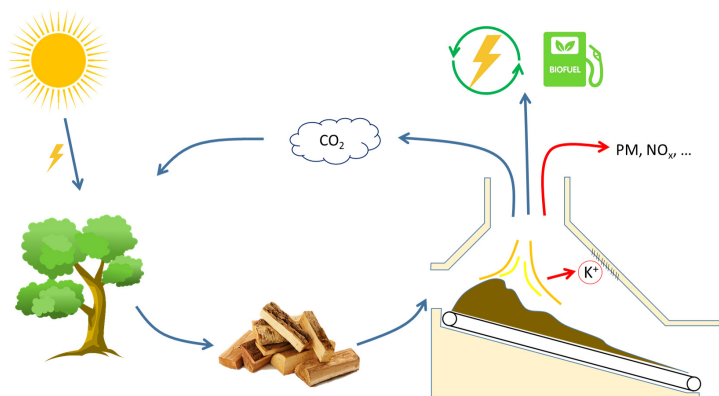
**Seyed Morteza Mousavi**, Hesameddin Fatehi, Xue-Song Bai

*Manuscript to be submitted*

The candidate (MM) developed the bed model and did the programming, performed numerical simulations, post-processed and analysed the results and wrote the first draft of the manuscript. All simulations and analysis were done under supervision of supervisors (HF and XB).

This graphical abstract shows the key elements and also some challenges of sustainable energy production through biomass thermochemical conversion. The main source of the energy is the sun and the whole process is $CO_2$-neutral because the same amount of $CO_2$ that was absorbed by biomass (the plant) will be released into the atmosphere again. Solid biomass can be oxidized to directly produce energy, or it can be converted to other types of liquid or gaseous biofuels. Two of the main challenges for biomass utilization are the $NO_x$ emissions and potassium (K) release from the solid fuel. $NO_x$ is harmful to the environment and potassium can damage the conversion device or lead to particulate matter (PM) emissions. In this thesis, numerical models are developed to study biomass conversion at the particle, fuel bed, and reactor scales. The release of potassium from the solid fuel and also the $NO_x$ emissions from the reactor are investigated using the models. The simulation results help to better understand the process of biomass conversion, and also to find solutions for the mentioned problems associated with potassium and $NO_x$ emissions.